

**STRUCTURAL AND FUNCTIONAL CHARACTERIZATION OF  
THE PROLINE-RICH REGION WITHIN THE  $\alpha$ 4- $\alpha$ 5 LOOP OF  
THE *Bacillus thuringiensis* Cry4Aa TOXIN**

**CHOMPOUNOOT IMTONG**

**A THESIS SUBMITTED IN PARTIAL FULFILLMENT  
OF THE REQUIREMENTS FOR  
THE DEGREE OF DOCTOR OF PHILOSOPHY  
(MOLECULAR GENETICS AND GENETIC ENGINEERING)  
FACULTY OF GRADUATE STUDIES  
MAHIDOL UNIVERSITY  
2014**

**COPYRIGHT OF MAHIDOL UNIVERSITY**

Thesis  
entitled  
**STRUCTURAL AND FUNCTIONAL CHARACTERIZATION OF  
THE PROLINE-RICH REGION WITHIN THE  $\alpha$ 4- $\alpha$ 5 LOOP OF  
THE *Bacillus thuringiensis* Cry4Aa TOXIN**

.....  
Miss Chompounoot Imtong  
Candidate

.....  
Assoc. Prof. Chanan Angsuthanasombat, Ph.D.  
Major advisor

.....  
Asst. Prof. Gerd Katzenmeier, Ph.D.  
Co-advisor

.....  
Mr. Somphob Leetachewa, Ph.D.  
Co-advisor

.....  
Lect. Chalernpol Kanchanawarin, Ph.D.  
Co-advisor

.....  
Prof. Banchong Mahaisavariya,  
M.D., Dip Thai Board of Orthopedics  
Dean  
Faculty of Graduate Studies  
Mahidol University

.....  
Assoc. Prof. Apinunt Udomkit, Ph.D.  
Program Director  
Doctor of Philosophy Program in  
Molecular Genetics and Genetic Engineering  
Institute of Molecular Biosciences  
Mahidol University

Thesis  
entitled  
**STRUCTURAL AND FUNCTIONAL CHARACTERIZATION OF  
THE PROLINE-RICH REGION WITHIN THE  $\alpha$ 4- $\alpha$ 5 LOOP OF  
THE *Bacillus thuringiensis* Cry4Aa TOXIN**

was submitted to the Faculty of Graduate Studies, Mahidol University  
for the degree of Doctor of Philosophy  
(Molecular Genetics and Genetic Engineering)

on  
March 21, 2014

.....  
Miss Chompounoot Imtong  
Candidate

.....  
Assoc. Prof. Apinunt Udomkit, Ph.D.  
Chair

.....  
Assoc. Prof. Chanan Angsuthanasombat, Ph.D.  
Member

.....  
Asst. Prof. Gerd Katzenmeier, Ph.D.  
Member

.....  
Lect. Chalernpol Kanchanawarin, Ph.D.  
Member

.....  
Lect. Lerson Tanasugarn, Ph.D.  
Member

.....  
Prof. Banchong Mahaisavariya,  
M.D., Dip Thai Board of Orthopedics  
Dean  
Faculty of Graduate Studies  
Mahidol University

.....  
Prof. Prasert Auewarakul,  
M.D., Dr. med.  
Director  
Institute of Molecular Biosciences  
Mahidol University

## ACKNOWLEDGEMENTS

The success of this thesis can be attributed to the attentive support from my major advisor, Assoc. Prof. Chanan Angsuthanasombat, and my co-advisors, Asst. Prof. Gerd Katzenmeier, Dr. Somphob Leetachewa and Dr. Chalernpol Kanchanawarin. I deeply thank them for their valuable advice and grateful discussion during this research.

I would like to thank all previous/present lab members, especially Mrs. Somsri Sakdee, for their help in performing some experiments. I wish to thank all staffs of the Institute of Molecular Biosciences for their technical supports.

I am grateful to the Development and Promotion of Science and Technology Talents Project (DPST) that provides me the opportunity to do this research.

Finally, I would like to express my appreciation to my parents for their care and encouragement.

Chompounoot Imtong

STRUCTURAL AND FUNCTIONAL CHARACTERIZATION OF THE PROLINE-RICH REGION WITHIN THE  $\alpha$ 4- $\alpha$ 5 LOOP OF THE *Bacillus thuringiensis* Cry4Aa TOXIN

CHOMPOUNOOT IMTONG 4937168 MBMG/D

Ph.D. (MOLECULAR GENETICS AND GENETIC ENGINEERING)

THESIS ADVISORY COMMITTEE: CHANAN ANGSUTHANASOMBAT, Ph.D.,  
GERD KATZENMEIER, Ph.D., SOMPHOB LEETACHEWA, Ph.D.,  
CHALERMPOL KANCHANAWARIN, Ph.D.

ABSTRACT

The long loop connecting transmembrane helices 4 and 5 of the *Bacillus thuringiensis* Cry4Aa toxin possesses unique structural features including a proline-rich sequence (Pro<sup>193</sup>Pro<sup>194</sup>Pro<sup>196</sup>) which was previously shown to be crucial for mosquito-larvicidal activity. In this study, the structural importance of the proline-rich region was further clarified. Initially, the three proline residues (Pro<sup>193</sup>, Pro<sup>194</sup> and Pro<sup>196</sup>) were substituted individually with valine, a hydrophobic residue with size similar to proline, and the resulting mutants were expressed in *Escherichia coli* cells at levels similar to that of the wild-type toxin. Bioassays demonstrated that *E. coli* cells expressing each mutant toxin exhibited a reduction in toxicity against *Aedes aegypti* mosquito larvae, suggesting an important role in toxin function of unique cyclic structure, not hydrophobic feature, of the loop proline residues. Molecular dynamics (MD) simulations of the 65-kDa Cry4Aa structure in 150 mM KCl solution revealed that the  $\alpha$ 4- $\alpha$ 5 loop is substantially stable as it showed a low structural fluctuation with RMSF value of 1.2 Å. When the  $\alpha$ 4- $\alpha$ 5 loop flexibility was increased through P193G, P194G and P196G mutations, a decrease in larvicidal activity was also observed for all mutants, suggesting that loop rigidity provided by cyclic side chain of proline residues is functionally important. Further structural analysis *via* MD simulations revealed that only the most critical proline residue, Pro<sup>193</sup>, at which mutations adversely affect toxin solubility is in close contact with several surrounding residues, thus playing an additional role in structural arrangement of the Cry4Aa toxin molecule. Altogether, present data suggest that structural stability of the Cry4Aa  $\alpha$ 4- $\alpha$ 5 loop comprising the proline-rich sequence plays an essential role in the toxin function.

KEY WORDS: *Bacillus thuringiensis* /  $\delta$ -ENDOTOXIN / LARVICIDAL ACTIVITY / LOOP RIGIDITY / PROLINE-RICH SEQUENCE

121 pages

การศึกษาเชิงโครงสร้างและหน้าที่ของ proline-rich region ในส่วนเชื่อมต่อเกลียวอัลฟาที่ 4 และ 5 ของโปรตีนสารพิษ Cry4Aa จากแบคทีเรีย *Bacillus thuringiensis*

STRUCTURAL AND FUNCTIONAL CHARACTERIZATION OF THE PROLINE-RICH REGION WITHIN THE  $\alpha$ 4- $\alpha$ 5 LOOP OF THE *Bacillus thuringiensis* Cry4Aa TOXIN

ชมพูนุช อิ่มทอง 4937168 MBMG/D

ปร.ด. (อนุพันธุศาสตร์และพันธุวิศวกรรมศาสตร์)

คณะกรรมการที่ปรึกษาวิทยานิพนธ์: ชนันท อังศุชนสมบัติ, Ph.D., GERD KATZENMEIER, Ph.D., สมภพ ลีตะชีวะ, Ph.D., เฉลิมพล กาญจนวรินทร์, Ph.D.

บทคัดย่อ

ส่วนเชื่อมต่อเกลียวอัลฟาที่ 4 และ 5 ของโปรตีนสารพิษ Cry4Aa มีลักษณะเฉพาะอันประกอบด้วย proline-rich sequence ที่พบว่ามีความสำคัญต่อการฆ่าลูกน้ำยุงของโปรตีนนี้ งานวิจัยนี้ได้ศึกษาต่อยอดถึงความสำคัญเชิงโครงสร้างของ proline-rich region ซึ่งเริ่มต้นด้วยการสร้างโปรตีนกลายพันธุ์ P193V, P194V และ P196V ที่ยังคงลักษณะความไม่ชอบน้ำของกรดอะมิโนทั้งสามตำแหน่งไว้และพบว่าปริมาณการสร้างโปรตีนขนาด 130 กิโลดาลตันของโปรตีนกลายพันธุ์ทั้งสามชนิดในเชื้อ *Escherichia coli* นั้นเท่ากับของโปรตีนต้นแบบ (wild type) ซึ่งเมื่อนำไปทดสอบความสามารถในการฆ่าลูกน้ำยุงลาย *Aedes aegypti* พบว่า *E. coli* ที่สร้างโปรตีนกลายพันธุ์ทั้งสามชนิดสูญเสียความเป็นพิษต่อลูกน้ำยุงลายอย่างมีนัยสำคัญ ซึ่งให้เห็นว่าความไม่ชอบน้ำของ proline เพียงอย่างเดียวไม่เพียงพอต่อความเป็นพิษของโปรตีน การจำลองการเคลื่อนไหวของโปรตีน Cry4Aa ในสารละลาย KCl แสดงให้เห็นว่าส่วนเชื่อมต่อเกลียวอัลฟาที่ 4 และ 5 มีความเสถียรอย่างมาก และเมื่อศึกษาเพิ่มเติมโดยการเพิ่มความยืดหยุ่นของส่วนเชื่อมต่อเกลียวอัลฟาที่ 4 และ 5 โดยการแทนที่ Pro<sup>193</sup>, Pro<sup>194</sup> หรือ Pro<sup>196</sup> ด้วย glycine พบว่าโปรตีนกลายพันธุ์ทั้งสามชนิดนี้มีความเป็นพิษต่อลูกน้ำยุงลดลง ซึ่งบ่งชี้ว่าความเสถียรของส่วนเชื่อมต่อเกลียวอัลฟาที่เกิดจาก proline มีความสำคัญต่อความเป็นพิษของโปรตีน นอกจากนี้การจำลองการเคลื่อนไหวของโปรตีน Cry4Aa ในสารละลายแสดงให้เห็นว่า Pro<sup>193</sup> ยังมีบทบาทในการจัดเรียงโครงสร้างของโมเลกุลโปรตีนให้เหมาะสม ผลการทดลองทั้งหมดนี้แสดงให้เห็นว่าโครงสร้างที่เสถียรของส่วนเชื่อมต่อเกลียวอัลฟาที่ 4 และ 5 ที่ประกอบด้วย proline-rich sequence มีบทบาทสำคัญในการแสดงความเป็นพิษต่อลูกน้ำยุงของโปรตีน Cry4Aa

## CONTENTS

	<b>Page</b>
<b>ACKNOWLEDGEMENTS</b>	<b>iii</b>
<b>ABSTRACT (ENGLISH)</b>	<b>iv</b>
<b>ABSTRACT (THAI)</b>	<b>v</b>
<b>LIST OF TABLES</b>	<b>xi</b>
<b>LIST OF FIGURES</b>	<b>xii</b>
<b>LIST OF ABBREVIATIONS</b>	<b>xv</b>
<b>CHAPTER I INTRODUCTION</b>	<b>1</b>
<b>CHAPTER II LITERATURE REVIEW</b>	<b>4</b>
2.1 <i>Bacillus thuringiensis</i> $\delta$ -endotoxins	4
2.2 Structure of Cry toxins	4
2.3 Mechanism of action of Cry toxins	5
2.3.1 Inclusion solubilization and proteolytic activation	5
2.3.2 Toxin-receptor binding	6
2.3.3 Membrane insertion and toxin oligomerization	7
2.3.4 Membrane permeabilization and pore formation	11
<b>CHAPTER III MATERIALS AND METHODS</b>	<b>12</b>
3.1 Materials	12
3.1.1 Chemicals and reagents	12
3.1.2 Enzymes	12
3.1.3 Bacterial strain	12
3.1.4 Plasmids	13
3.1.5 Synthetic oligonucleotides	16
3.1.6 Culture media	18
3.1.7 Solutions for analyzing phosphorus content	19
3.1.8 Instruments	19
3.1.9 Miscellaneous	19

**CONTENTS (cont.)**

	<b>Page</b>
3.2 Methods	20
3.2.1 Plasmid DNA extraction using CTAB method	20
3.2.2 Agarose gel electrophoresis of DNA	20
3.2.3 Site-directed mutagenesis	21
3.2.4 Digestion of PCR products	24
3.2.5 Preparation of competent cells	24
3.2.6 Transformation of plasmid DNA into competent cells	24
3.2.7 Mutant plasmid screening	25
3.2.8 DNA sequencing	25
3.2.9 Expression of toxins	25
3.2.10 SDS-polyacrylamide gel electrophoresis	26
3.2.11 Isolation of protoxin inclusions	26
3.2.11.1 Inclusion isolation using distilled water	26
3.2.11.2 Inclusion isolation using 100 mM KH <sub>2</sub> PO <sub>4</sub> , pH 5.0	26
3.2.12 Determination of protein concentrations	27
3.2.13 Solubilization of toxin inclusion and proteolytic digestion	27
3.2.14 Precipitation of soluble protoxin	27
3.2.15 Mosquito-larvicidal activity assay	28
3.2.16 Purification of Cry4Aa toxin and its mutants	28
3.2.17 Intrinsic fluorescence measurement	29
3.2.18 Identification of disulfide bond-containing peptides	29

## CONTENTS (cont.)

	<b>Page</b>
3.2.19 Membrane perturbation assays	29
3.2.19.1 Preparation of calcein-entrapped hybrid liposomes	29
3.2.19.2 Phosphorus content analysis of phospholipid	30
3.2.19.3 Calcein release assays	30
3.2.20 Molecular dynamics (MD) simulations	31
<b>CHAPTER IV RESULT I: ISOLATION OF Cry4Aa INCLUSION</b>	<b>32</b>
4.1 Isolation of Cry4Aa protoxin inclusion from <i>E. coli</i> cells	32
4.2 Precipitation of Cry4Aa inclusion from its soluble protoxin	36
<b>CHAPTER V RESULT II: MUTAGENESIS OF PROLINE RESIDUES WITHIN <math>\alpha 4</math>-<math>\alpha 5</math> LOOP OF Cry4Aa TOXIN</b>	<b>39</b>
5.1 Constructions of valine-substituted Cry4Aa mutant plasmids	39
5.2 Expression of valine-substituted Cry4Aa mutant toxins	40
5.3 Solubilization and proteolytic processing of valine-substituted Cry4Aa mutant toxins	40
5.4 Mosquito-larvicidal activity of valine-substituted Cry4Aa mutant toxins	41
5.5 Constructions of glycine-substituted Cry4Aa mutant plasmids	50
5.6 Expression of glycine-substituted Cry4Aa mutant toxins	50
5.7 Solubilization and proteolytic processing of glycine-substituted Cry4Aa mutant toxins	50
5.8 Mosquito-larvicidal activity of glycine-substituted Cry4Aa mutant toxins	51
5.9 Constructions of Cry4Aa mutant plasmids substituted at the position 193	60

## **CONTENTS (cont.)**

	<b>Page</b>
5.10 Expression of Cry4Aa mutant toxins substituted at the position 193	60
5.11 Solubilization of Cry4Aa mutant toxins substituted at the position 193	61
5.12 Mosquito-larvicidal activity of Cry4Aa mutant toxins substituted at the position 193	61
 <b>CHAPTER VI RESULT III: PROLINE-SCANNING MUTAGENESIS</b>	
<b>IN <math>\alpha</math>4-<math>\alpha</math>5 LOOP OF Cry4Aa TOXIN</b>	<b>70</b>
6.1 Constructions of proline-substituted Cry4Aa mutant plasmids	70
6.2 Expression of proline-substituted Cry4aa mutant toxins	70
6.3 Solubilization and proteolytic processing of proline-substituted Cry4Aa mutant toxins	71
6.4 Mosquito-larvicidal activity of proline-substituted Cry4Aa mutant toxins	71
 <b>CHAPTER VII RESULT IV: CHARACTERIZATION OF Cry4Aa AND ITS MUTANT TOXINS</b>	
<b>7.1 Purification of Cry4Aa and its glycine-substituted mutant toxins</b>	<b>85</b>
7.2 Structural determination of Cry4Aa and its glycine-substituted mutant toxins	85
7.3 Disulfide bond determination of Cry4Aa and its glycine-substituted mutant toxins	86
7.4 Membrane-perturbing activity of Cry4Aa and its glycine-substituted mutant toxins	86
7.5 Structural analysis of Cry4Aa and its mutant toxins substituted at the position 193	86
7.6 RMSF value determination of Cry4Aa-domain I	87

**CONTENTS (cont.)**

	<b>Page</b>
<b>CHAPTER VIII DISCUSSION</b>	<b>100</b>
8.1 Effects of pH on formation of Cry4Aa protoxin inclusion	100
8.2 Hydrophobic feature of proline-rich sequence located in Cry4Aa $\alpha$ 4- $\alpha$ 5 loop	101
8.3 Structural importance of proline-rich sequence for Cry4Aa activity	102
8.4 Additional importance of Pro <sup>193</sup> for structural arrangement of Cry4Aa toxin molecule	104
8.5 Structure-stability relationships of the long Cry4Aa $\alpha$ 4- $\alpha$ 5 loop	105
<b>CHAPTER IX CONCLUSIONS</b>	<b>108</b>
<b>REFERENCES</b>	<b>110</b>
<b>BIOGRAPHY</b>	<b>121</b>

## LIST OF TABLES

<b>Tables</b>	<b>Page</b>
3.1 Temperature cycling parameters for site-directed mutagenesis	22
3.2 Annealing temperature ( $T_a$ ) for each pair of mutagenic primers	23

## LIST OF FIGURES

<b>Figures</b>	<b>Page</b>
1.1 Cry4Aa structure, illustrating structural features of the $\alpha$ 4- $\alpha$ 5 loop	3
2.1 Ribbon illustrations of various Cry toxin structures	9
2.2 Schematic presentation of an umbrella-like model for membrane-bound state of Cry toxins	10
3.1 Schematic map of the pMEx-8 plasmid	14
3.2 Schematic map of the pMEx-B4A recombinant plasmid	15
4.1 Phase-contrast micrographs of <i>E. coli</i> cells harboring pMEx-8 or pMEx-B4A	33
4.2 Protein profiles of extracted protein fractions from <i>E. coli</i> cells suspended in distilled water or 100 mM KH <sub>2</sub> PO <sub>4</sub>	34
4.3 Alkaline solubility and proteolytic stability of Cry4Aa inclusion	35
4.4 Alkaline solubility and proteolytic stability of precipitated Cry4Aa inclusion	37
4.5 Larvicidal activity of <i>E. coli</i> cells expressing Cry4Aa toxin and of precipitated Cry4Aa inclusion	38
5.1 PCR amplification of Cry4Aa mutant plasmids: pP193V, pP194V and pP196V	42
5.2 Restriction digestion and DNA sequencing of pP193V	43
5.3 Restriction digestion and DNA sequencing of pP194V	44
5.4 Restriction digestion and DNA sequencing of pP196V	45
5.5 Expression of Cry4Aa and its valine-substituted mutants	46
5.6 Alkaline solubility of Cry4Aa and its valine-substituted mutant inclusions	47
5.7 Trypsin-digested products of Cry4Aa and its valine-substituted mutants	48
5.8 Larvicidal activity of Cry4Aa and its valine-substituted mutants	49
5.9 PCR amplification of Cry4Aa mutant plasmids: pP193G, pP194G and pP196G	52
5.10 Restriction digestion and DNA sequencing of pP193G	53

## LIST OF FIGURES (cont.)

<b>Figures</b>	<b>Page</b>
5.11 Restriction digestion and DNA sequencing of pP194G	54
5.12 Restriction digestion and DNA sequencing of pP196G	55
5.13 Expression of Cry4Aa and its glycine-substituted mutants	56
5.14 Alkaline solubility of Cry4Aa and its glycine-substituted mutant inclusions	57
5.15 Trypsin-digested products of Cry4Aa and its glycine-substituted mutants	58
5.16 Larvicidal activity of Cry4Aa and its glycine-substituted mutants	59
5.17 Close-up views of part of Cry4Aa structure, illustrating orientation of Pro <sup>193</sup> and Tyr <sup>133</sup>	62
5.18 PCR amplification of Cry4Aa mutant plasmids: pP193F, pP193W and pP193Y	63
5.19 Restriction digestion and DNA sequencing of pP193F	64
5.20 Restriction digestion and DNA sequencing of pP193W	65
5.21 Restriction digestion and DNA sequencing of pP193Y	66
5.22 Expression of Cry4Aa and its mutants substituted at the position 193	67
5.23 Alkaline solubility of Cry4Aa and its mutant inclusions substituted at the position 193	68
5.24 Larvicidal activity of Cry4Aa and its mutants substituted at the position 193	69
6.1 PCR amplification of Cry4Aa mutant plasmids: pS191P, pC192P, pN195P, pS197P, pD198P, pC199P and pD200P	72
6.2 Restriction digestion and DNA sequencing of pS191P	73
6.3 Restriction digestion and DNA sequencing of pC192P	74
6.4 Restriction digestion and DNA sequencing of pN195P	75
6.5 Restriction digestion and DNA sequencing of pS197P	76
6.6 Restriction digestion and DNA sequencing of pD198P	77
6.7 Restriction digestion and DNA sequencing of pC199P	78
6.8 Restriction digestion and DNA sequencing of pD200P	79

## LIST OF FIGURES (cont.)

<b>Figures</b>	<b>Page</b>
6.9 Expression of Cry4Aa and its proline-substituted mutants	80
6.10 Alkaline solubility of Cry4Aa and its proline-substituted mutant inclusions	81
6.11 Alkaline solubility of proline-substituted Cry4Aa mutant inclusions	82
6.12 Trypsin-digested products of Cry4Aa and its proline-substituted mutants	83
6.13 Larvicidal activity of Cry4Aa and its proline-substituted mutants	84
7.1 Chromatogram and SDS-PAGE analysis of purified Cry4Aa toxin	88
7.2 Chromatogram and SDS-PAGE analysis of purified P193G mutant	89
7.3 Chromatogram and SDS-PAGE analysis of purified P194G mutant	90
7.4 Chromatogram and SDS-PAGE analysis of purified P196G mutant	91
7.5 Intrinsic fluorescence spectra of Cry4Aa and its glycine-substituted mutants	92
7.6 Band-shift of Cry4Aa and its glycine-substituted mutants	93
7.7 Relative calcein release activity of Cry4Aa	94
7.8 Relative calcein release activity of Cry4Aa and its glycine-substituted mutants	95
7.9 Close-up view of part of Cry4Aa structure, illustrating side-chain direction of proline residues within the $\alpha$ 4- $\alpha$ 5 loop	96
7.10 Close-up views of part of Cry4Aa structure, illustrating interactions between residues at position 193 and their neighboring residues within 5 Å	97
7.11 Snapshots from MD simulations of Cry4Aa and its mutants, illustrating structural arrangement around position 193	98
7.12 RMSF value of Cry4Aa-domain I from MD simulations	99
8.1 Two different views of Cry4Aa trimeric structure, illustrating position of loop proline clusters within the molecule	107

## LIST OF ABBREVIATIONS

% (w/v)	Percent weight by volume
sec	Second (s)
ns	Nanosecond (s)
ps	Picosecond (s)
fs	Femtosecond (s)
min	Minute (s)
hr (s)	Hour (s)
$\mu\text{m}$	Micrometer (s)
nm	Nanometer (s)
Å	Angstrom (s)
g	Gram (s)
mg	Milligram (s)
$\mu\text{g}$	Microgram (s)
ng	Nanogram (s)
L	Liter (s)
ml	Milliliter (s)
$\mu\text{l}$	Microliter (s)
M	Molar (s)
mM	Millimolar (s)
$\mu\text{M}$	Micromolar (s)
pmole	Picomole (s)
psi	Pound-force per square inch
°C	Degree Celsius
K	Degree Kelvin
kb	Kilobase (s)
kDa	Kilodalton (s)
U	Unit (s)

## LIST OF ABBREVIATIONS (cont.)

<i>A. aegypti</i>	<i>Aedes aegypti</i>
BBMV	Brush-border membrane vesicles
<i>Bti</i>	<i>Bacillus thuringiensis</i> subsp. <i>israelensis</i>
CTAB	Cetyl trimethyl ammonium bromide
DNA	Deoxyribonucleic acid
DTT	1,4-Dithiothreitol
<i>E. coli</i>	<i>Escherichia coli</i>
EDTA	Ethylenediaminetetraacetic acid
FPLC	Fast performance liquid chromatography
IPTG	Isopropyl- $\beta$ -D-thiogalactopyranoside
LB	Luria Bertani medium
MD	Molecular dynamics
OD	Optical density (-ies)
PCR	Polymerase chain reaction
PDB	Protein data bank
PMSF	Phenylmethylsulphonylfluoride
RMSF	Root mean square fluctuation
RNase	Ribonuclease
rpm	Revolutions per minute
SD	Standard deviation
SDS-PAGE	Sodium dodecyl sulfate-polyacrylamide gel electrophoresis
SEM	Standard errors of the mean
T <sub>a</sub>	Annealing temperature
TAE	Tris acetate EDTA
TPCK	L-1-tosylamido-2-phenylethyl chloromethyl ketone

## CHAPTER I

### INTRODUCTION

Cry4Aa toxin is a mosquito-active protein produced from *Bacillus thuringiensis* subsp. *israelensis* (*Bti*) during sporulation as 130-kDa protoxin in the form of crystalline inclusion (1). This toxin is highly specific to mosquito larvae of genera *Aedes*, *Anopheles* and *Culex* which are vectors of dengue fever, malaria and filariasis (2).

After ingestion by susceptible mosquito larvae, inclusions of the 130-kDa Cry protoxins are solubilized under alkaline conditions of larval midgut lumen. The resulting soluble protoxins are subsequently processed by larval gut proteases to yield 65-kDa active toxins (3). The activated toxins then bind to specific receptors located on the midgut epithelial cell membrane and thus are able to insert into the membrane to form ion-leakage pores, resulting in osmotic cell lysis and eventual death of the target insect-larvae (4-5).

Similar to other known Cry toxins, the 65-kDa Cry4Aa active toxin is composed of three distinct domains:  $\alpha$ -helical domain (I),  $\beta$ -prism domain (II) and  $\beta$ -sandwich domain (III) (**Figure 1.1A**) (6). It was widely agreed that the Cry-domain I is responsible for membrane-inserting and pore-forming activities of the toxins while the domain II is involved in receptor recognition. Based on the umbrella-like model (7), the best description for the membrane-bound state of the Cry toxins, helices 4 and 5 of the domain I penetrate the membrane as a helical hairpin structure. The transmembrane  $\alpha$ 4- $\alpha$ 5 hairpins subsequently combine together to form an oligomeric pore (8) in which helix 4 faces the pore lumen and participates in ion conduction (9-10), whereas helix 5 interacts with the lipid membranes and is involved in toxin oligomerization (11-12).

Loop connecting the transmembrane helices 4 and 5 was shown to be structurally required for membrane-perturbing activity of Cry toxins (13). This finding was supported by the evidence that one highly conserved tyrosine residue within the

$\alpha$ 4- $\alpha$ 5 loop of two closely related mosquito-larvicidal toxins (Cry4Aa: Tyr<sup>202</sup>; Cry4Ba: Tyr<sup>170</sup>) plays a crucial role in toxicity, conceivably by stabilizing the oligomeric pore structure *via* an interaction with the phospholipid head groups (14-15).

Of particular interest among known Cry toxins, the Cry4Aa toxin possesses an extraordinarily long  $\alpha$ 4- $\alpha$ 5 loop with unique structural features: a proline-rich sequence (Pro<sup>193</sup>Pro<sup>194</sup>Pro<sup>196</sup>), a disulfide bond (Cys<sup>192</sup>-Cys<sup>199</sup>) and a short  $\alpha$ -helical structure (Pro<sup>196</sup> to Ile<sup>204</sup>) (**Figure 1.1**) (6). The proline-rich sequence as well as the disulfide bond was previously displayed to be required for larvicidal activity of the Cry4Aa toxin (16). In this study, importance of the Cry4Aa  $\alpha$ 4- $\alpha$ 5 loop structure, particularly the proline-rich sequence, was further investigated by mutagenic and computational analysis.



## CHAPTER II

### LITERATURE REVIEW

#### 2.1 *Bacillus thuringiensis* $\delta$ -endotoxins

*Bacillus thuringiensis* (*Bt*), a Gram-positive spore-forming bacterium, produces crystalline inclusions during sporulation. These inclusions are composed of one or more insect-larvicidal proteins known as  $\delta$ -endotoxins which are specifically active to larvae of several important insect crop pests as well as disease vectors (21). Due to high specificity and environmental safety, *Bt* becomes a promising biological alternative to traditional chemical pesticides (22).

*Bt*  $\delta$ -endotoxins can be classified into two major groups, Cry (crystal) and Cyt (cytolytic) toxins, according to the similarity of their deduced amino acid sequences and insect-larvicidal spectra (21). The Cry toxins (70-130 kDa) are specific to several insect larvae (4, 21) in the orders of Diptera (mosquitoes and flies), Lepidoptera (butterflies and moths), Coleoptera (beetles) and Hymenoptera (wasps and bees). The Cyt toxins (27-29 kDa) show cytolytic activity against a variety of invertebrate and vertebrate cell-lines *in vitro*, apart from being toxic to the larvae of dipteran insects *in vivo* (3, 23).

#### 2.2 Structure of Cry toxins

The X-ray crystal structures of different Cry toxins, *e.g.*, Cry1Aa (17), Cry3Aa (19), Cry4Aa (6) and Cry4Ba (20), reveal similar overall structures with three-domain organization (see **Figure 2.1**). The N-terminal domain I is a seven-helix bundle in which the helix 5 is relatively hydrophobic and surrounded by the six remaining helices. This domain was shown to be responsible for membrane insertion and ion-leakage pore formation (7, 11, 13, 24-27). Domain II, the most variable part of the Cry toxin structures, is composed of three antiparallel  $\beta$ -sheets, each of which terminates in surface-exposed loops. It was widely agreed that the domain II

determines target specificity of the Cry toxins as a number of loop residues in this domain have been implicated in receptor binding (28-33). Domain III is a  $\beta$ -sandwich of two antiparallel  $\beta$ -sheets. The exact role of this domain is still not clearly elucidated. Several studies showed that this domain may be involved in receptor binding (34-36). Positioning of the Cry-toxin C-terminus within the domain III is believed to be essential for maintaining structural integrity of the active toxin molecules as it may prevent further proteolytic degradation (19).

## 2.3 Mechanism of action of Cry toxins

The insect-larvicidal mechanism of the *Bt* Cry  $\delta$ -endotoxins is a multistep process including solubilization of the toxin inclusions in larval midgut, proteolytic activation of the soluble protoxins by midgut proteases, binding of the activated toxins to specific receptors located on the midgut epithelial cell membrane, insertion of the toxin into the midgut apical membrane and oligomerization of the inserted toxins to form ion-leakage pores. These pores would lead to the disruption of the osmotic balance across the cell membrane, thus resulting in cell lysis and eventual death of the target larvae.

### 2.3.1 Inclusion solubilization and proteolytic activation

*Bt* toxins are naturally produced as inactive protoxins in the form of crystalline inclusions. After ingestion by susceptible insect larvae, the toxin inclusions are solubilized in the midgut lumen which is highly alkaline in a number of dipteran and lepidopteran larvae and predominantly acidic in coleopteran larvae (4, 37). The soluble protoxins are subsequently cleaved by larval midgut proteases to yield the protease-resistant active toxins. The toxin activation can be simulated *in vitro* by incubating the Cry protoxins with larval gut extracts, trypsin or chymotrypsin (38).

The *Bt* Cry  $\delta$ -endotoxins can be categorized into two groups based on molecular mass of the protoxins. For the large Cry toxins (ca. 130 kDa), *e.g.*, Cry1 and Cry4, approximate half of the molecule (ca. 600 amino acids) is removed from C-terminus during *in vitro* proteolytic activation, leaving the N-terminal half (ca. 65 kDa) as the toxic component. Activation of these protoxins also involves removal of

approximate 30 residues from the N-terminus (39-40). Moreover, interhelical proteolysis was found for toxin activation of the dipteran-specific Cry4 toxins. For example, the 130-kDa Cry4Aa toxin was cleaved by trypsin into two major fragments of ca. 21 and 47 kDa, in addition to the removal of the C-terminal half of the protoxin. These two trypsin-resistant fragments were produced by the cleavage at Arg<sup>235</sup> located in the solvent-exposed loop connecting helices 5 and 6 within the pore-forming domain of the Cry4Aa toxin (41). In the case of the smaller Cry toxins (ca. 70 kDa), *e.g.*, Cry2 and Cry3, the proteolytic processing occurs only at the N-terminus where about 50 residues are removed (19). C-terminal protease resistance of the small Cry toxins may be due to the position of their C-termini buried in the toxin molecules (19).

### 2.3.2 Toxin-receptor binding

After inclusion solubilization and proteolytic activation in larval midgut lumen, the activated Cry toxins are believed to pass through the peritrophic membrane, a thin porous structure which separates ingested materials from gut epithelium, to bind the specific receptors located on the midgut epithelial cell membrane (4, 42). The target specificity of the *Bt*-Cry toxins was shown to be determined by these specific membrane receptors (3). To date, at least three types of Cry toxin-binding proteins have been identified as specific receptors: glycosylphosphatidylinositol (GPI)-anchored alkaline phosphatase (ALP), GPI-anchored aminopeptidase-N (APN) and cadherin-like protein.

The 62-kDa and 68-kDa ALPs isolated from *Manduca sexta* and *Heliothis virescens* larvae were identified as a Cry1Ac binding protein (43-44). The 65-kDa GPI-anchored ALP from *Aedes aegypti* larvae was characterized as a functional receptor for the *Bti* Cry11Aa toxin since interfering interaction between the ALP and the Cry11Aa toxin reduced the toxin bioactivity (45). Recently, it was shown that *A. aegypti* ALP heterologously expressed in *Spodoptera frugiperda* (*Sf9*) cells as 58-kDa membrane-bound protein (*Aa*-mALP) can interact with Cry4Ba toxin (46). Moreover, the *Aa*-mALP-expressing cells showed susceptibility to the Cry4Ba toxin.

The 120-kDa GPI-anchored APN from *M. sexta* larvae was shown to recognize Cry1Aa, Cry1Ab and Cry1Ac (47). GPI-anchored APN was also identified as a Cry1Aa-binding protein in *Bombyx mori* larvae (48). It was suggested that the

170-kDa GPI-anchored APN from *H. virescens* larvae is a functional receptor for Cry1A toxins as the APN reconstituted into phospholipid vesicles can promote toxin-induced  $^{86}\text{Rb}^+$  release for Cry1A toxins (49). Furthermore, the 106-kDa GPI-anchored APN was proposed to be a putative receptor for the Cry11Ba toxin in *Anopheles gambiae* larvae since feeding the larvae with mixtures of the toxin and the truncated APN reduced the larvicidal activity (50).

A 175-kDa cadherin-like protein (BtR175) was identified as a Cry1Aa-binding protein in *B. mori* larvae (51). By introducing the BtR175 into Cry1Aa-insusceptible cells, the cells became sensitive to the toxin (52). Cadherin-like proteins from *Tenebrio molitor* and *Tribolium castaneum* larvae (*TmCad1* and *TcCad1*) were characterized as a functional receptor for Cry3Aa and Cry3Ba, respectively, since RNA interference knockdown of the two cadherin-like proteins resulted in decreased toxin susceptibility of the larvae (53-54). Also, it was suggested that a cadherin-like protein from *A. gambiae* larvae (BT-R<sub>3</sub>) is a receptor for Cry4Ba as binding of the Cry4Ba toxin to BT-R<sub>3</sub> expressed in High Five<sup>TM</sup> insect cells triggered cytotoxic events and hence cell death (55).

Domain II of Cry toxins has been shown to be involved in receptor binding, hence determining target specificity. Surface-exposed loops connecting  $\beta 6$ - $\beta 7$  and  $\beta 10$ - $\beta 11$  within domain II of Cry1Ab were identified as an epitope for interacting with *M. sexta* cadherin-like BT-R<sub>1</sub> receptor (56-57). It was demonstrated that *Culex* toxicity can be introduced into *Culex*-inactive Cry1Aa and Cry4Ba by amino acid substitutions in domain-II loops of the toxins (58-59).

The involvement of Cry-domain III in receptor binding was also reported. It was shown that Cry1Ac binds to a putative APN receptor from *M. sexta* via a site on domain III of the toxin (36, 60). Also, domain III of Cry1Ab was shown to be involved in the interaction with *M. sexta* APN receptor (57).

### 2.3.3 Membrane insertion and toxin oligomerization

Upon binding to the specific receptors, it is believed that substantial structural rearrangements of the bound toxins occur, thus allowing their pore-forming portion to insert into the target cell membrane. Oligomerization of the inserted toxins is related to formation of the ion-leakage pores which cause osmotic cell lysis (4).

An umbrella-like model has been proposed to describe the membrane-associated state of the Cry toxins (7). In this model,  $\alpha 4$  and  $\alpha 5$  insert into the membrane as a helical hairpin, while the remaining helices spread on the membrane surface like the ribs of an umbrella (**Figure 2.2**). On the basis of energy considerations, the  $\alpha 4$ - $\alpha 5$  helical hairpin of Cry1Aa was predicted to insert spontaneously into the membrane (61). Moreover, it was suggested that the  $\alpha 4$  and  $\alpha 5$  are buried within the membrane after incubation of the Cry1Aa toxin with brush-border membrane vesicles (BBMV) from *B. mori* larvae (62). Interestingly, membrane permeation study with Cry1Ac revealed that the  $\alpha 4$ -loop- $\alpha 5$  segment is more active than either the isolated helices or their mixtures, suggesting requirement of the  $\alpha 4$ - $\alpha 5$  connecting loop for efficient membrane insertion of the toxin (13).

Upon incubation of Cry1Ab and Cry1Ac with *M. sexta* BBMV, toxin aggregates of ca. 200 kDa were observed, suggesting occurrence of toxin oligomerization (63). There is evidence from AFM studies that the 65-kDa activated Cry4Ba toxin spontaneously inserts into receptor-free lipid bilayers and forms pore-like tetrameric structures (64). Later, it was, however, revealed by electron crystallography that the 65-kDa Cry4Ba toxin exists in the lipid membrane as trimeric structures (65). Furthermore, by using molecular dynamics (MD) simulations, the trimeric structure of Cry4Aa which is closely related to the Cry4Ba toxin was found to be stable in solution on 10-ns timescale (66).

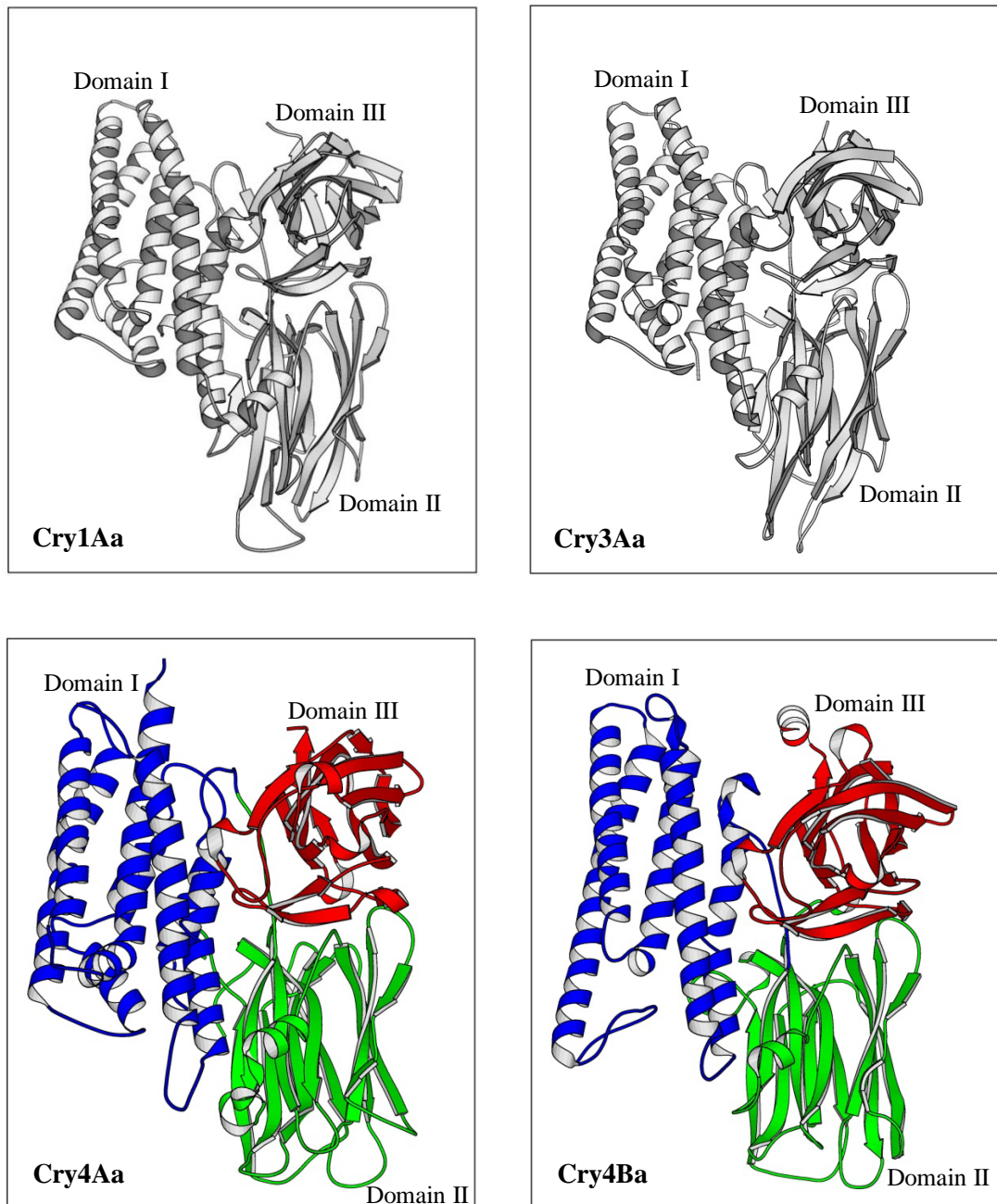


**Figure 2.1** Ribbon illustrations of various Cry toxin structures

The figure shows side view of 3D structures of Cry1Aa (17), Cry3Aa (19), Cry4Aa (6) and Cry4Ba (20) toxins determined by X-ray crystallography. These ribbon illustrations demonstrate high similarity in their overall structures with three-domain organization.

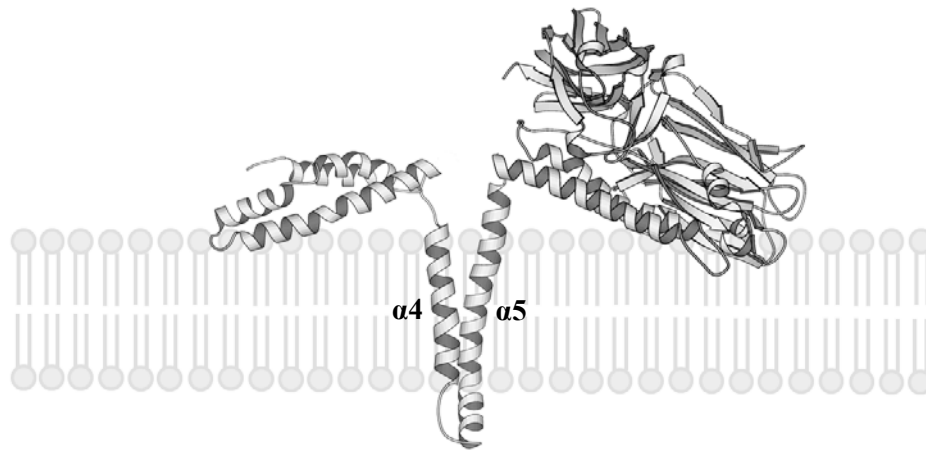


**Figure 2.2** Schematic presentation of an umbrella-like model for membrane-bound state of Cry toxins

The figure shows a model of the Cry toxin's orientation within phospholipid membrane, suggested by Gazit *et al* (7).  $\alpha 4$  and  $\alpha 5$  helices in domain I penetrate into the membrane as a helical hairpin while the remaining parts lie on the membrane surface.

### 2.3.4 Membrane permeabilization and pore formation

Lytic pore formation is a key step in mechanism of action of the Cry toxins. Through a variety of techniques, membrane-permeabilizing and pore-forming abilities of the toxins have been examined.

Membrane permeation studies by using entrapped dye-release assays revealed that Cry1Ab can disrupt receptor-free liposomes. Moreover, a great increase in Cry1Ab-mediated disruption was found when proteins from *B. mori* BBMV were reconstituted into liposomes (67). It was demonstrated that peptides corresponding to the  $\alpha$ 4-loop- $\alpha$ 5 hairpin of Cry1Ac and Cry4Ba can induce leakage of entrapped calcein from liposomes, indicating direct involvement of this  $\alpha$ 4- $\alpha$ 5 hairpin in membrane perturbation and pore formation (13, 68).

Several studies employed osmotic swelling assays to monitor permeability change of insect-larval midgut BBMV upon incubation with Cry toxins. It was found that Cry1Ac produced a marked change in membrane permeability of *M. sexta* BBMV (69). Tran *et al.* (70) examined the membrane-permeabilizing effects of Cry1Ac and Cry1Ca in *M. sexta* BBMV over a wide range of pHs and found that pore-forming activity of both toxins varied as a function of pH.

Various activated Cry toxins have been shown to form ion channels in planar lipid bilayers (PLBs). In PLBs where *M. sexta* receptors were reconstituted, ion channel activity was observed following addition of Cry1Aa, Cry1Ac or Cry1C at doses less than those required to form ion channels in receptor-free PBLs, suggesting that reconstituted receptors catalyze channel formation in phospholipid membrane (71). Moreover, Peyronnet *et al.* (72) estimated the size of ion channels formed in PLBs by using the non-electrolyte exclusion technique and polyethylene glycols of various molecular weights and found that Cry1C formed ion channels with pore radius of ca. 10 Å. Puntheeranurak *et al.* (73) demonstrated that both Cry4Ba and its  $\alpha$ 1- $\alpha$ 5 fragment formed cation-selective channels in PLBs, indicating that the  $\alpha$ 1- $\alpha$ 5 region of the domain I is the major determinant of Cry4Ba pore formation.

## CHAPTER III

### MATERIALS AND METHODS

#### 3.1 Materials

##### 3.1.1 Chemicals and reagents

Ampicillin	Sigma
Bromophenol blue	Sigma
Calcium chloride	Sigma
Cetyl trimethyl ammonium bromide (CTAB)	Sigma
Coomassie brilliant blue R-250	Sigma
1,4-Dithiothreitol (DTT)	Sigma
Isopropyl- $\beta$ -D-thiogalactopyranoside (IPTG)	Sigma

All other unlisted chemicals are analytical grade purchased from various suppliers (Bio-Rad, Merck and Sigma)

##### 3.1.2 Enzymes

Phusion DNA polymerase	Finnzymes
Trypsin (TPCK-treated)	Sigma
RNaseA	Sigma
Restriction endonucleases, <i>i.e.</i> , <i>Ava</i> I, <i>Dde</i> I, <i>Dpn</i> I, <i>Hae</i> III, <i>Hinc</i> II, <i>Hpa</i> II, <i>Pvu</i> II, <i>Rsa</i> I, <i>Sau</i> 3AI	Promega

##### 3.1.3 Bacterial strain

*Escherichia coli* strain **JM109** [*endA*1, *recA*1, *gyrA*96, *thi*, *hsdR*17, ( $r_K^-$ ,  $m_K^+$ ), *relA*1, *supE*44,  $\lambda^-$ ,  $\Delta(lac-proAB)$ , (F, *traD*36, *proAB*<sup>+</sup>, *lacI*<sup>q</sup>, *lacZ* $\Delta$ M15)] purchased from Promega was used as a recombinant plasmid host.

### 3.1.4 Plasmids

**pMEx-8 (Figure 3.1):** the expression vector containing the *tac* promoter and the ampicillin resistance (*bla*) gene was used as a negative control.

**pMEx-B4A (Figure 3.2):** the recombinant plasmid containing the 130-kDa Cry4Aa toxin gene (GenBank accession number: Y00423) under control of the *cry4Ba* regulatory region and the *tac* promoter was used as a DNA template for site-directed mutagenesis.

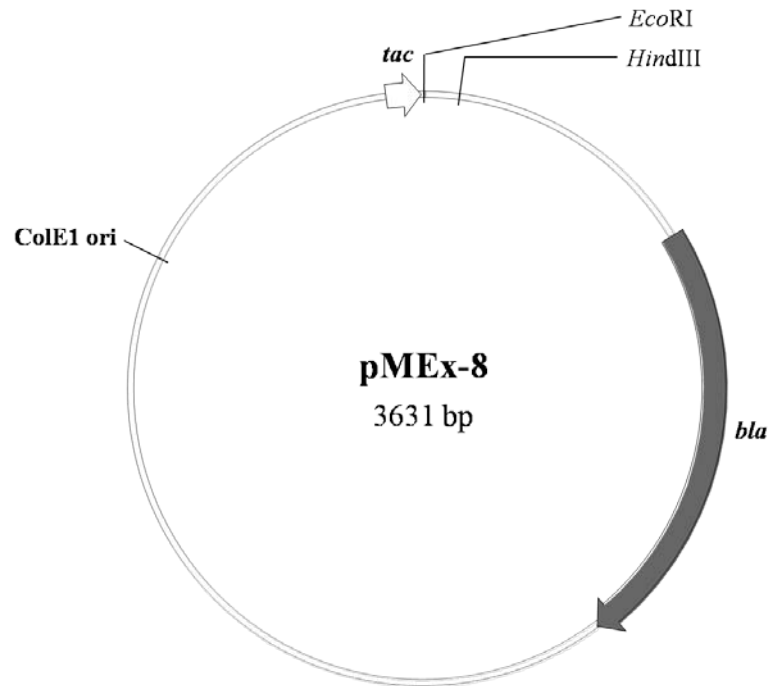


**Figure 3.1** Schematic map of the pMEx-8 plasmid (74)

The figure illustrates the pMEx-8 plasmid containing the *tac* promoter (white arrow), *ColE1 ori* origin of replication and ampicillin resistance (*bla*) gene (dark gray arrow). For clarity, not all of the restriction sites are shown.

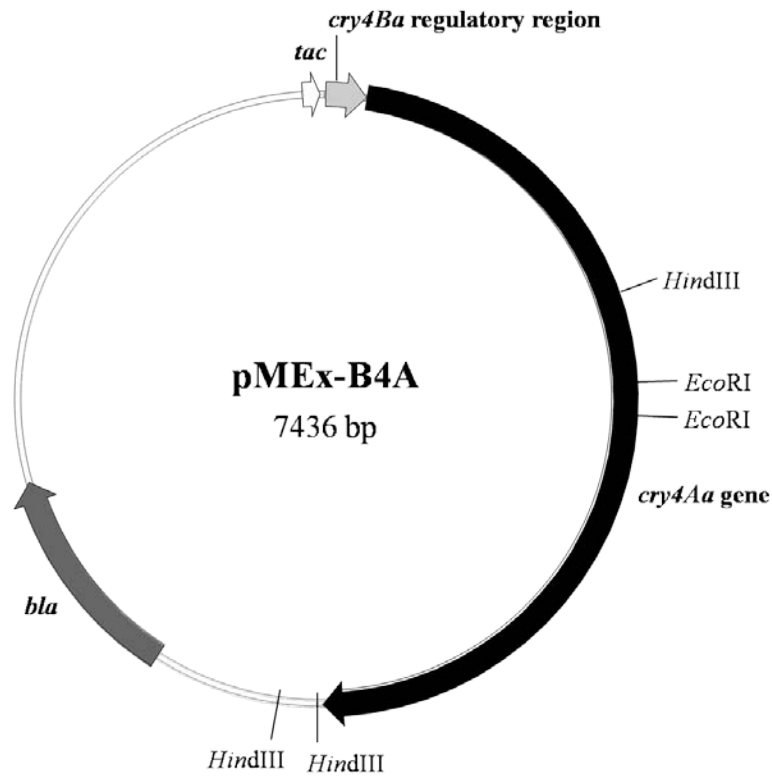


**Figure 3.2 Schematic map of the pMEx-B4A recombinant plasmid (41)**

The figure illustrates the pMEx-B4A recombinant plasmid containing the 130-kDa Cry4Aa toxin gene (black arrow) under control of the *cry4Ba* regulatory region (gray arrow) and the *tac* promoter (white arrow). The thin line represents the pMEx-8 vector containing the ampicillin resistance (*bla*) gene (dark gray arrow). For clarity, not all of the restriction sites are shown.

### 3.1.5 Synthetic oligonucleotides

All synthetic oligonucleotides serving as primers were purchased from Sigma Proligo (Singapore). The sequences of all oligonucleotides are shown below. Mutated nucleotides and amino acid residues are indicated as bold letters. Introduced restriction enzyme recognition sites are underlined. Single-code amino acid letters are placed above their corresponding nucleotide sequences.

	S C <b>V</b> P N P S
P193V-f	5'-CTCTTGT <u><b>GTA</b></u> CCTAATCCTAGTGA-3'
P193V-r	3'-GAACATTTGAGAACA <u><b>CAT</b></u> GGATTAG-5' <i>RsaI</i>
	C P <b>V</b> N P S D
P194V-f	5'-CTTGTCC <u><b>GGT</b></u> TAATCCTAGTGATTG-3'
P194V-r	3'-CATTTGAGAACAGG <u><b>CCA</b></u> ATTAGGAT-5' <i>HpaII</i>
	P N <b>V</b> S D C D Y Y
P196V-f	5'-CTCCTAAT <u><b>GTCTCAG</b></u> ATTGCGATTACTATAAC-3'
P196V-r	3'-TGAGAACAGGAGGATTAC <u><b>CAGAGT</b></u> CTAACGC-5' <i>DdeI</i>
	N S C <b>G</b> P N P S D
P193G-f	5'-AAACTCTTGT <u><b>GGGCC</b></u> CAATCCTAGTGATTG-3'
P193G-r	3'-GAACATTTGAGAACA <u><b>CCCGGG</b></u> TTAGGATCAC-5' <i>HaeIII</i>
	C P <b>G</b> N P S D
P194G-f	5'-TTGTCC <u><b>GGG</b></u> TAATCCTAGTGATTG-3'
P194G-r	3'-CATTTGAGAACAGG <u><b>CCC</b></u> ATTAGGAT-5' <i>HpaII</i>
	P N <b>G</b> S D C D Y
P196G-f	5'-TCCTAAT <u><b>GGATC</b></u> TGATTGCGATTACTA-3'
P196G-r	3'-GAACAGGAGGATTAC <u><b>CCTAG</b></u> ACTAACG-5' <i>Sau3AI</i>

L V N S C **F** P N P SP193F-f 5'-AGCTTGTA AACCAGCTGTTTCCTAATCCTAGTG-3'P193F-r 3'-GTCTCGAACATTTGTCGACAAAGGATTAGGAT-5'  
*PvuII*L V N S C **W** P N P SP193W-f 5'-AGCTTGTA AACCAGCTGTTGGCCTAATCCTAGTG-3'P193W-r 3'-GTCTCGAACATTTGTCGACAACCGGATTAGGAT-5'  
*PvuII*L V N S C **Y** P N P SP193Y-f 5'-AGCTTGTA AACCAGCTGTTATCCTAATCCTAGTG-3'P193Y-r 3'-GTCTCGAACATTTGTCGACAATAGGATTAGGAT-5'  
*PvuII*L V N **P** C P P NS191P-f 5'-AGCTTGTTTAACCCTTGTCTCCTAATC-3'S191P-r 3'-GTAAGGTCTCGAACAATTGGGAACAGG-5'  
*HincII*L V N S **P** P P N P SC192P-f 5'-AGCTTGTTTAACTCTCCTCCTAATCCTAGTG-3'C192P-r 3'-CAGTAAGGTCTCGAACAATTGAGGGAGGAGG-5'  
*HincII*P P **P** P S D C D YN195P-f 5'-TCCTCCTCCCCGAGTGATTGCGATTACTA-3'N195P-r 3'-TTTGAGAACAGGAGGAGGGGGCTCACTAAC-5'  
*AvaI*N P **P** D C D Y YS197P-f 5'-CTAATCCTCCGGATTGCGATTACTATA-3'S197P-r 3'-CAGGAGGATTAGGAGGGCTAACGC-5'  
*HpaII*

P N P S P C D Y Y N I

D198P-f 5'-CTCCTAACCCGAGTCCTTGCATTACTATAACATAC-3'

D198P-r 3'-ATTTGAGAACAGGAGGATTGGGCTCAGGAACGCTA-5'  
AvaI

S D P D Y Y N

C199P-f 5'-CTAGTGATCCCGATTACTATAACAT-3'

C199P-r 3'-GATTAGGATCACTAGGGCTAATGA-5'  
DpnI

D C P Y Y N I L

D200P-f 5'-TGATTGCCGTACTATAACATACTAG-3'

D200P-r 3'-TAGGATCACTAACGGGCATGATATTG-5'  
RsaI

### 3.1.6 Culture media

#### Luria Bertani (LB) broth and agar (75)

1 L of LB broth contains 10 g of peptone, 5 g of bacto-yeast extract and 10 g of NaCl. LB agar was prepared by adding 15 g of bacto-agar in 1 L of LB broth. The medium was sterilized by autoclaving at 121°C, 15 psi for 20 min. For selective medium, ampicillin was added to a final concentration of 100 µg/ml.

### 3.1.7 Solutions for analyzing phosphorus content

#### Ammonium molybdate-H<sub>2</sub>SO<sub>4</sub> solution (100 ml)

Ammonium molybdate	4.31 g
H <sub>2</sub> SO <sub>4</sub>	28 ml
Distilled water	72 ml

Ammonium molybdate was dissolved well in distilled water and then added with H<sub>2</sub>SO<sub>4</sub>. This solution should be prepared in prechilled container.

#### Phosphorus content assay solution (10 ml)

Ascorbic acid	0.15 g
Distilled water	9.2 ml
Ammonium molybdate-H <sub>2</sub> SO <sub>4</sub> solution	0.8 ml

This solution should be prepared freshly before assay.

### 3.1.8 Instruments

Automatic microplate reader	Spectra MAX 190
Cell incubators	Heraeus
Centrifuges	TOMY/Sorvall
FPLC system	Thermo Electron Corporation
Geldoc system	BioDoc-IT™
Jasco FP-6300 spectrofluorometer	Jasco Inc.
Thermal cycler	Bio-Rad
Spectrophotometer	Pharmacia

### 3.1.9 Miscellaneous

Bradford protein assay reagent	Bio-Rad
Deoxyribonucleotide triphosphates (dNTP)	Promega
DNA molecular mass standards	Bio-Rad
Protein concentrator	PALL
Protein molecular mass standards, broad range	Bio-Rad
Superose 12 GL 10/300 column	GE Healthcare Life Sciences

## 3.2 Methods

### 3.2.1 Plasmid DNA extraction using CTAB method (76)

A single colony of *E. coli* clones was inoculated into 3-ml LB broth containing 100 µg/ml ampicillin and incubated at 37°C with 250 rpm shaking for 16-20 hrs. Cell culture was then transferred into a microcentrifuge tube and centrifuged at 12,000 rpm for 15 sec. The pellet was resuspended in 200 µl of STET buffer (8% sucrose, 0.1% Triton X-100, 50 mM EDTA and 50 mM Tris-HCl, pH 8.0). 10-µl freshly prepared lysozyme (10 mg/ml) was then added and incubated for 10 min at room temperature. The mixture was boiled for exactly 45 sec and immediately centrifuged at 12,000 rpm for 15 min at room temperature. The pellet containing cell debris and chromosomal DNA was removed by using a sterile toothpick. Plasmid DNA was recovered by adding 20 µl of 5% CTAB into the supernatant. The contents were mixed by inversion and centrifuged at 12,000 rpm for 10 min at room temperature. The pellet was resuspended in 300 µl of 1.2 M NaCl by vigorously vortexing. In order to remove RNA, 5 µl of RNaseA (10 mg/ml) was added and incubated at 37°C for 30 min. Protein was removed by addition of 300-µl chloroform, vigorous inversion and centrifugation at 12,000 rpm for 5 min at room temperature. The aqueous phase was transferred to a new microcentrifuge tube. The plasmid DNA was precipitated with 2 volumes of absolute ethanol at -20°C for 30 min and recovered by centrifugation at 12,000 rpm for 15 min at room temperature. The DNA pellet was washed with 70% ethanol. After removal of the supernatant and air drying, the DNA pellet was resuspended in 20 µl of distilled water.

### 3.2.2 Agarose gel electrophoresis of DNA

The appropriate amount of agarose powder was dissolved in 1x TAE buffer (40 mM acetic acid, 2.5 mM EDTA and 40 mM Tris-HCl, pH 8.0) under boiling temperature to ensure the homogeneity of the gel solution. When the gel mixture cooled down to about 60°C, the mixture was poured into the mold and allowed to solidify at room temperature. DNA sample was mixed with gel-loading dye (15% (w/v) Ficoll 400, 0.1% bromophenol blue and 5 mM EDTA) at ratio of 5:1 and loaded into a well of the agarose gel submerged in TAE buffer. After electrophoresis, the gel

was stained in ethidium bromide solution for 5 min and then destained in distilled water for 10 min. The DNA patterns were visualized under UV light and digitalized by Geldoc system. The amount of DNA was estimated by comparing the DNA bands with the standard DNA marker ( $\lambda$  DNA digested with *HindIII*) of known concentrations.

### 3.2.3 Site-directed mutagenesis

Site-directed mutagenesis was carried out based on the Quick Change<sup>TM</sup> Site-Directed Mutagenesis Kit (Stratagene). The recombinant plasmid, pMEx-B4A, containing the full length of *cry4Aa* gene was used as a template. The method would make use of Phusion DNA polymerase which replicates both strands of DNA plasmid with extreme fidelity (50x greater than that of ordinary *Taq* DNA polymerase) and high polymerization speed (15-30 sec/1 kb).

A thermal cycler was used to perform polymerase chain reaction (PCR) for all samples. The PCR reaction mixture (50  $\mu$ l) was composed of

DNA template	50 ng
dNTPs	50 $\mu$ M each
Forward primer	10 pmole
Reverse primer	10 pmole
5x Phusion <sup>TM</sup> HF buffer	10 $\mu$ l
Phusion DNA polymerase	1 U
Sterile distilled water making final volume to	50 $\mu$ l

The PCR was performed by following amplification conditions as shown in **Tables 3.1** and **3.2**. After the amplification reaction was finished, the PCR products were examined by agarose gel electrophoresis (0.8% gel).

**Table 3.1 Temperature cycling parameters for site-directed mutagenesis**

<b>Temperature (°C)</b>	<b>Time (min:sec)</b>	<b>Cycles</b>
95	5:00	1
95	0:30	20
T <sub>a</sub> *	1:00	
72	4:00	
72	7:00	1

\*The annealing temperature (T<sub>a</sub>) are shown in **Table 3.2**

**Table 3.2 Annealing temperature ( $T_a$ ) for each pair of mutagenic primers**

<b>Primers</b>	<b>Annealing temperature (°C)</b>
P193V	45
P194V	45
P196V	45
P193G	44
P194G	40
P196G	40
P193F	44
P193W	44
P193Y	44
S191P	45
C192P	45
N195P	45
S197P	45
D198P	45
C199P	45
D200P	45

### 3.2.4 Digestion of PCR products

Each amplified reaction was treated with 10 U of *DpnI* restriction endonuclease and incubated at 37°C for 1 hr. *DpnI* restriction endonuclease is specific to methylated and hemimethylated DNA (5'-G<sup>me</sup>A↓TC-3'). DNA isolated from almost all *E. coli* strains is *dam* methylated and thus susceptible to *DpnI* digestion. Accordingly, the *DpnI* will digest only the parental DNA template and leave mutated plasmid undigested. The *DpnI*-digested PCR products were analyzed by agarose gel electrophoresis (0.8% gel) before being transformed into *E. coli* competent cells.

### 3.2.5 Preparation of competent cells (75)

A single colony of *E. coli* strain JM109 was inoculated into 3-ml LB broth and grown at 37°C with 250-rpm shaking for 16-20 hrs. 1 ml of the culture was transferred into 100 ml of fresh LB broth and incubated at 37°C with 250-rpm shaking until OD<sub>600</sub> reached 0.3-0.5. The culture was chilled on ice for 10 min and then centrifuged at 4,000 rpm for 10 min at 4°C. The *E. coli* pellet was gently resuspended in 20 ml of cold 0.1 M CaCl<sub>2</sub> and incubated on ice for 10 min. Cells were then centrifuged at 4,000 rpm for 10 min at 4°C and the cell pellet was gently resuspended in 4 ml of cold 0.1 M CaCl<sub>2</sub> containing 30% (v/v) glycerol. The suspension of competent cells was split into 200-μl aliquots and kept at -80°C until required.

### 3.2.6 Transformation of plasmid DNA into competent cells (75)

The *DpnI*-digested PCR product (5-20 μl) was mixed with 200-μl competent cells. The mixture was incubated on ice for 30 min, followed by incubation at 42°C for exactly 90 sec, and then immediately placed on ice for 5 min. 800 μl of LB broth was added into the transformed cells, gently mixed and incubated at 37°C with 250-rpm shaking for 45 min. The transformed cells were collected by centrifugation at 5,000 rpm for 30 sec and the cell pellet was gently resuspended in 200-μl LB broth. The cell suspension was spread on a LB agar plate containing 100 μg/ml ampicillin. The agar plate was incubated at 37°C for 16-20 hrs until *E. coli* colonies were clearly seen on agar plate.

### 3.2.7 Mutant plasmid screening

Restriction endonuclease analysis was used to screen for each mutant plasmid based on a recognition site silently introduced into each pair of mutagenic primers. The digestion reaction (20  $\mu$ l) was composed of 100-200 ng of plasmid DNA, 1x restriction enzyme digestion buffer, 3-5 U of restriction endonuclease and sterile distilled water to make up a total volume of 20  $\mu$ l. The digestion reaction was incubated at recommended temperature for a period of time depending on the specification supplied by the enzyme manufacturer. To visualize the restriction patterns, agarose gel electrophoresis (0.8-1.2% gel) of the digested DNA was carried out in TAE buffer with constant voltage of 80 volts.

### 3.2.8 DNA sequencing

In order to verify nucleotide sequences of the mutant plasmids, 200 ng of each mutant plasmid, together with 10 pmole of oligonucleotide primer (V147A-f: 5'-CGTTTAATGCAATCAGTACGTATCATAATCACC-3'), was submitted to Macrogen Inc. (Korea) to perform DNA sequencing. The resulting sequences were aligned with that of the wild type using ClustalX.

### 3.2.9 Expression of toxins (41)

Each clone of *E. coli* strain JM109 containing either wild-type or each mutant plasmid was inoculated into 3-ml LB broth containing 100  $\mu$ g/ml ampicillin and grown at 37°C with 250-rpm shaking for 16-20 hrs. The *E. coli* culture was transferred into fresh LB broth containing ampicillin at inoculation ratio of 1:100 and incubated until OD<sub>600</sub> reached 0.3-0.5. Then, protein expression was induced with IPTG at a final concentration of 0.1 mM at either 37°C for 4 hrs (for toxicity assays) or 30°C for 10 hrs (for biochemical characterization). The cell cultures were collected by centrifugation at 6,000 rpm for 10 min. 0.1 OD<sub>600</sub> of *E. coli* cells ( $\sim 10^7$  cells) was subjected to analysis of the protein profiles by sodium dodecyl sulfate-polyacrylamide gel (10%) electrophoresis (SDS-PAGE).

### 3.2.10 SDS-polyacrylamide gel electrophoresis (75)

For sample preparation, protein samples were mixed with 4x loading buffer (8% SDS, 40% glycerol, 0.4% bromophenol blue, 100 mM DTT and 200 mM Tris-HCl, pH 6.8) at ratio of 3:1 and heated at 100°C for 10 min. The heated samples were vigorously mixed using vortex and centrifuged at 10,000 rpm for 10 min. The supernatant was then loaded into each well of SDS-polyacrylamide gel.

SDS-polyacrylamide gel was prepared using the Bio-Rad Mini-Protein II system. SDS-polyacrylamide gel is composed of separating and stacking gels. The separating gel consists of 3.3% crosslinker, 10% or 12% gel, 0.375 M Tris-HCl (pH 8.8) and 0.1% SDS. The stacking gel contains 3.3% crosslinker, 5% gel, 0.125 M Tris-HCl (pH 6.8) and 0.1% SDS. The gel was run in Tris-glycine buffer (25 mM Tris, 192 mM glycine and 0.1% SDS). Electrophoresis was performed with constant voltage of 100 volts at room temperature.

After electrophoresis, protein bands on the gel were visualized by soaking the gel in staining solution (10% ethanol, 10% glacial acetic acid and 0.1% Coomassie brilliant blue R-250) for 40 min. The gel was subsequently soaked in destaining solution (10% ethanol and 10% glacial acetic acid) until the background was clear.

### 3.2.11 Isolation of protoxin inclusions

#### 3.2.11.1 Inclusion isolation using distilled water

*E. coli* cells expressing recombinant protein were harvested by centrifugation and resuspended in cold distilled water. The cell suspension was lysed by using a French Pressure Cell at 10,000 psi and the cell lysate was then centrifuged at 6,000 ×g for 10 min at 4°C. The pellet was washed three times in cold distilled water. Protein concentration of the protoxin inclusion was examined by using a Bradford-based protein microassay (see **section 3.2.12**).

#### 3.2.11.2 Inclusion isolation using 100 mM KH<sub>2</sub>PO<sub>4</sub> (pH 5.0)

*E. coli* cells expressing recombinant proteins were harvested by centrifugation and resuspended in cold 100 mM KH<sub>2</sub>PO<sub>4</sub> (pH 5.0). The cell suspension was disrupted by using the French Pressure Cell at 10,000 psi and the crude lysate was then centrifuged at 6,000 ×g for 10 min at 4°C. The pellets were resuspended and incubated in 100 mM KH<sub>2</sub>PO<sub>4</sub> containing 1 M NaCl and 0.1% Triton

X-100 at 4°C. After incubation for 30 min, the pellets were collected by centrifugation and washed once in cold 100 mM KH<sub>2</sub>PO<sub>4</sub> and twice in cold distilled water. Protein concentrations of the partially purified toxin inclusions were determined by using the Bradford-based protein microassay (Bio-Rad).

### **3.2.12 Determination of protein concentrations**

Protein concentrations were determined by using Bio-Rad protein assay reagent based on the method described by Bradford (77). The calibration curve was constructed using bovine serum albumin (BSA) as a protein standard. BSA standards were prepared by making dilution ranging from 0, 1, 2, 3, 4 and 5 µg/50 µl in distilled water. Each standard protein and sample solution was mixed with 200 µl of Bradford dye reagent in a 96-well flat-bottom microtiter plate (Bibby Sterilin, England). The absorbance of samples and standards was measured at 595 nm by using an automatic microplate reader (Spectra MAX 190). The protein concentrations of samples were calculated from the standard curve.

### **3.2.13 Solubilization of toxin inclusion and proteolytic digestion**

Protoxin inclusions were solubilized at a concentration of 1 mg/ml in 50 mM Na<sub>2</sub>CO<sub>3</sub> (pH 9.0) and incubated at 37°C for 1 hr. For solubility analysis, the incubated toxins were subjected to centrifugation at 6,000 ×g for 10 min. The supernatants containing soluble toxins were analyzed by SDS-PAGE (10% gel) in comparison with the non-centrifuged solubilized toxins.

For proteolytic digestion, the soluble protoxins were treated with trypsin (L-1-tosylamido-2-phenylethyl chloromethyl ketone-treated, Sigma) at an enzyme/toxin ratio of 1:20 (w/w). The protoxin-trypsin mixture was incubated at 37°C for 24 hrs and the trypsin-digested products were then analyzed by SDS-PAGE (12% gel).

### **3.2.14 Precipitation of soluble protoxin**

After solubilization of protoxin inclusion in 50 mM Na<sub>2</sub>CO<sub>3</sub> (pH 9.0), the supernatant containing soluble protoxin was dialyzed against 100 mM KH<sub>2</sub>PO<sub>4</sub> (pH 5.0) at volume ratio of 1:200 for 16 hrs, with four-time change of outer solution. The

precipitates occurring after dialysis were recovered by centrifugation at  $6,000 \times g$  for 10 min and subsequently washed twice in distilled water. Protein concentration of the precipitated protoxin inclusion was determined as described in **section 3.2.12**.

### 3.2.15 Mosquito-larvicidal activity assay

Bioassays for mosquito-larvicidal activity were performed using 2-day old *A. aegypti* larvae (hatched from eggs supplied by the mosquito-rearing facility of the Institute of Molecular Biosciences, Mahidol University).  $10 \text{ OD}_{600}$  ( $\sim 10^9$  cells) of *E. coli* cells expressing Cry4Aa wild-type or mutant toxins were harvested by centrifugation at 6,000 rpm for 10 min at  $4^\circ\text{C}$  and resuspended in 2 ml of distilled water ( $10^8$  cells/200  $\mu\text{l}$ ). Each assay was carried out in a 48-well microtiter plate (11.3-mm well diameter, Costar, USA), with 10 larvae per well in 800  $\mu\text{l}$  of distilled water. Then, 200  $\mu\text{l}$  of *E. coli* suspension ( $10^8$  cells) was added into each well. 100 larvae were used for each sample in one experiment and three independent experiments were performed. *E. coli* cells containing the pMEx-8 vector were used as a negative control. To observe toxicity of the precipitated protoxin inclusions, 200  $\mu\text{l}$  of inclusion suspension (50  $\mu\text{g/ml}$ ) was used in place of *E. coli* suspension. Mortality was recorded after 24-hr incubation period.

### 3.2.16 Purification of Cry4Aa toxin and its mutants

The 65-kDa trypsin-activated Cry4Aa toxin and its mutants were first centrifuged at 10,000 rpm for 10 min and supernatant was then injected into a size-exclusion FPLC system, equipped with a Superose 12 GL 10/300 column (GE Healthcare Life Sciences). The column was equilibrated with eluent (50 mM  $\text{Na}_2\text{CO}_3$ , pH 9.0) at flow rate of 0.4 ml/min before operation. The injected volume was 200  $\mu\text{l}$  and the operating flow rate of the eluent was 0.4 ml/min. Protein fractions were monitored as UV absorption at 280 nm. Fractions were collected and analyzed by SDS-PAGE (12% gel). The fractions containing a purified 65-kDa activated toxin were pooled together and concentrated using a 30-kDa cutoff centrifugal filter tube (PALL). Protein concentration was determined as described in **section 3.2.12**.

### 3.2.17 Intrinsic fluorescence measurement

Structural change of mutant toxins was examined *via* their intrinsic tryptophan fluorescence. The fluorescence spectra were obtained by emission scanning of the FPLC-purified trypsin-activated toxins using Jasco FP-6300 spectrofluorometer. The emission wavelengths were observed from 300 to 500 nm with the excitation wavelength of 280 nm. Excitation and emission slit widths are 5.0 and 2.5 nm, respectively. All spectra were subtracted with the background spectrum.

### 3.2.18 Identification of disulfide bond-containing peptides

Band-shift assay was employed to identify disulfide bond-containing protein fragments. Prior to analysis on SDS-(12%) polyacrylamide gel, the trypsin-treated toxin fragments of the Cry4Aa wild type and its mutants were prepared by incubation with sample loading buffer (2% SDS, 10% glycerol, 0.1% bromophenol blue, 50 mM Tris-HCl (pH 6.8), with/without 25 mM DTT).

### 3.2.19 Membrane perturbation assays (78-79)

#### 3.2.19.1 Preparation of calcein-entrapped hybrid liposomes

Larval gut suspension was prepared from 4-day old *A. aegypti* larvae. 60 dissected guts were suspended in 100  $\mu$ l of 50 mM Na<sub>2</sub>CO<sub>3</sub> buffer (pH 9.0), containing 5 mM EDTA and 1 mM PMSF, by using the micropipette. Protein concentrations of larval gut suspension were quantified as described in **section 3.2.12**. A lipid mixture (10 mg/ml) was prepared from phosphatidylethanolamine (PE), phosphatidylcholine (PC) and cholesterol (Ch) at the ratio of 10:10:1 (w/w). 2 mg of the lipid mixture, 1.5 ml of chloroform and 250  $\mu$ g of larval gut suspension were placed in an amber glass bottle and then mixed by sonication. The mixture was dried under a gentle stream of oxygen-free nitrogen gas at room temperature. The resulting lipid film was resuspended in 200  $\mu$ l of 50 mM calcein (pre-dissolved in 150 mM Na<sub>2</sub>CO<sub>3</sub> buffer, pH 9.0) and then briefly sonicated. Large unilamella vesicles (LUVs) were prepared by repeatedly squeezing the lipid suspension through a polycarbonate membrane (0.1- $\mu$ m pore size, Avanti Polar Lipids) for a minimum of 15 passes, using a two-syringe extruder (Avanti Polar Lipids). Unentrapped calcein was removed from the LUV suspension by gel filtration on PD-10 desalting column (GE Healthcare Life

Sciences) equilibrated with 150 mM Na<sub>2</sub>CO<sub>3</sub> buffer (pH 9.0). Liposome concentrations were estimated by measuring the lipid phosphorus content (see section 3.2.19.2). The calcein-entrapped liposomes were diluted to a phospholipid concentration of 1 μM with 50 mM Na<sub>2</sub>CO<sub>3</sub> buffer (pH 9.0) for performing the membrane perturbation assays.

#### 3.2.19.2 Phosphorus content analysis of phospholipid (80)

Phosphorus standards were prepared with various volumes (0, 10, 20, 30 and 40 μl) of 1 mM Na<sub>2</sub>HPO<sub>4</sub>. Each standard solution was transferred to a clean glass tube and solvent was completely dried on heated sand tray. 50 μl of 70% perchloric acid was then added into the tube and allowed to heat at 180°C for 1 hr. After the mixtures were cooled down, 0.9 ml of phosphorus assay solution was added and incubated at 80°C for 10 min before measuring absorbance at 820 nm. A standard curve was then plotted against phosphorus quantity versus absorbance<sub>820</sub>. For phospholipid samples, 20 μl of liposome suspension was used and the phospholipid concentrations were calculated from the standard curve.

#### 3.2.19.3 Calcein release assays

Membrane perturbation was assessed by calcein release assays as previously described (78-79). The calcein dye would be self-quenched when it was trapped inside liposomes. Thus, membrane perturbation can be detected by measuring an increase in fluorescence of the released calcein. Leakage of calcein was followed using a Jasco FP-6300 spectrofluorometer, with excitation and emission wavelengths set at 485 and 520 nm, respectively, and a slit width of 5 nm. When fluorescence intensity of 400 μl of calcein-entrapped liposome was stable, the purified toxin (0.6-30.0 μg) was added and fluorescence of the leaked calcein was monitored for 10 min. Finally, 10 μl of 0.5% Triton X-100 was added to determine the total fluorescence intensity of the sample. Percentage of calcein release (%*F*) was defined as:

$$\%F = \frac{I_t - I_0}{I_{max} - I_0} \times 100$$

where *I*<sub>0</sub> = the initial fluorescence intensity

*I*<sub>*t*</sub> = the fluorescence intensity observed after addition of purified toxin

*I*<sub>*max*</sub> = the total fluorescence intensity observed after addition of Triton X-100

### 3.2.20 Molecular dynamics (MD) simulations

The structural model of the Cry4Aa monomer in 150 mM KCl solution box (66) was used as an initial system for 10-ns simulations. MD simulations were performed using NAMD 2.6 program (81) and CHARMM27 force field (82). The system was energy minimized and then equilibrated for 50 ps at temperature of 298 K and pressure of 1 atm with all heavy atoms of the protein under harmonic constraints (a force constant of 2 kcal/mole/Å<sup>2</sup>). Subsequently, without constraints, equilibration was continued for another 10 ns.

The simulations were performed under periodic boundary conditions. Temperature and pressure were controlled using Langevin temperature control (a damping constant of 5 p/s) and Langevin piston control (an oscillation period of 200 fs and a damping time of 100 fs), respectively. A time step of 1 fs was used and electrostatic interactions were calculated every four time steps using the Particle Mesh Ewald method (83-84). van der Waals interactions were computed every step using a 13-Å cutoff and a switching function.

The equilibrated coordinates of the 10-ns Cry4Aa system were used as a template for amino acid substitutions using VMD program. The resulting mutant systems were equilibrated for 10 ns under the same condition as that used for the wild-type system.

Root mean square fluctuation (RMSF) values were calculated from the last 4 ns of the wild-type MD trajectories. The RMSF was defined as:

$$\text{RMSF} = \sqrt{\frac{1}{T} \sum_{t=1}^T (x_i(t) - \tilde{x}_i)^2}$$

where  $x_i(t)$  = the coordinates of C<sub>α</sub> atom of residue  $x_i$  at time-step  $t$

$\tilde{x}_i$  = the average coordinates of C<sub>α</sub> atom of residue  $x_i$

$T$  = the number of time-steps

## CHAPTER IV

### RESULT I: ISOLATION OF Cry4Aa INCLUSION

#### 4.1 Isolation of Cry4Aa protoxin inclusion from *E. coli* cells

Upon IPTG induction, *E. coli* cells harboring pMEx-B4A plasmid produced 130-kDa Cry4Aa protein as cytoplasmic inclusions (**Figure 4.1B**). When *E. coli* cells expressing the Cry4Aa toxin were pelleted, resuspended in distilled water and subsequently lysed as described in section 3.2.11.1, the expressed 130-kDa Cry4Aa protoxin, however, was totally found in the soluble fraction of the cell lysate (**Figure 4.2A**). Interestingly, when 100 mM  $\text{KH}_2\text{PO}_4$  (pH 5.0) was used instead as a cell-suspending buffer (see section 3.2.11.2), the expressed Cry4Aa protoxin was entirely found as sedimentable inclusion in the insoluble fraction (**Figure 4.2B**). Henceforth, protoxin inclusions of Cry4Aa and its mutants were isolated from *E. coli* cells by following the method described in section 3.2.11.2.

Assessment of alkaline solubility of the Cry4Aa inclusion isolated from *E. coli* cells revealed that the toxin inclusion was highly soluble in 50 mM  $\text{Na}_2\text{CO}_3$  buffer (pH 9.0) (**Figure 4.3A**). When the 130-kDa soluble protoxin was subsequently treated with trypsin, it was cleaved into two fragments of ca. 47 and ca. 21 kDa (**Figure 4.3B**).

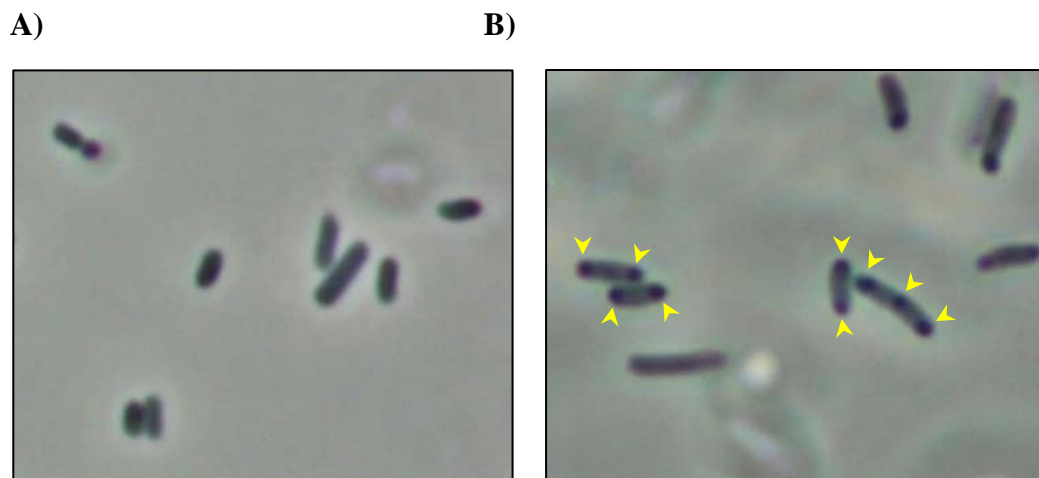


**Figure 4.1 Phase-contrast micrographs of *E. coli* cells harboring pMEx-8 or pMEx-B4A**

The figure shows IPTG-induced *E. coli* cells, harboring pMEx-8 (A) or pMEx-B4A (B), visualized under a phase-contrast microscope. Cry4Aa protein was produced as cytoplasmic inclusions (indicated by arrows) in *E. coli* cells containing pMEx-B4A recombinant plasmid.

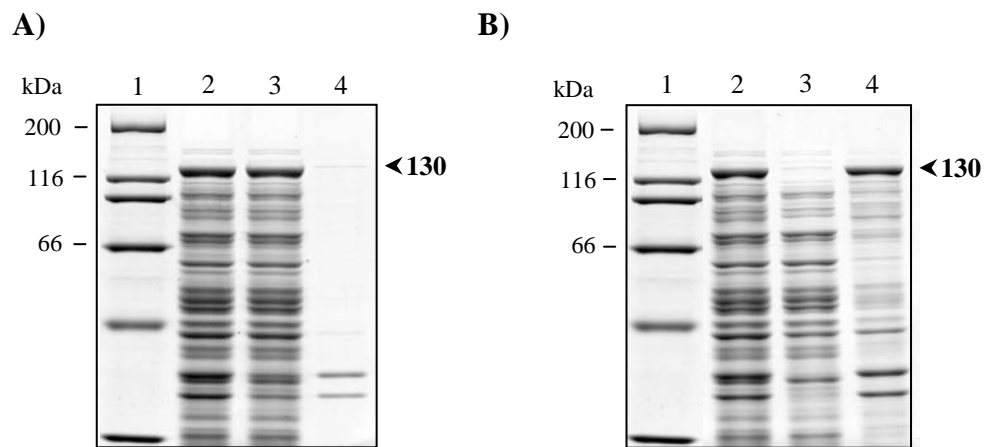


**Figure 4.2 Protein profiles of extracted protein fractions from *E. coli* cells suspended in distilled water or 100 mM  $\text{KH}_2\text{PO}_4$**

**A)** Coomassie blue-stained SDS-polyacrylamide gel (10%) shows protein profiles of lysate extracted from *E. coli* cells suspended in distilled water. The bands of 130-kDa protoxins are indicated.

Lane 1: Molecular mass standards

Lane 2: Total cell lysate

Lane 3: Supernatant fraction

Lane 4: Sedimented inclusion

**B)** Coomassie blue-stained SDS-polyacrylamide gel (10%) shows protein profiles of lysate extracted from *E. coli* cells suspended in 100 mM  $\text{KH}_2\text{PO}_4$  buffer. The bands of 130-kDa protoxins are indicated.

Lane 1: Molecular mass standards

Lane 2: Total cell lysate

Lane 3: Supernatant fraction

Lane 4: Sedimented inclusion

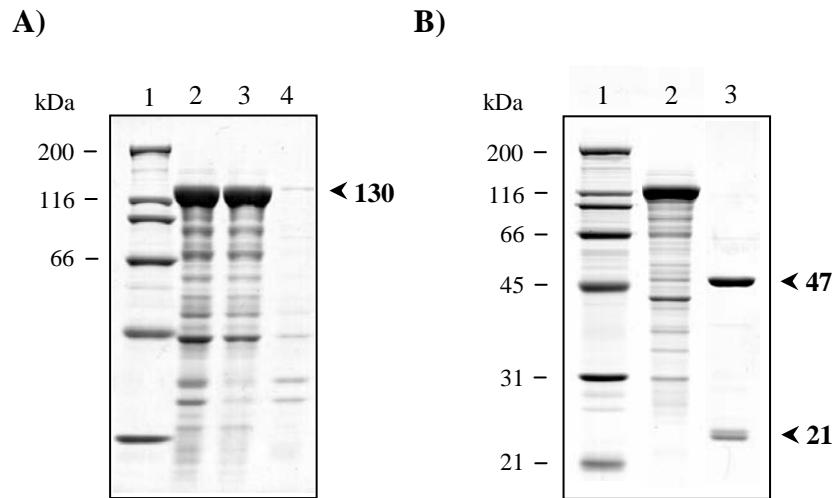


**Figure 4.3 Alkaline solubility and proteolytic stability of Cry4Aa inclusion**

**A)** Coomassie blue-stained SDS-polyacrylamide gel (10%) shows solubility of Cry4Aa inclusion in 50 mM Na<sub>2</sub>CO<sub>3</sub> buffer (pH 9.0). The bands of 130-kDa protoxins are indicated.

- Lane 1: Molecular mass standards
- Lane 2: Total inclusion suspension
- Lane 3: Soluble fraction
- Lane 4: Insoluble pellet

**B)** Coomassie blue-stained SDS-polyacrylamide gel (12%) shows tryptic processing of Cry4Aa protoxin. The bands of trypsin-treated toxin products (ca. 47- and ca. 21-kDa) are indicated.

- Lane 1: Molecular mass standards
- Lane 2: Trypsin-untreated Cry4Aa protoxin
- Lane 3: Trypsin-treated products of Cry4Aa protoxin

## 4.2 Precipitation of Cry4Aa inclusion from its soluble protoxin

When soluble Cry4Aa protoxin in 50 mM Na<sub>2</sub>CO<sub>3</sub> buffer (pH 9.0) was dialyzed against 100 mM KH<sub>2</sub>PO<sub>4</sub> buffer (pH 5.0), it became precipitated as a white sedimentable inclusion. The resulting precipitated Cry4Aa inclusion can be resolubilized in 50 mM Na<sub>2</sub>CO<sub>3</sub> buffer (pH 9.0) (**Figure 4.4A**) and was tryptically processed to two protease-resistant fragments of ca. 47 and ca. 21 kDa (**Figure 4.4B**).

Moreover, when 10 µg of the precipitated Cry4Aa inclusion was tested for its larvicidal activity, it showed toxicity against *A. aegypti* larvae as good as *E. coli* cells (10<sup>8</sup>) expressing approximately 10 µg of the 130-kDa Cry4Aa toxin (**Figure 4.5**).

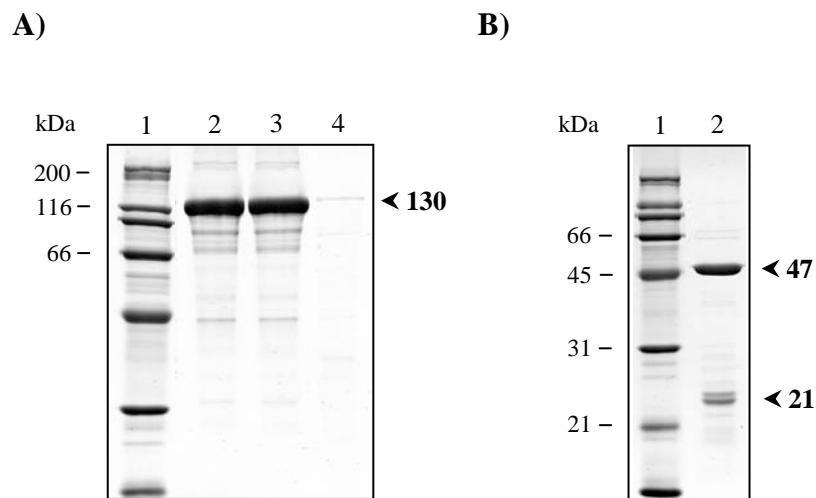


**Figure 4.4 Alkaline solubility and proteolytic stability of precipitated Cry4Aa inclusion**

**A)** Coomassie blue-stained SDS-polyacrylamide gel (10%) shows solubility of precipitated Cry4Aa inclusion in 50 mM Na<sub>2</sub>CO<sub>3</sub> buffer (pH 9.0). The bands of 130-kDa protoxins are indicated.

- Lane 1: Molecular mass standards
- Lane 2: Total inclusion suspension
- Lane 3: Soluble fraction
- Lane 4: Insoluble pellet

**B)** Coomassie blue-stained SDS-polyacrylamide gel (12%) shows tryptic processing of precipitated Cry4Aa protoxin. The bands of trypsin-treated toxin products (ca. 47- and ca. 21-kDa) are indicated.

- Lane 1: Molecular mass standards
- Lane 2: Trypsin-treated products of precipitated Cry4Aa protoxin

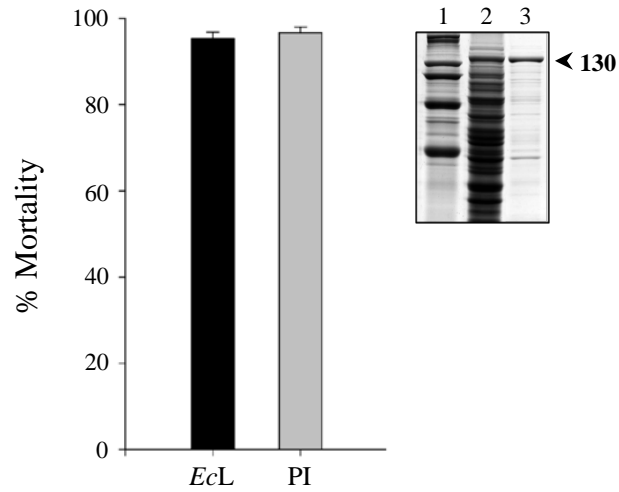


**Figure 4.5 Larvicidal activity of *E. coli* cells expressing Cry4Aa toxin and of precipitated Cry4Aa inclusion**

The figure shows larvicidal activity of *E. coli* ( $10^8$  cells) expressing the Cry4Aa toxin (*EcL*) and of 10- $\mu$ g precipitated Cry4Aa toxin inclusion (PI). Error bars represent standard errors of the mean (SEM) from three independent experiments.

Inset is SDS-PAGE analysis of :

- Lane 1: Molecular mass standards (quantity of each protein band is 1  $\mu$ g)
- Lane 2: Lysates extracted from *E. coli* ( $10^7$  cells) expressing Cry4Aa toxin
- Lane 3: Inclusion suspension of precipitated Cry4Aa toxin (1  $\mu$ g)

## CHAPTER V

### RESULT II: MUTAGENESIS OF PROLINE RESIDUES WITHIN $\alpha$ 4- $\alpha$ 5 LOOP OF Cry4Aa TOXIN

It was previously demonstrated that proline-rich sequence (Pro<sup>193</sup>Pro<sup>194</sup>\_Pro<sup>196</sup>), found within the loop connecting helices 4 and 5 of Cry4Aa-domain I, is crucial for mosquito-larvicidal activity of the toxin (16). In this study, site-directed mutagenesis was employed to further examine structural importance of the proline-rich sequence.

#### 5.1 Constructions of valine-substituted Cry4Aa mutant plasmids

To examine whether hydrophobic feature *per se* of the proline-rich sequence is important for larvicidal activity of the Cry4Aa toxin, three valine-substituted mutant plasmids (pP193V, pP194V and pP196V) were generated by PCR-based directed mutagenesis. The pMEx-B4A plasmid (**Figure 3.2**) containing the gene sequence of the 130-kDa Cry4Aa protein was used as a template. Oligonucleotides containing mutated nucleotide residues and an introduced restriction enzyme recognition site for screening the mutant plasmids were used as mutagenic primers. After PCR amplification, the PCR products were digested with *DpnI* endonuclease and analyzed on agarose gel as shown in **Figure 5.1**. It was found that all PCR products showed a 7.4-kb major DNA band which corresponds to pMEx-B4A.

The *DpnI*-treated PCR products were then transformed into *E. coli* JM109 competent cells. The mutant plasmids from *E. coli* transformants with the required mutation were first screened by restriction endonuclease digestion. After being treated with an appropriate restriction endonuclease, the digested DNA fragments of the mutant plasmids could be distinguished from those of the wild-type plasmid as shown in **Figures 5.2A-5.4A**. Each mutant plasmid was further verified in the mutated region by DNA sequencing as shown in the sequencing chromatograms (**Figures 5.2B-5.4B**).

The results showed that all mutant plasmids contained nucleotide changes at the desired positions.

## 5.2 Expression of valine-substituted Cry4Aa mutant toxins

The plasmids encoding the 130-kDa Cry4Aa wild-type or mutant toxins were expressed in *E. coli* JM109 under inducible control of the *tac* promoter together with the *cry4Ba* promoter upon IPTG induction as described in **section 3.2.9**. Protein profiles of lysates extracted from the *E. coli* cells revealed that protein expression levels of all valine-substituted mutants (P193V, P194V and P196V) were comparable with that of the wild type (**Figure 5.5**).

## 5.3 Solubilization and proteolytic processing of valine-substituted Cry4Aa mutant toxins

The alkaline solubility of Cry4Aa mutant toxin inclusions in comparison with that of the wild-type inclusion was carried out as previously described in **section 3.2.13**. To determine the percentage of toxin solubility, amounts of the 130-kDa soluble toxins in the supernatant were compared with those of the total toxin inclusions initially used. A nearly complete loss of solubility was observed for the P193V mutant while solubility of the remaining mutants (P194V and P196V) was comparable with that of the wild type (**Figure 5.6**).

The soluble mutant protoxins were subsequently examined for their proteolytic stability by digestion with TPCK-treated trypsin and all were found to yield trypsin-resistant products of ca. 47 and ca. 21 kDa similar to the Cry4Aa wild-type protoxin (**Figure 5.7**).

#### **5.4 Mosquito-larvicidal activity of valine-substituted Cry4Aa mutant toxins**

To determine an effect of valine substitutions on toxicity, *E. coli* cells expressing each Cry4Aa mutant toxin were tested for their biological activity against *A. aegypti* larvae. As can be seen in **Figure 5.8**, P193V substitution reduced larvicidal activity of approximately 75% and two other valine-substituted mutations, P194V and P196V, resulted in a 25% loss in toxicity.

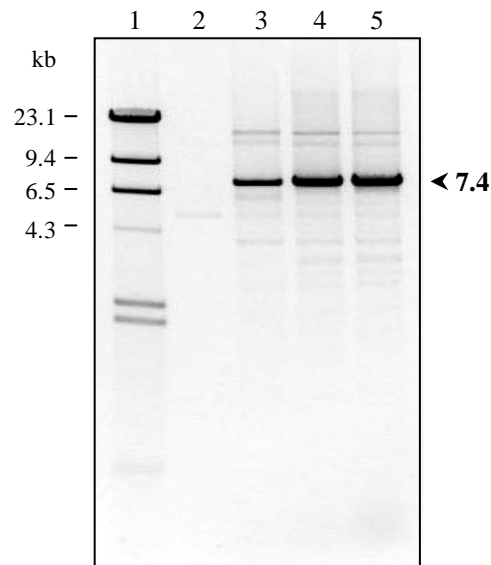


**Figure 5.1 PCR amplification of Cry4Aa mutant plasmids: pP193V, pP194V and pP196V**

The figure shows 0.8% agarose gel electrophoresis (ethidium bromide-stained) of *DpnI*-treated PCR products of Cry4Aa mutant plasmids. The expected 7.4-kb DNA band in each lane is indicated with the bold label.

Lane 1:  $\lambda$ /*Hind*III DNA markers

Lane 2: The pMEx-B4A plasmid

Lane 3: The *DpnI*-treated PCR products of the pP193V plasmid

Lane 4: The *DpnI*-treated PCR products of the pP194V plasmid

Lane 5: The *DpnI*-treated PCR products of the pP196V plasmid

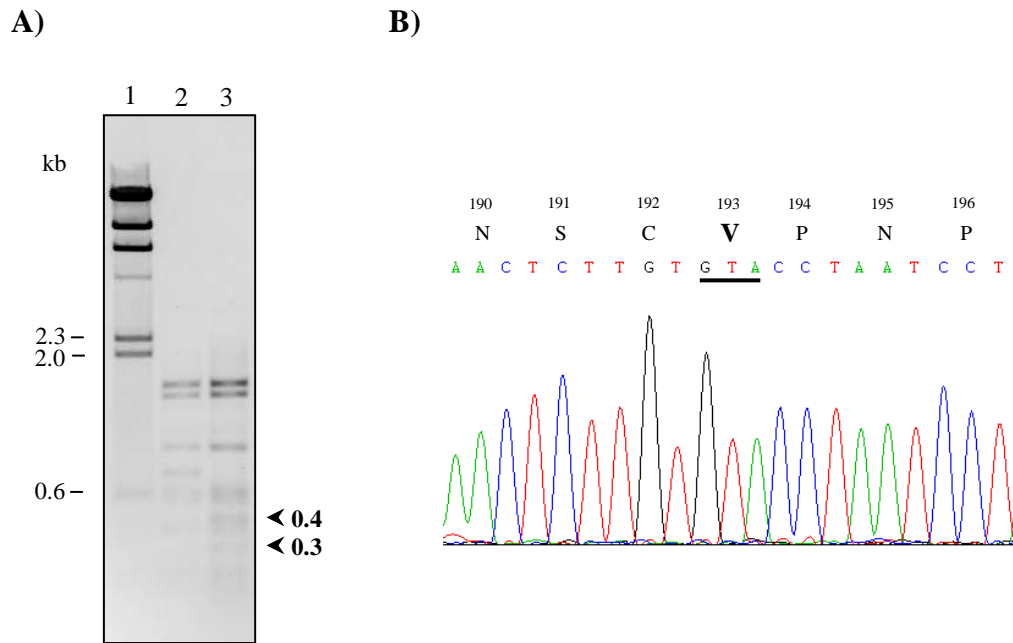


**Figure 5.2 Restriction digestion and DNA sequencing of pP193V**

**A)** 1.0% agarose gel electrophoresis (ethidium bromide-stained) of *RsaI* digestion patterns of the wild-type and mutant plasmids. The 0.4- and 0.3-kb mutant-specific DNA bands are indicated.

Lane 1:  $\lambda$ /*HindIII* DNA markers

Lane 2: The *RsaI*-digested wild-type plasmid, pMEx-B4A

Lane 3: The *RsaI*-digested mutant plasmid, pP193V

**B)** DNA sequencing chromatogram of pP193V, using V147A-f as a sequencing primer. Part of the sense strand sequence is shown. Underlined letters indicate the mutated nucleotides. The bold letter represents the substituted amino acid residue.

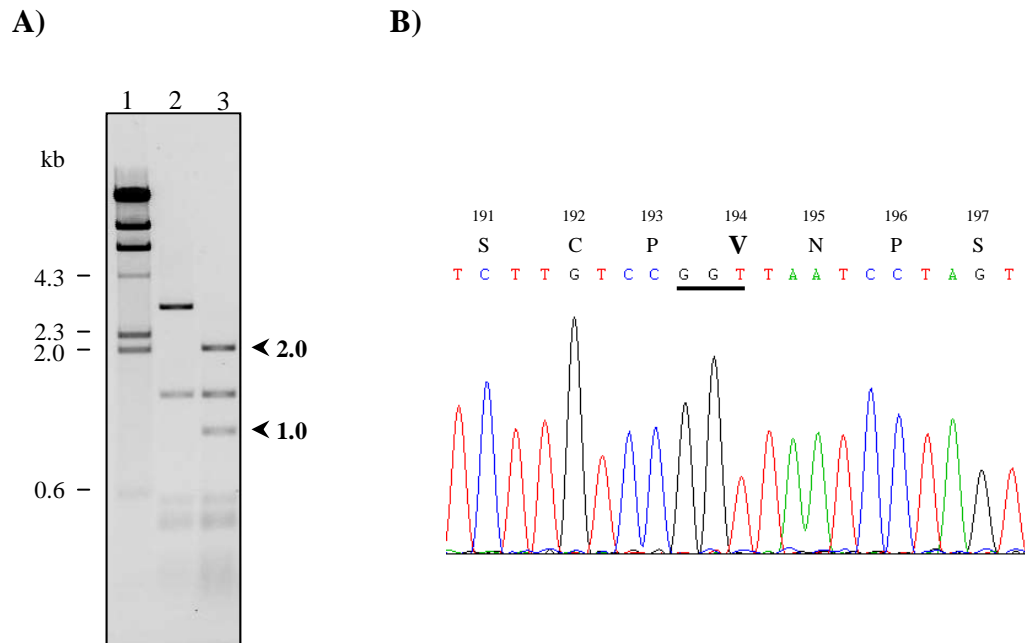


**Figure 5.3 Restriction digestion and DNA sequencing of pP194V**

**A)** 1.0% agarose gel electrophoresis (ethidium bromide-stained) of *Hpa*II digestion patterns of the wild-type and mutant plasmids. The 2.0- and 1.0-kb mutant-specific DNA bands are indicated.

Lane 1:  $\lambda$ /*Hind*III DNA markers

Lane 2: The *Hpa*II-digested wild-type plasmid, pMEx-B4A

Lane 3: The *Hpa*II-digested mutant plasmid, pP194V

**B)** DNA sequencing chromatogram of pP194V, using V147A-f as a sequencing primer. Part of the sense strand sequence is shown. Underlined letters indicate the mutated nucleotides. The bold letter represents the substituted amino acid residue.

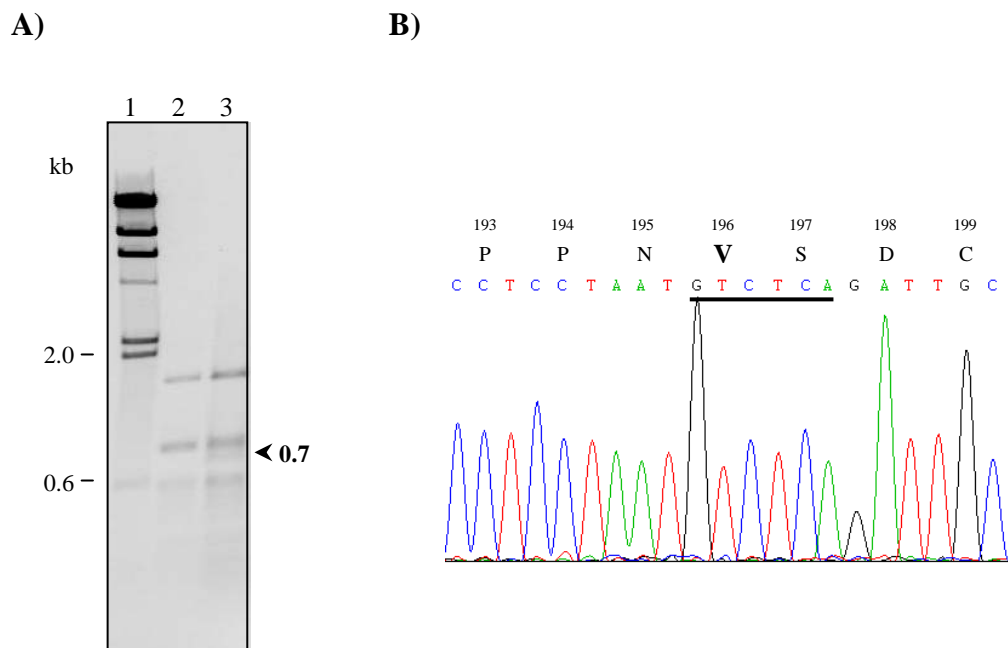


**Figure 5.4 Restriction digestion and DNA sequencing of pP196V**

**A)** 1.0% agarose gel electrophoresis (ethidium bromide-stained) of *DdeI* digestion patterns of the wild-type and mutant plasmids. The 0.7-kb mutant-specific DNA band is indicated.

Lane 1:  $\lambda$ /*HindIII* DNA markers

Lane 2: The *DdeI*-digested wild-type plasmid, pMEx-B4A

Lane 3: The *DdeI*-digested mutant plasmid, pP196V

**B)** DNA sequencing chromatogram of pP196V, using V147A-f as a sequencing primer. Part of the sense strand sequence is shown. Underlined letters indicate the mutated nucleotides. The bold letter represents the substituted amino acid residue.

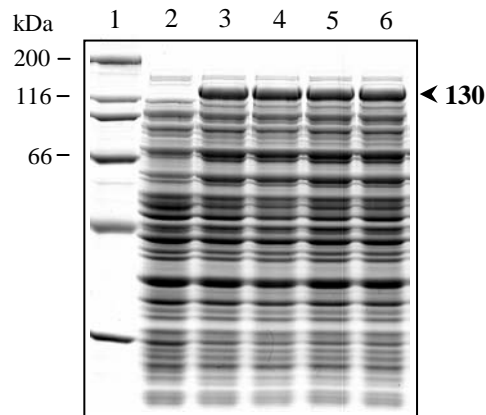


**Figure 5.5 Expression of Cry4Aa and its valine-substituted mutants**

Coomassie blue-stained SDS-polyacrylamide gel (10%) shows protein profiles of lysates extracted from IPTG-induced *E. coli* cells containing each different plasmid. The expected bands of 130-kDa protoxins are indicated.

Lane 1: Molecular mass standards

Lane 2: Lysates extracted from *E. coli* cells containing the pMEx-8 plasmid

Lane 3: Lysates extracted from *E. coli* cells containing the pMEx-B4A plasmid

Lane 4: Lysates extracted from *E. coli* cells containing the pP193V plasmid

Lane 5: Lysates extracted from *E. coli* cells containing the pP194V plasmid

Lane 6: Lysates extracted from *E. coli* cells containing the pP196V plasmid

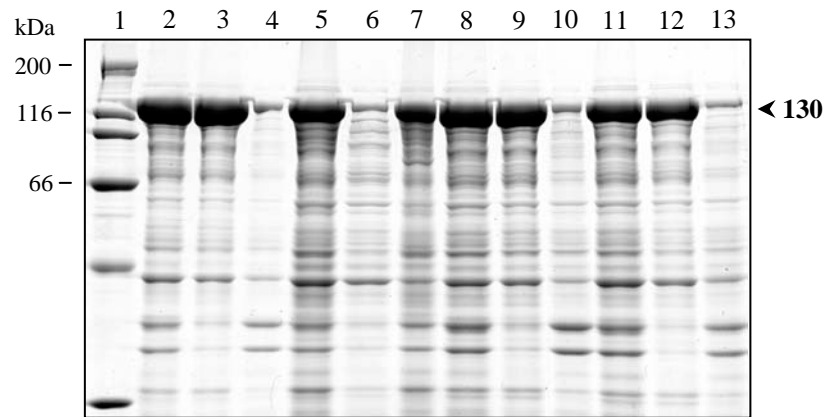


**Figure 5.6 Alkaline solubility of Cry4Aa and its valine-substituted mutant inclusions**

Coomassie blue-stained SDS-polyacrylamide gel (10%) shows solubility of Cry4Aa and its valine-substituted mutant inclusions in 50 mM  $\text{Na}_2\text{CO}_3$  buffer (pH 9.0). The bands of 130-kDa protoxins are indicated.

- Lane 1 : Molecular mass standards
- Lanes 2-4 : Total inclusion suspension, soluble fraction and insoluble pellet of Cry4Aa, respectively
- Lanes 5-7 : Total inclusion suspension, soluble fraction and insoluble pellet of P193V, respectively
- Lanes 8-10 : Total inclusion suspension, soluble fraction and insoluble pellet of P194V, respectively
- Lanes 11-13 : Total inclusion suspension, soluble fraction and insoluble pellet of P196V, respectively

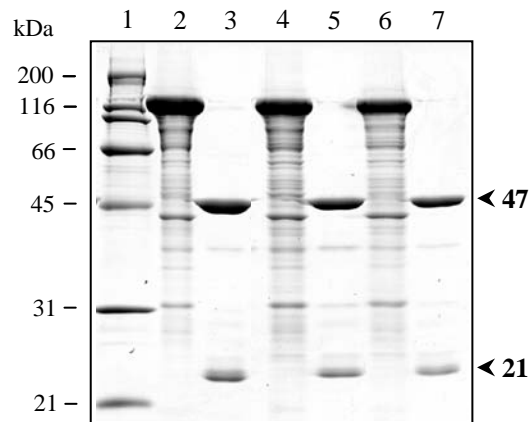


**Figure 5.7 Trypsin-digested products of Cry4Aa and its valine-substituted mutants**

Coomassie blue-stained SDS-polyacrylamide gel (12%) shows tryptic processing of Cry4Aa and its valine-substituted mutants. The expected bands of trypsin-treated products (ca. 47- and ca. 21-kDa) are indicated.

- Lane 1: Molecular mass standards
- Lane 2: Trypsin-untreated Cry4Aa protoxin
- Lane 3: Trypsin-treated products of Cry4Aa
- Lane 4: Trypsin-untreated P194V mutant protoxin
- Lane 5: Trypsin-treated products of P194V
- Lane 6: Trypsin-untreated P196V mutant protoxin
- Lane 7: Trypsin-treated products of P196V

Toxin	% Mortality				
	pMEx-8	Cry4Aa	P193V	P194V	P196V
Mean	0.6	80.6	19.3	58.3	59.0
SEM	0.3	6.9	6.8	4.9	5.5

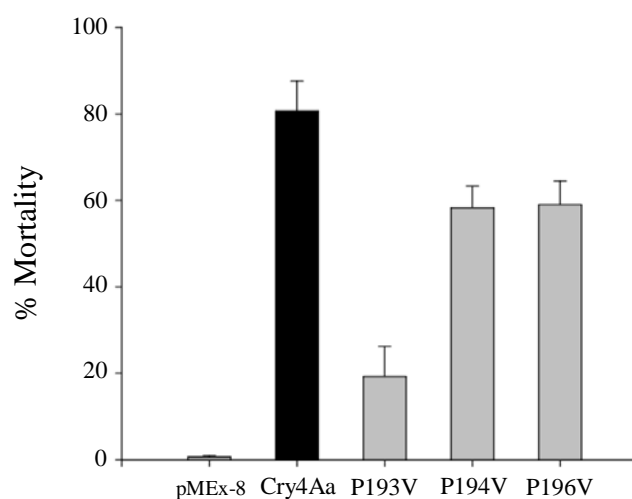


**Figure 5.8 Larvicidal activity of Cry4Aa and its valine-substituted mutants**

The figure shows toxicity of *E. coli* cells ( $10^8$ ) expressing the Cry4Aa wild-type or its mutant toxins (P193V, P194V and P196V) against *A. aegypti* larvae. The control sample was *E. coli* cells carrying pMEx-8 vector. Error bars represent SEM from three independent experiments. Inserted table shows each value in details.

## 5.5 Constructions of glycine-substituted Cry4Aa mutant plasmids

The previous results indicated that hydrophobicity *per se* is not enough for biological function of the critical proline-rich sequence (Pro<sup>193</sup>Pro<sup>194</sup>\_Pro<sup>196</sup>). Apart from hydrophobic feature, proline residues possess the unique cyclic side chain which is known to lock the backbone dihedral angle, thus causing the peptide backbone to be highly rigid. To examine whether the  $\alpha$ 4- $\alpha$ 5 loop rigidity provided by the three proline residues is important for the Cry4Aa toxicity, three glycine-substituted mutants (P193G, P194G and P196G) were therefore generated by PCR-based site-directed mutagenesis.

The amplified products were digested with *DpnI* endonuclease and analyzed on agarose gel. As demonstrated in **Figure 5.9**, all the PCR products showed a 7.4-kb major DNA band which corresponds to pMEx-B4A. The mutant plasmids from *E. coli* transformants were identified by restriction endonuclease digestion (**Figures 5.10A-5.12A**). The mutated region in each mutant plasmid was further confirmed by DNA sequencing (**Figures 5.10B-5.12B**) which revealed that all mutant plasmids contained nucleotide changes at the desired positions.

## 5.6 Expression of glycine-substituted Cry4Aa mutant toxins

The Cry4Aa wild-type and its glycine-substituted mutant toxins were expressed in *E. coli* cells upon IPTG induction. Comparison of expression levels between the wild-type and mutant toxins revealed that expression levels of all glycine-substituted mutants are similar to that of the wild type (**Figure 5.13**).

## 5.7 Solubilization and proteolytic processing of glycine-substituted Cry4Aa mutant toxins

When protoxin inclusions of the Cry4Aa wild type and its glycine-substituted mutants were assessed for their solubility in carbonate buffer (pH 9.0), it was found that inclusion solubility of P194G and P196G mutants was comparable with

that of the wild type whereas ~50% reduction in solubility was observed for the P193G mutant (**Figure 5.14**).

Proteolytic processing of the glycine-substituted mutants in comparison with that of the Cry4Aa wild type revealed that all mutant protoxins were typically cleaved into ca. 47- and ca. 21-kDa fragments (**Figure 5.15**).

## **5.8 Mosquito-larvicidal activity of glycine-substituted Cry4Aa mutant toxins**

Mosquito-larvicidal activity assays were performed to determine an effect of the glycine substitutions on toxicity. When *E. coli* cells expressing each glycine-substituted mutant were tested for their relative toxicity towards *A. aegypti* larvae, it was found that P194G and P196G mutants displayed an approximately 25% decrease in larvicidal activity and P193G mutant exhibited a 50% reduction in toxicity (**Figure 5.16**).

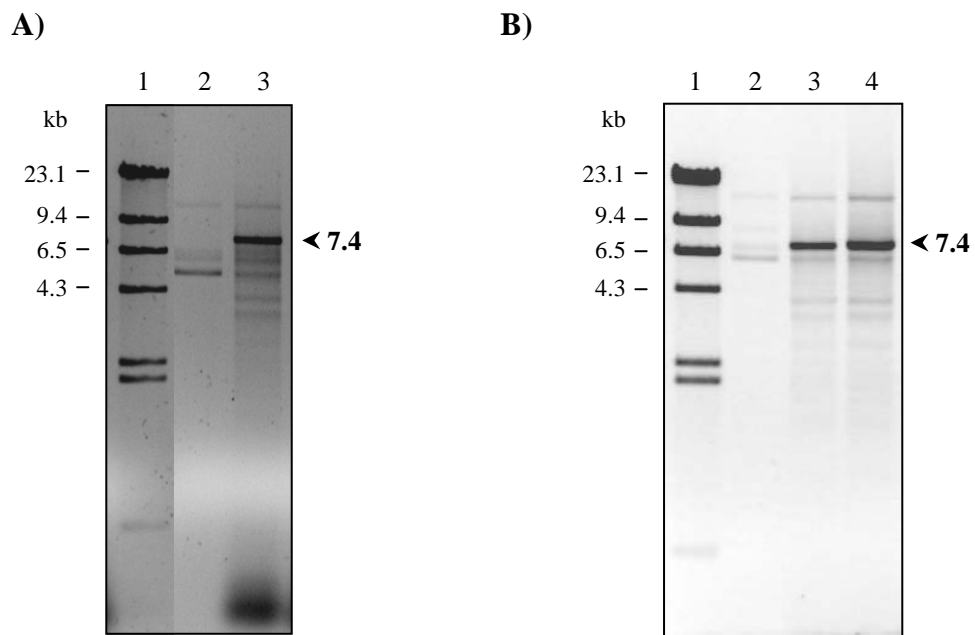


**Figure 5.9 PCR amplification of Cry4Aa mutant plasmids: pP193G, pP194G and pP196G**

The figure shows 0.8% agarose gel electrophoresis (ethidium bromide-stained) of *DpnI*-treated PCR products of Cry4Aa mutant plasmids. The expected 7.4-kb DNA band in each lane is indicated with the bold label.

**A)** Lane 1:  $\lambda$ *HindIII* DNA markers

Lane 2: The pMEx-B4A plasmid

Lane 3: The *DpnI*-treated PCR products of the pP193G plasmid

**B)** Lane 1:  $\lambda$ *HindIII* DNA markers

Lane 2: The pMEx-B4A plasmid

Lane 3: The *DpnI*-treated PCR products of the pP194G plasmid

Lane 4: The *DpnI*-treated PCR products of the pP196G plasmid

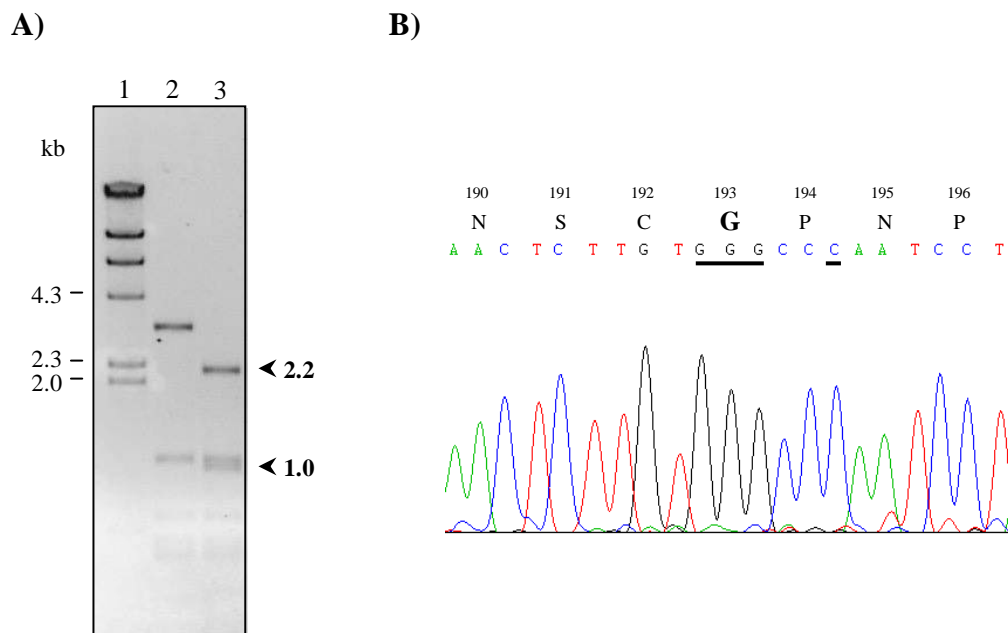


**Figure 5.10 Restriction digestion and DNA sequencing of pP193G**

**A)** 1.2% agarose gel electrophoresis (ethidium bromide-stained) of *Hae*III digestion patterns of the wild-type and mutant plasmids. The 2.2- and 1.0-kb mutant-specific DNA bands are indicated.

Lane 1:  $\lambda$ /*Hind*III DNA markers

Lane 2: The *Hae*III-digested wild-type plasmid, pMEX-B4A

Lane 3: The *Hae*III-digested mutant plasmid, pP193G

**B)** DNA sequencing chromatogram of pP193G, using V147A-f as a sequencing primer. Part of the sense strand sequence is shown. Underlined letters indicate the mutated nucleotides. The bold letter represents the substituted amino acid residue.

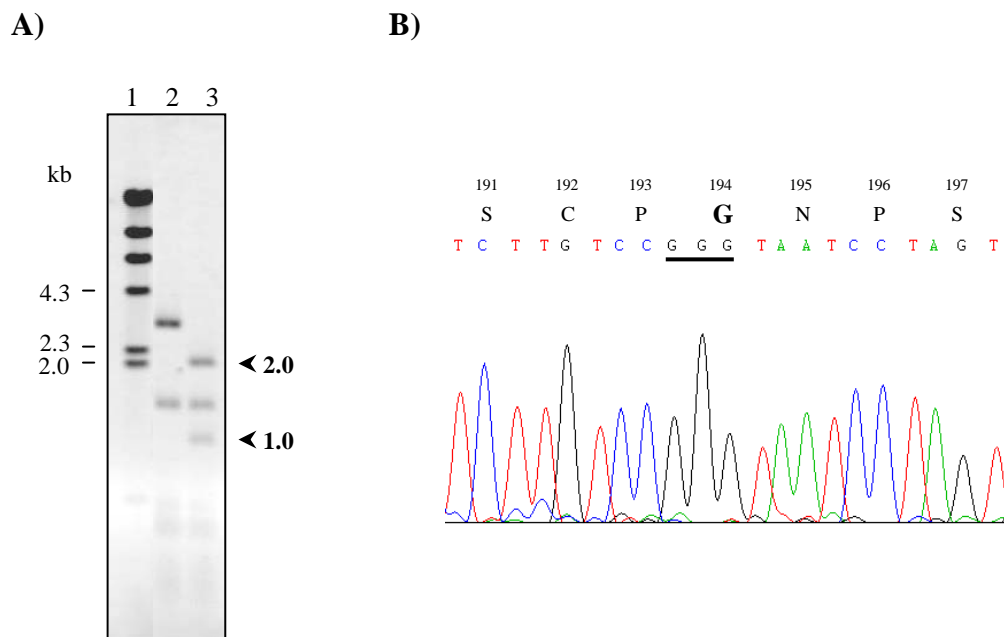


**Figure 5.11 Restriction digestion and DNA sequencing of pP194G**

**A)** 1.2% agarose gel electrophoresis (ethidium bromide-stained) of *Hpa*II digestion patterns of the wild-type and mutant plasmids. The 2.0- and 1.0-kb mutant-specific DNA bands are indicated.

Lane 1:  $\lambda$ /*Hind*III DNA markers

Lane 2: The *Hpa*II-digested wild-type plasmid, pMEx-B4A

Lane 3: The *Hpa*II-digested mutant plasmid, pP194G

**B)** DNA sequencing chromatogram of pP194G, using V147A-f as a sequencing primer. Part of the sense strand sequence is shown. Underlined letters indicate the mutated nucleotides. The bold letter represents the substituted amino acid residue.

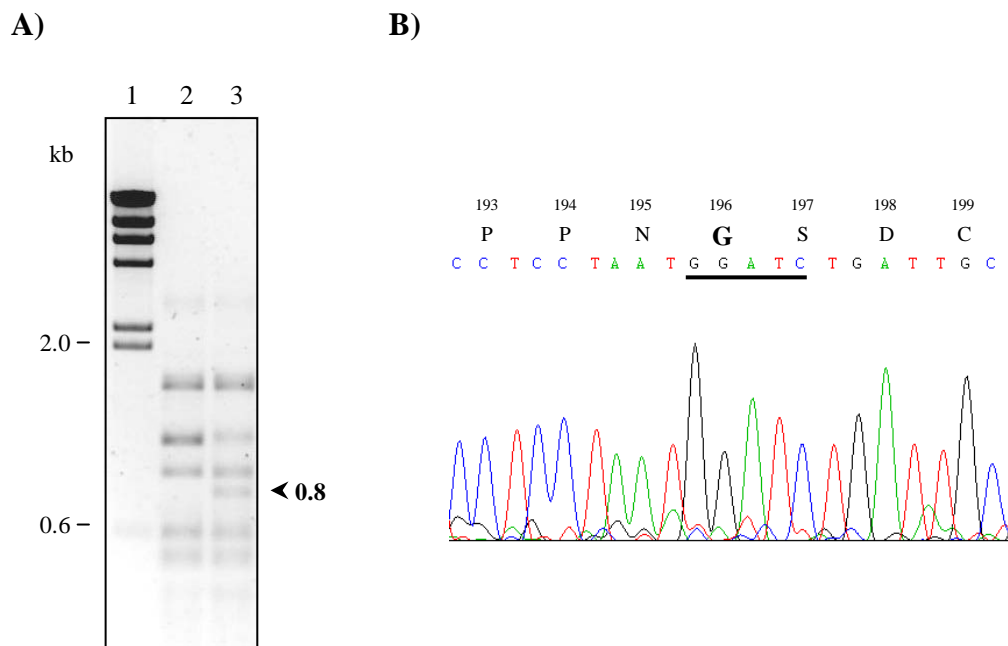


**Figure 5.12 Restriction digestion and DNA sequencing of pP196G**

**A)** 1.2% agarose gel electrophoresis (ethidium bromide-stained) of *Sau3AI* digestion patterns of the wild-type and mutant plasmids. The 0.8-kb mutant-specific DNA band is indicated.

Lane 1:  $\lambda$ /*HindIII* DNA markers

Lane 2: The *Sau3AI*-digested wild-type plasmid, pMEx-B4A

Lane 3: The *Sau3AI*-digested mutant plasmid, pP196G

**B)** DNA sequencing chromatogram of pP196G, using V147A-f as a sequencing primer. Part of the sense strand sequence is shown. Underlined letters indicate the mutated nucleotides. The bold letter represents the substituted amino acid residue.

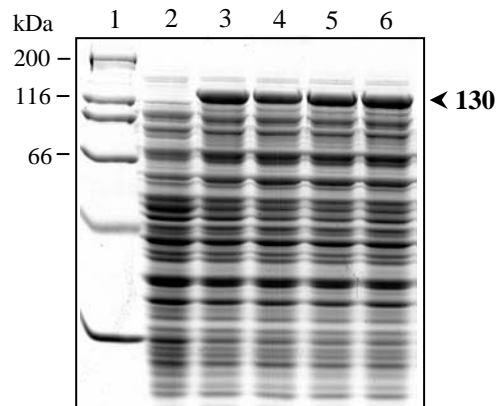


**Figure 5.13 Expression of Cry4Aa and its glycine-substituted mutants**

Coomassie blue-stained SDS-polyacrylamide gel (10%) shows protein profiles of lysates extracted from IPTG-induced *E. coli* cells containing each different plasmid. The expected bands of 130-kDa protoxins are indicated.

Lane 1: Molecular mass standards

Lane 2: Lysates extracted from *E. coli* cells containing the pMEx-8 plasmid

Lane 3: Lysates extracted from *E. coli* cells containing the pMEx-B4A plasmid

Lane 4: Lysates extracted from *E. coli* cells containing the pP193G plasmid

Lane 5: Lysates extracted from *E. coli* cells containing the pP194G plasmid

Lane 6: Lysates extracted from *E. coli* cells containing the pP196G plasmid

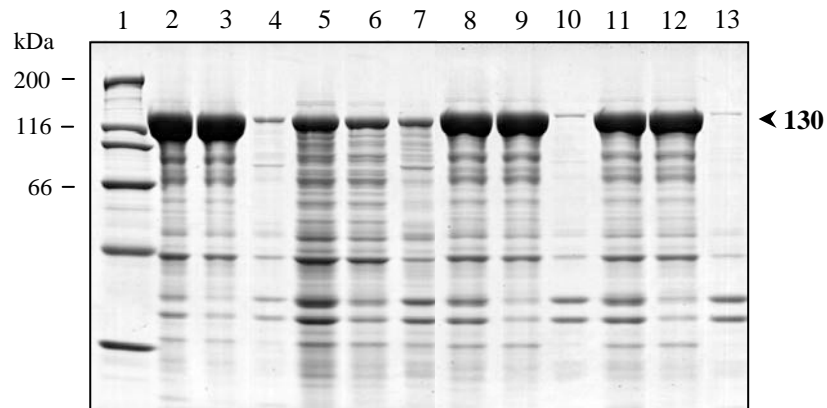


**Figure 5.14 Alkaline solubility of Cry4Aa and its glycine-substituted mutant inclusions**

Coomassie blue-stained SDS-polyacrylamide gel (10%) shows solubility of Cry4Aa and its glycine-substituted mutant inclusions in 50 mM Na<sub>2</sub>CO<sub>3</sub> buffer (pH 9.0). The bands of 130-kDa protoxins are indicated.

- Lane 1 : Molecular mass standards
- Lanes 2-4 : Total inclusion suspension, soluble fraction and insoluble pellet of Cry4Aa, respectively
- Lanes 5-7 : Total inclusion suspension, soluble fraction and insoluble pellet of P193G, respectively
- Lanes 8-10 : Total inclusion suspension, soluble fraction and insoluble pellet of P194G, respectively
- Lanes 11-13 : Total inclusion suspension, soluble fraction and insoluble pellet of P196G, respectively

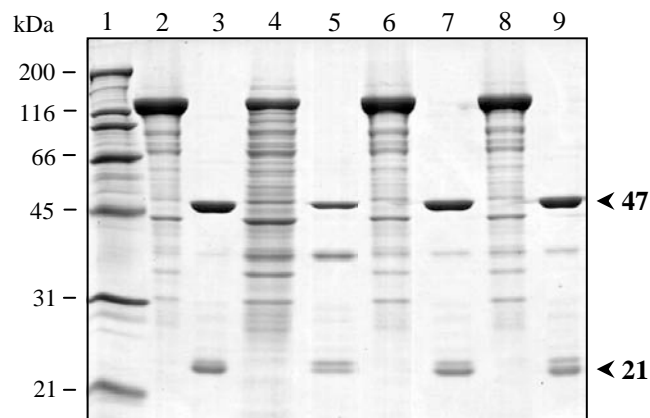


**Figure 5.15 Trypsin-digested products of Cry4Aa and its glycine-substituted mutants**

Coomassie blue-stained SDS-polyacrylamide gel (12%) shows tryptic processing of Cry4Aa and its glycine-substituted mutants. The expected bands of trypsin-treated products (ca. 47- and ca. 21-kDa) are indicated.

- Lane 1: Molecular mass standards
- Lane 2: Trypsin-untreated Cry4Aa protoxin
- Lane 3: Trypsin-treated products of Cry4Aa
- Lane 4: Trypsin-untreated P193G mutant protoxin
- Lane 5: Trypsin-treated products of P193G
- Lane 6: Trypsin-untreated P194G mutant protoxin
- Lane 7: Trypsin-treated products of P194G
- Lane 8: Trypsin-untreated P196G mutant protoxin
- Lane 9: Trypsin-treated products of P196G

Toxin	% Mortality				
	pMEx-8	Cry4Aa	P193G	P194G	P196G
Mean	0.6	80.6	33.6	56.0	62.6
SEM	0.3	6.9	5.6	8.0	2.1

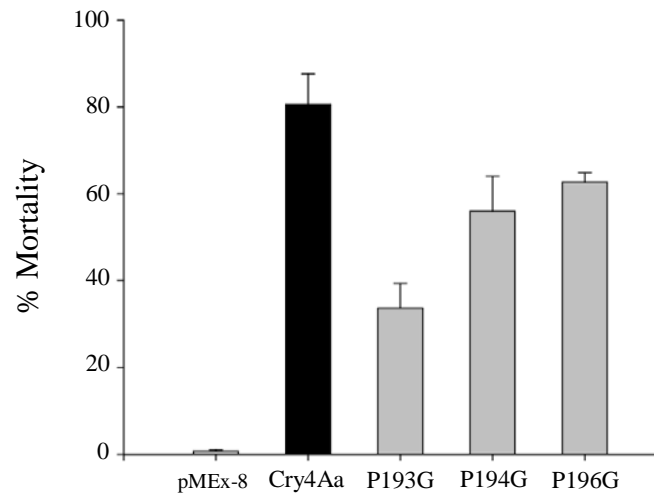


**Figure 5.16 Larvicidal activity of Cry4Aa and its glycine-substituted mutants**

The figure shows toxicity of *E. coli* cells ( $10^8$ ) expressing the Cry4Aa wild-type or its mutant toxins (P193G, P194G and P196G) against *A. aegypti* larvae. The control sample was *E. coli* cells carrying pMEx-8 vector. Error bars represent SEM from three independent experiments. Inserted table shows each value in details.

## 5.9 Constructions of Cry4Aa mutant plasmids substituted at the position 193

It can be noticed that mutations at Pro<sup>193</sup> (P193V and P193G) gave more adverse effects on larvicidal activity than those at Pro<sup>194</sup> and Pro<sup>196</sup> (P194V, P194G, P196V and P196G). According to Cry4Aa crystal structure (6), Pro<sup>193</sup> is located in the way that its pyrrolidine ring is closely parallel to benzene ring of Tyr<sup>133</sup> (**Figure 5.17**), thus suggesting an interaction between these two amino-acid residues. Such possible interaction may be involved in maintaining a functional structure of the Cry4Aa toxin. To test this notion, additional mutagenesis at position 193 (P193F, P193W and P193Y) was performed to see whether aromatic ring can compensate pyrrolidine ring of Pro<sup>193</sup> for possible interaction with Tyr<sup>133</sup>.

After PCR amplification, the amplified products were treated with *DpnI* endonuclease and analyzed on agarose gel. It was found that all PCR products showed a 7.4-kb major DNA band (**Figure 5.18**) that corresponds to pMEx-B4A. The mutant plasmids from *E. coli* transformants were first identified by restriction endonuclease digestion (**Figures 5.19A-5.21A**) and then verified by DNA sequencing. The results revealed that there was the required mutation at the desired position (**Figures 5.19B-5.21B**).

## 5.10 Expression of Cry4Aa mutant toxins substituted at the position 193

The plasmids encoding the 130-kDa Cry4Aa wild-type or mutant toxins were expressed in *E. coli* JM109 as inclusion bodies upon IPTG induction and the crude cell lysates were subjected to SDS-PAGE. As can be seen in **Figure 5.22**, the protein expression levels of all mutants (P193F, P193W and P193Y) are similar to that of the wild type.

### **5.11 Solubilization of Cry4Aa mutant toxins substituted at the position 193**

When inclusions of all mutant toxins (P193F, P193W and P193Y) were solubilized in carbonate buffer (pH 9.0), it was found that, unlike the wild type which was highly soluble, all the mutants exhibited a drastic reduction in inclusion solubility (**Figure 5.23**).

### **5.12 Mosquito-larvicidal activity of Cry4Aa mutant toxins substituted at the position 193**

When *E. coli* cells expressing each mutant toxin (P193F, P193W and P193Y) were tested for their relative toxicity towards *A. aegypti* larvae, a nearly complete loss in larvicidal activity was observed for all the mutant toxins (**Figure 5.24**).

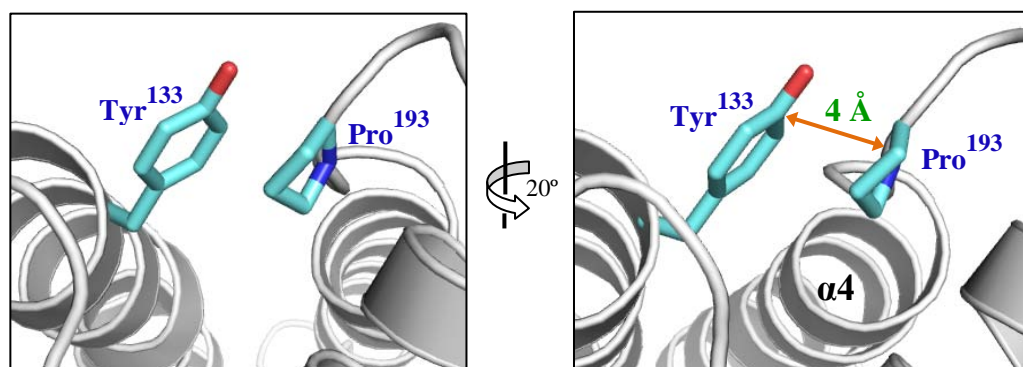


**Figure 5.17** Close-up views of part of Cry4Aa structure, illustrating orientation of Pro<sup>193</sup> and Tyr<sup>133</sup>

The figure shows side-chain orientation of Pro<sup>193</sup> and Tyr<sup>133</sup>. The distance between Pro<sup>193</sup>-pyrrolidine ring and Tyr<sup>133</sup>-benzene ring is indicated.

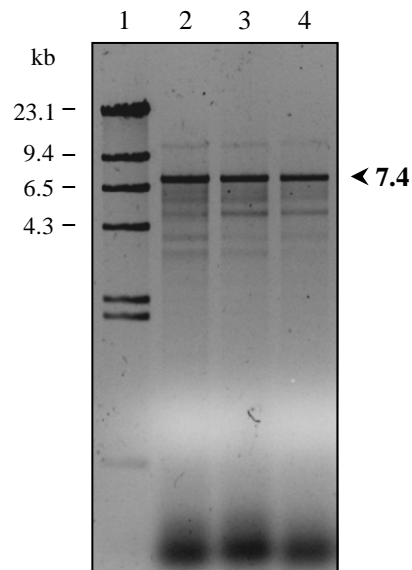


**Figure 5.18 PCR amplification of Cry4Aa mutant plasmids: pP193F, pP193W and pP193Y**

The figure shows 0.8% agarose gel electrophoresis (ethidium bromide-stained) of *DpnI*-treated PCR products of Cry4Aa mutant plasmids. The expected 7.4-kb DNA band in each lane is indicated with the bold label.

Lane 1:  $\lambda$ /*HindIII* DNA markers

Lane 2: The *DpnI*-treated PCR products of the pP193F plasmid

Lane 3: The *DpnI*-treated PCR products of the pP193W plasmid

Lane 4: The *DpnI*-treated PCR products of the pP193Y plasmid

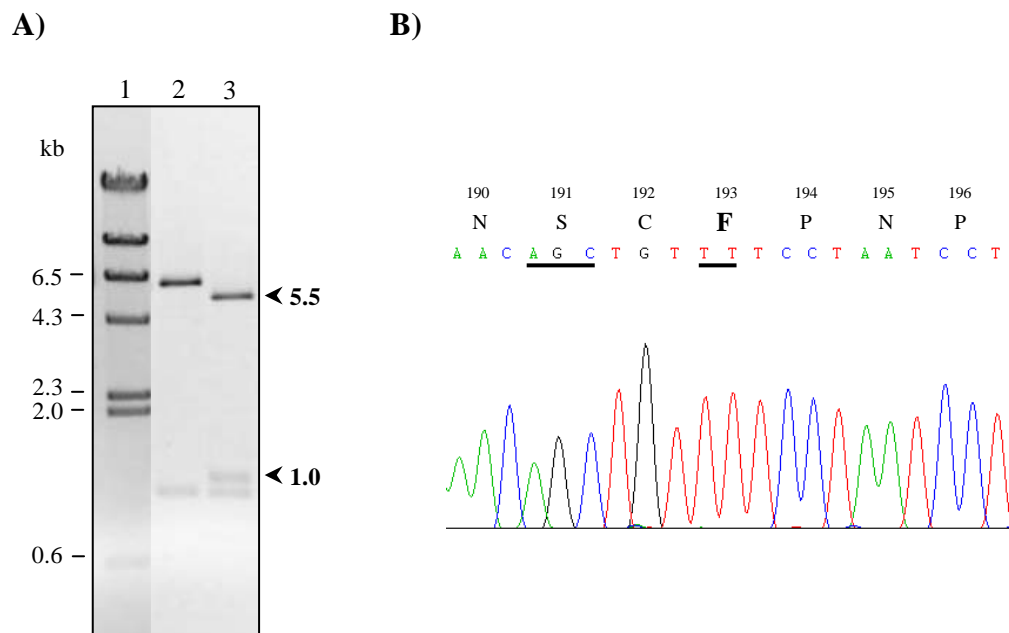


**Figure 5.19 Restriction digestion and DNA sequencing of pP193F**

**A)** 0.8% agarose gel electrophoresis (ethidium bromide-stained) of *Pvu*II digestion patterns of the wild-type and mutant plasmids. The 5.5- and 1.0-kb mutant-specific DNA bands are indicated.

Lane 1:  $\lambda$ /*Hind*III DNA markers

Lane 2: The *Pvu*II-digested wild-type plasmid, pMEx-B4A

Lane 3: The *Pvu*II-digested mutant plasmid, pP193F

**B)** DNA sequencing chromatogram of pP193F, using V147A-f as a sequencing primer. Part of the sense strand sequence is shown. Underlined letters indicate the mutated nucleotides. The bold letter represents the substituted amino acid residue.

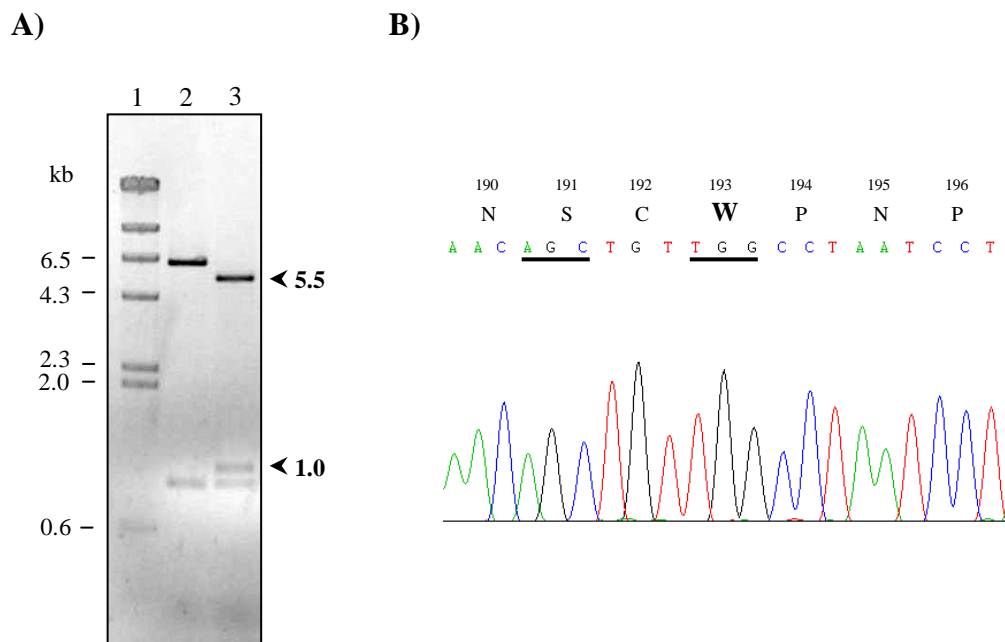


**Figure 5.20 Restriction digestion and DNA sequencing of pP193W**

**A)** 0.8% agarose gel electrophoresis (ethidium bromide-stained) of *PvuII* digestion patterns of the wild-type and mutant plasmids. The 5.5- and 1.0-kb mutant-specific DNA bands are indicated.

Lane 1:  $\lambda$ /*HindIII* DNA markers

Lane 2: The *PvuII*-digested wild-type plasmid, pMEx-B4A

Lane 3: The *PvuII*-digested mutant plasmid, pP193W

**B)** DNA sequencing chromatogram of pP193W, using V147A-f as a sequencing primer. Part of the sense strand sequence is shown. Underlined letters indicate the mutated nucleotides. The bold letter represents the substituted amino acid residue.

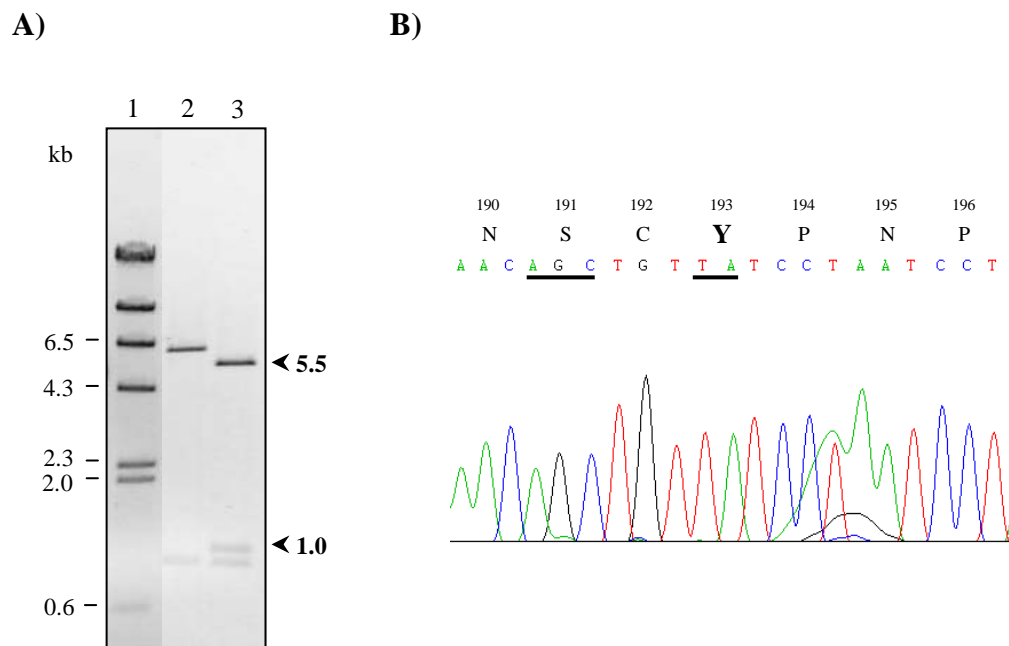


**Figure 5.21 Restriction digestion and DNA sequencing of pP193Y**

**A)** 0.8% agarose gel electrophoresis (ethidium bromide-stained) of *Pvu*II digestion patterns of the wild-type and mutant plasmids. The 5.5- and 1.0-kb mutant-specific DNA bands are indicated.

Lane 1:  $\lambda$ /*Hind*III DNA markers

Lane 2: The *Pvu*II-digested wild-type plasmid, pMEx-B4A

Lane 3: The *Pvu*II-digested mutant plasmid, pP193Y

**B)** DNA sequencing chromatogram of pP193Y, using V147A-f as a sequencing primer. Part of the sense strand sequence is shown. Underlined letters indicate the mutated nucleotides. The bold letter represents the substituted amino acid residue.

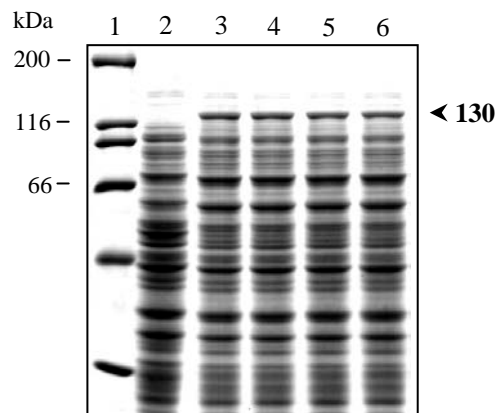


**Figure 5.22 Expression of Cry4Aa and its mutants substituted at the position 193**

Coomassie blue-stained SDS-polyacrylamide gel (10%) shows protein profiles of lysates extracted from IPTG-induced *E. coli* cells containing each different plasmid. The expected bands of 130-kDa protoxins are indicated.

Lane 1: Molecular mass standards

Lane 2: Lysates extracted from *E. coli* cells containing the pMEx-8 plasmid

Lane 3: Lysates extracted from *E. coli* cells containing the pMEx-B4A plasmid

Lane 4: Lysates extracted from *E. coli* cells containing the pP193F plasmid

Lane 5: Lysates extracted from *E. coli* cells containing the pP193W plasmid

Lane 6: Lysates extracted from *E. coli* cells containing the pP193Y plasmid

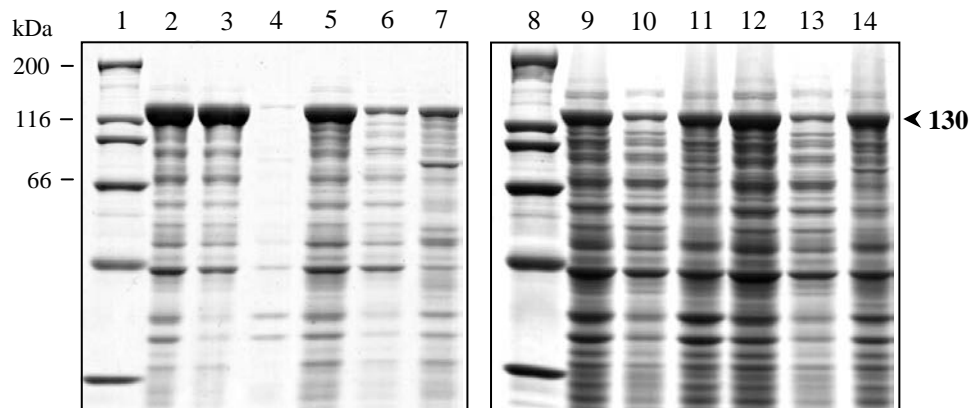


**Figure 5.23 Alkaline solubility of Cry4Aa and its mutant inclusions substituted at the position 193**

Coomassie blue-stained SDS-polyacrylamide gel (10%) shows solubility of Cry4Aa and its mutant inclusions substituted at the position 193 in 50 mM Na<sub>2</sub>CO<sub>3</sub> buffer (pH 9.0). The bands of 130-kDa protoxins are indicated.

- Lanes 1 and 8 : Molecular mass standard
- Lanes 2-4 : Total inclusion suspension, soluble fraction and insoluble pellet of Cry4Aa, respectively
- Lanes 5-7 : Total inclusion suspension, soluble fraction and insoluble pellet of P193F, respectively
- Lanes 9-11 : Total inclusion suspension, soluble fraction and insoluble pellet of P193W, respectively
- Lanes 12-14 : Total inclusion suspension, soluble fraction and insoluble pellet of P193Y, respectively

Toxin	% Mortality				
	pMEx-8	Cry4Aa	P193F	P193W	P193Y
Mean	2.0	81.3	4.0	9.6	3.0
SEM	1.4	6.1	3.3	8.0	3.7

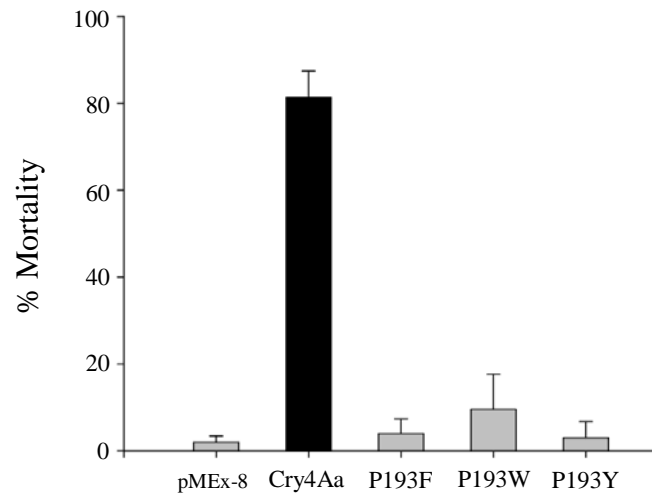


**Figure 5.24 Larvicidal activity of Cry4Aa and its mutants substituted at the position 193**

The figure shows toxicity of *E. coli* cells ( $10^8$ ) expressing the Cry4Aa wild-type or its mutant toxins (P193F, P193W and P193Y) against *A. aegypti* larvae. The control sample was *E. coli* cells carrying pMEx-8 vector. Error bars represent SEM from three independent experiments. Inserted table shows each value in details.

## CHAPTER VI

### RESULT III: PROLINE-SCANNING MUTAGENESIS IN $\alpha 4$ - $\alpha 5$ LOOP OF Cry4Aa TOXIN

As shown in **Chapter V**, proline residues (Pro<sup>193</sup>, Pro<sup>194</sup> and Pro<sup>196</sup>) within the  $\alpha 4$ - $\alpha 5$  loop of Cry4Aa are essential for biological function and structural conformation of the toxin. In this chapter, proline-scanning mutagenesis in the Cry4Aa  $\alpha 4$ - $\alpha 5$  loop was performed to determine whether importance of the loop proline residues is position-dependent.

#### 6.1 Constructions of proline-substituted Cry4Aa mutant plasmids

Seven mutant plasmids (pS191P, pC192P, pN195P, pS197P, pD198P, pC199P and pD200P) were generated by PCR-based mutagenesis using pMEx-B4A plasmid as a template. The PCR products showed the expected size of 7.4 kb after being digested with *DpnI* as shown in **Figure 6.1**. The mutant plasmids from *E. coli* transformants were first identified by restriction endonuclease digestion (**Figures 6.2A-6.8A**), and then verified by DNA sequencing (**Figures 6.2B-6.8B**).

#### 6.2 Expression of proline-substituted Cry4Aa mutant toxins

The proline-substituted mutant toxins (S191P, C192P, N195P, S197P, D198P, C199P and D200P) were expressed in *E. coli* cells upon IPTG induction. When *E. coli* lysates were analyzed by SDS-PAGE, it was found that protein expression levels of all mutants are similar to that of the wild type (**Figure 6.9**).

### **6.3 Solubilization and proteolytic processing of proline-substituted Cry4Aa mutant toxins**

Solubility analysis of the proline-substituted mutants revealed that toxin inclusions of N195P and S197P mutants were soluble in carbonate buffer (pH 9.0), giving almost 100% solubility which is comparable with solubility of the wild-type inclusion under the same condition. In contrast, a reduction or a complete loss of inclusion solubility was observed for the five other mutants (S191P, C192P, D198P, C199P and D200P) (**Figures 6.10-6.11**).

After soluble protoxins (130-kDa) of the N195P and S197P were treated with trypsin and analyzed on SDS-polyacrylamide gel in comparison with that of the wild type, it was found that all were digested into two major trypsin-resistant fragments of ca. 47 and ca. 21 kDa (**Figure 6.12**).

### **6.4 Mosquito-larvicidal activity of proline-substituted Cry4Aa mutant toxins**

*E. coli* cells expressing each proline-substituted mutant were tested for their toxicity against *A. aegypti* larvae. As can be seen in **Figure 6.13**, all proline substitutions, except S197P, adversely affected larvicidal activity.

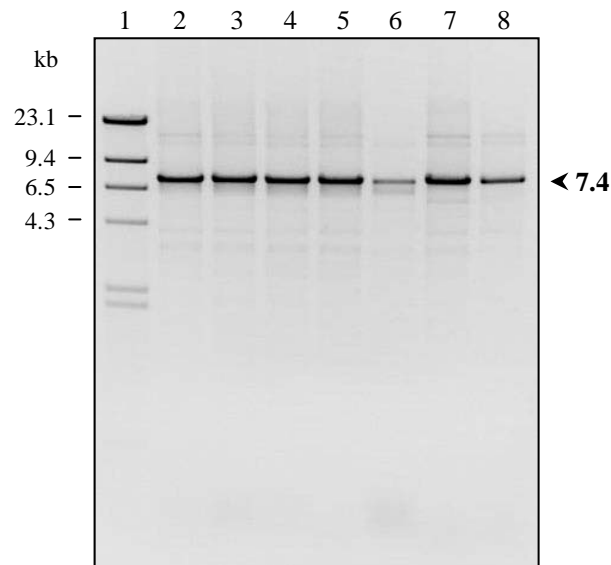


**Figure 6.1 PCR amplification of Cry4Aa mutant plasmids: pS191P, pC192P, pN195P, pS197P, pD198P, pC199P and pD200P**

The figure shows 0.8% agarose gel electrophoresis (ethidium bromide-stained) of *DpnI*-treated PCR products of Cry4Aa mutant plasmids. The expected 7.4-kb DNA band in each lane is indicated with the bold label.

Lane 1:  $\lambda$ /*Hind*III DNA markers

Lane 2: The *DpnI*-treated PCR products of the pS191P plasmid

Lane 3: The *DpnI*-treated PCR products of the pC192P plasmid

Lane 4: The *DpnI*-treated PCR products of the pN195P plasmid

Lane 5: The *DpnI*-treated PCR products of the pS197P plasmid

Lane 6: The *DpnI*-treated PCR products of the pD198P plasmid

Lane 7: The *DpnI*-treated PCR products of the pC199P plasmid

Lane 8: The *DpnI*-treated PCR products of the pD200P plasmid

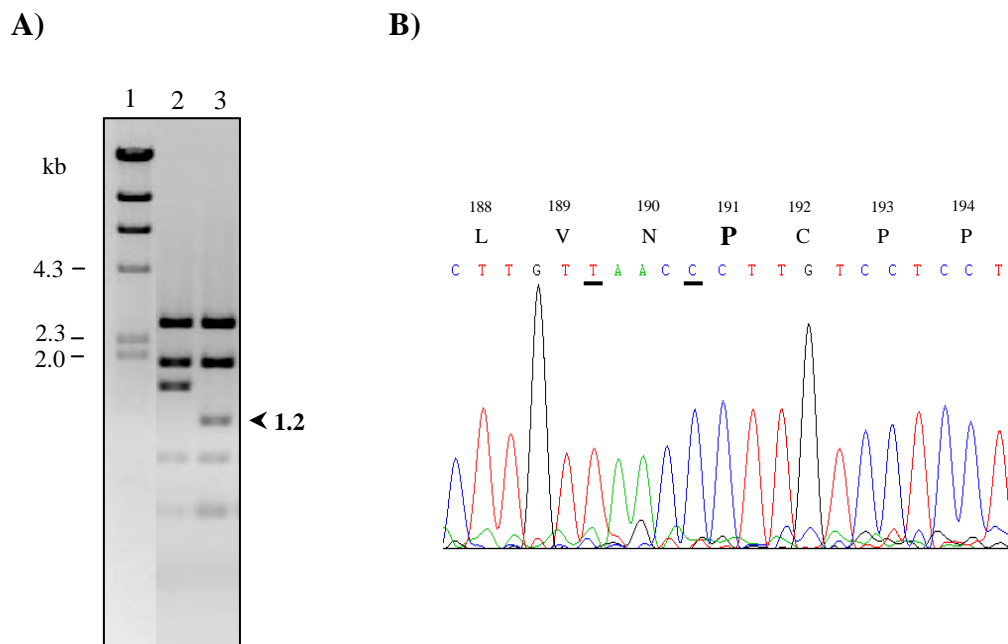


**Figure 6.2 Restriction digestion and DNA sequencing of pS191P**

**A)** 0.8% agarose gel electrophoresis (ethidium bromide-stained) of *HincII* digestion patterns of the wild-type and mutant plasmids. The 1.2-kb mutant-specific DNA band is indicated.

Lane 1:  $\lambda$ /*HindIII* DNA markers

Lane 2: The *HincII*-digested wild-type plasmid, pMEx-B4A

Lane 3: The *HincII*-digested mutant plasmid, pS191P

**B)** DNA sequencing chromatogram of pS191P, using V147A-f as a sequencing primer. Part of the sense strand sequence is shown. Underlined letters indicate the mutated nucleotides. The bold letter represents the substituted amino acid residue.

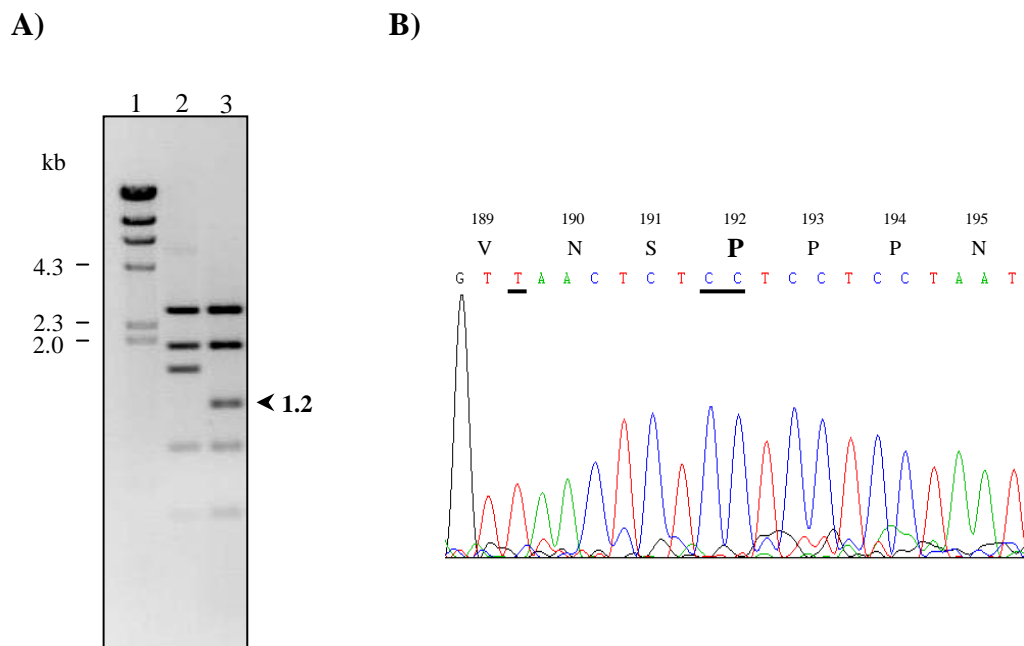


**Figure 6.3 Restriction digestion and DNA sequencing of pC192P**

**A)** 1.0% agarose gel electrophoresis (ethidium bromide-stained) of *HincII* digestion patterns of the wild-type and mutant plasmids. The 1.2-kb mutant-specific DNA band is indicated.

Lane 1:  $\lambda$ /*HindIII* DNA markers

Lane 2: The *HincII*-digested wild-type plasmid, pMEx-B4A

Lane 3: The *HincII*-digested mutant plasmid, pC192P

**B)** DNA sequencing chromatogram of pC192P, using V147A-f as a sequencing primer. Part of the sense strand sequence is shown. Underlined letters indicate the mutated nucleotides. The bold letter represents the substituted amino acid residue.

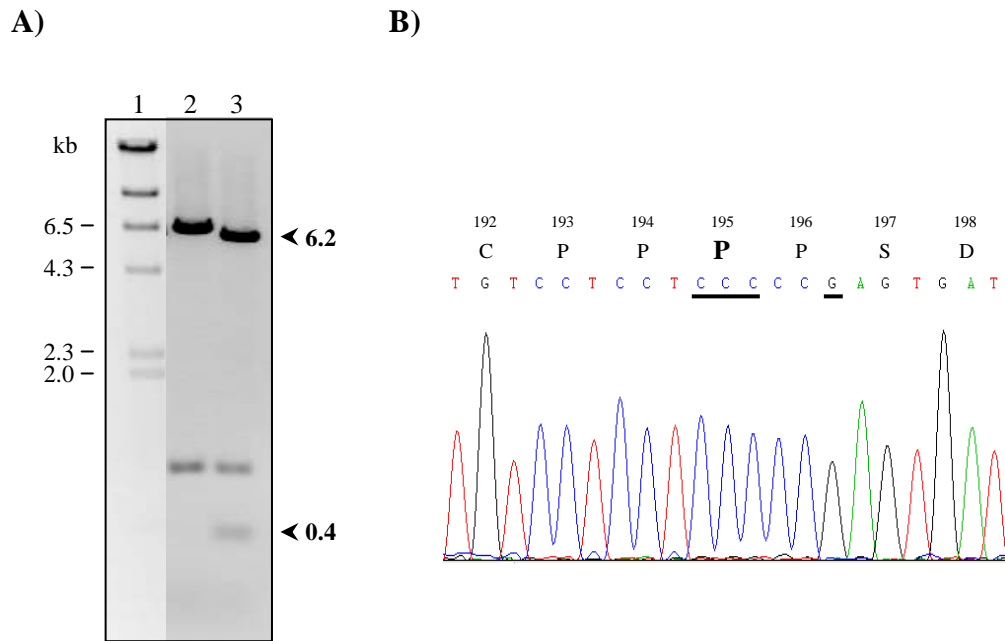


**Figure 6.4 Restriction digestion and DNA sequencing of pN195P**

**A)** 0.8% agarose gel electrophoresis (ethidium bromide-stained) of *Ava*I digestion patterns of the wild-type and mutant plasmids. The 6.2- and 0.4-kb mutant-specific DNA bands are indicated.

Lane 1:  $\lambda$ /*Hind*III DNA markers

Lane 2: The *Ava*I-digested wild-type plasmid, pMEx-B4A

Lane 3: The *Ava*I-digested mutant plasmid, pN195P

**B)** DNA sequencing chromatogram of pN195P, using V147A-f as a sequencing primer. Part of the sense strand sequence is shown. Underlined letters indicate the mutated nucleotides. The bold letter represents the substituted amino acid residue.

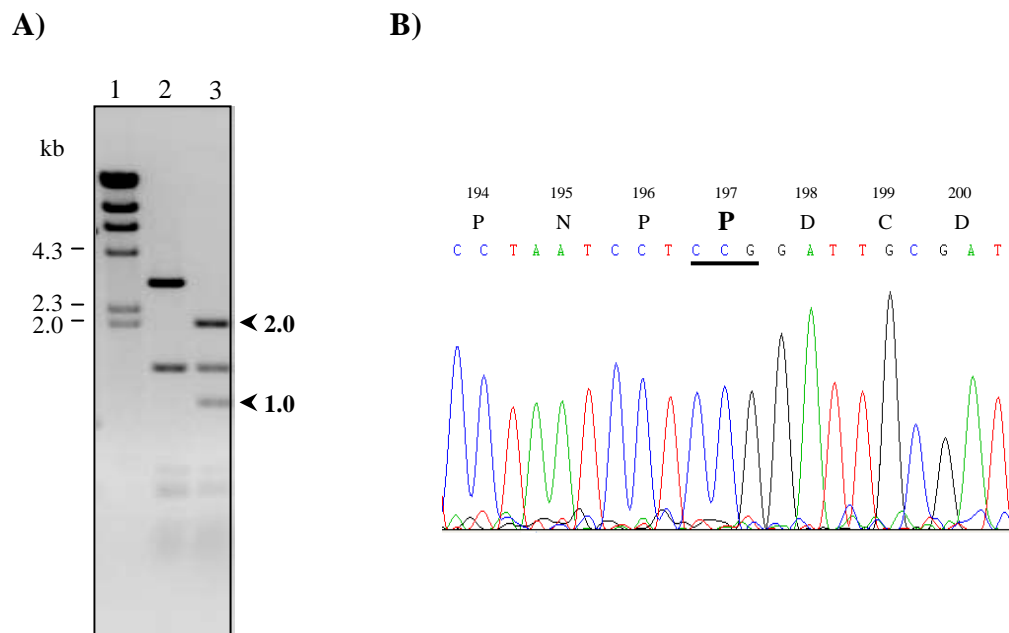


**Figure 6.5 Restriction digestion and DNA sequencing of pS197P**

**A)** 1.0% agarose gel electrophoresis (ethidium bromide-stained) of *Hpa*II digestion patterns of the wild-type and mutant plasmids. The 2.0- and 1.0-kb mutant-specific DNA bands are indicated.

Lane 1:  $\lambda$ /*Hind*III DNA markers

Lane 2: The *Hpa*II-digested wild-type plasmid, pMEx-B4A

Lane 3: The *Hpa*II-digested mutant plasmid, pS197P

**B)** DNA sequencing chromatogram of pS197P, using V147A-f as a sequencing primer. Part of the sense strand sequence is shown. Underlined letters indicate the mutated nucleotides. The bold letter represents the substituted amino acid residue.

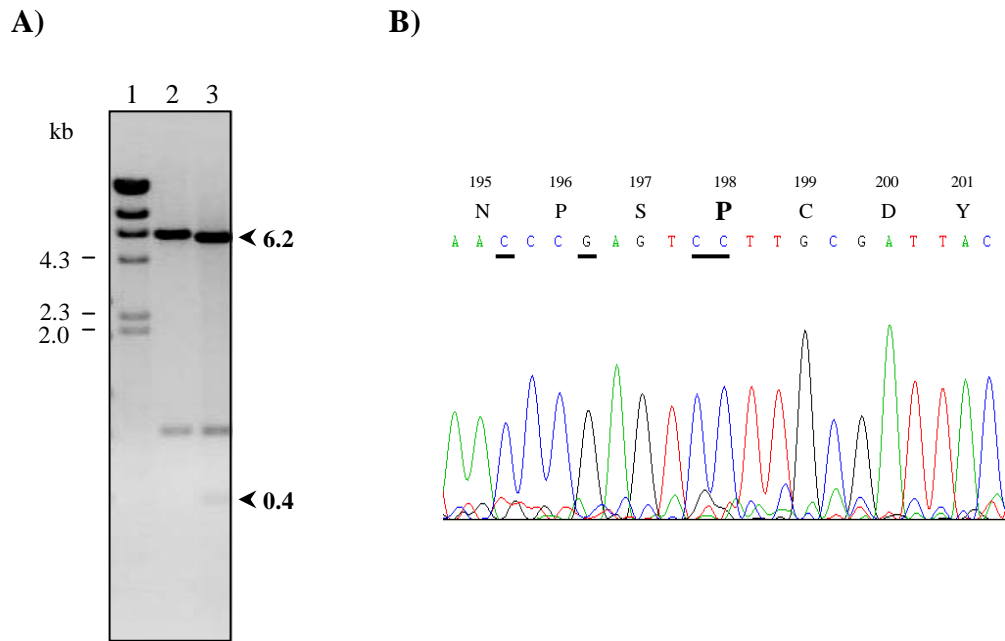


**Figure 6.6 Restriction digestion and DNA sequencing of pD198P**

**A)** 1.0% agarose gel electrophoresis (ethidium bromide-stained) of *AvaI* digestion patterns of the wild-type and mutant plasmids. The 6.2- and 0.4-kb mutant-specific DNA bands are indicated.

Lane 1:  $\lambda$ /*HindIII* DNA markers

Lane 2: The *AvaI*-digested wild-type plasmid, pMEx-B4A

Lane 3: The *AvaI*-digested mutant plasmid, pD198P

**B)** DNA sequencing chromatogram of pD198P, using V147A-f as a sequencing primer. Part of the sense strand sequence is shown. Underlined letters indicate the mutated nucleotides. The bold letter represents the substituted amino acid residue.

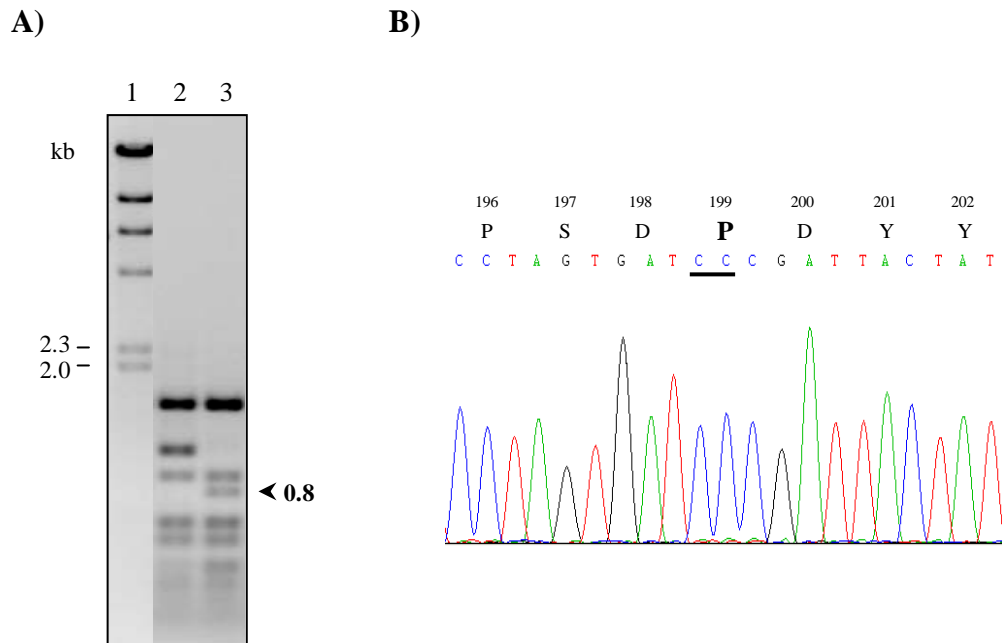


**Figure 6.7 Restriction digestion and DNA sequencing of pC199P**

**A)** 0.8% agarose gel electrophoresis (ethidium bromide-stained) of *DpnI* digestion patterns of the wild-type and mutant plasmids. The 0.8-kb mutant-specific DNA band is indicated.

Lane 1:  $\lambda$ /*HindIII* DNA markers

Lane 2: The *DpnI*-digested wild-type plasmid, pMEx-B4A

Lane 3: The *DpnI*-digested mutant plasmid, pC199P

**B)** DNA sequencing chromatogram of pC199P, using V147A-f as a sequencing primer. Part of the sense strand sequence is shown. Underlined letters indicate the mutated nucleotides. The bold letter represents the substituted amino acid residue.

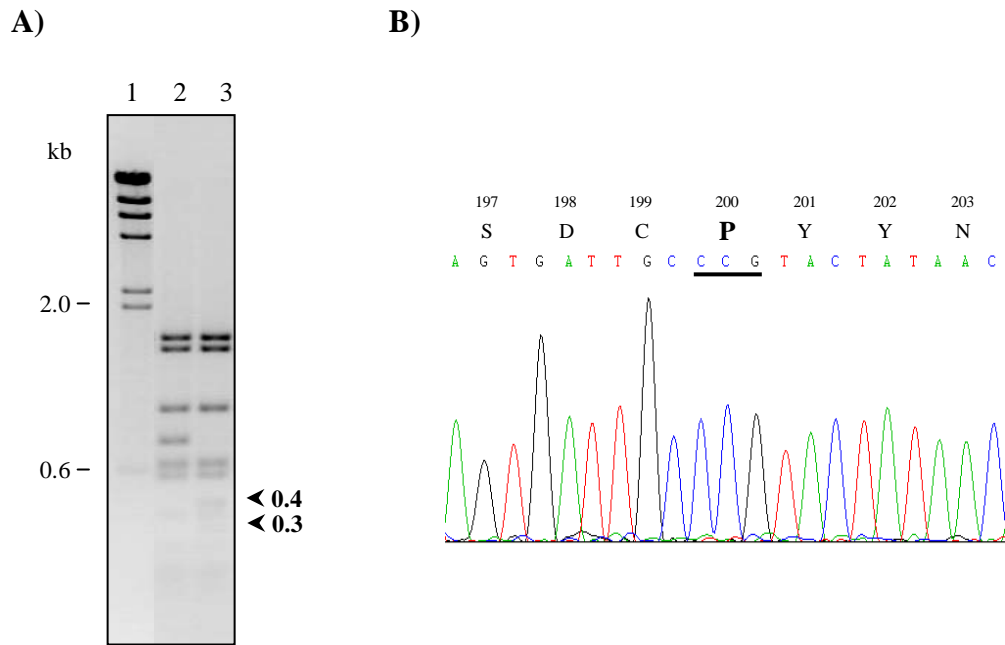


**Figure 6.8 Restriction digestion and DNA sequencing of pD200P**

**A)** 1.5% agarose gel electrophoresis (ethidium bromide-stained) of *RsaI* digestion patterns of the wild-type and mutant plasmids. The 0.4- and 0.3-kb mutant-specific DNA bands are indicated.

Lane 1:  $\lambda$ /*HindIII* DNA markers

Lane 2: The *RsaI*-digested wild-type plasmid, pMEx-B4A

Lane 3: The *RsaI*-digested mutant plasmid, pD200P

**B)** DNA sequencing chromatogram of pD200P, using V147A-f as a sequencing primer. Part of the sense strand sequence is shown. Underlined letters indicate the mutated nucleotides. The bold letter represents the substituted amino acid residue.

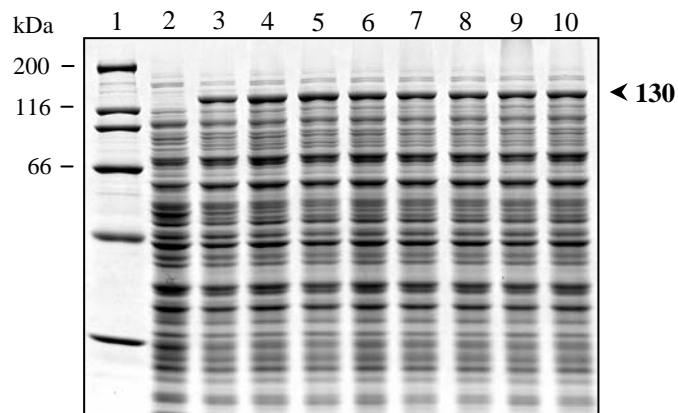


**Figure 6.9 Expression of Cry4Aa and its proline-substituted mutants**

Coomassie blue-stained SDS-polyacrylamide gel (10%) shows protein profiles of lysates extracted from IPTG-induced *E. coli* cells containing each different plasmid. The expected bands of 130-kDa protoxins are indicated.

- Lane 1 : Molecular mass standards
- Lane 2 : Lysates extracted from *E. coli* cells containing the pMEx-8 plasmid
- Lane 3 : Lysates extracted from *E. coli* cells containing the pMEx-B4A plasmid
- Lane 4 : Lysates extracted from *E. coli* cells containing the pS191P plasmid
- Lane 5 : Lysates extracted from *E. coli* cells containing the pC192P plasmid
- Lane 6 : Lysates extracted from *E. coli* cells containing the pN195P plasmid
- Lane 7 : Lysates extracted from *E. coli* cells containing the pS197P plasmid
- Lane 8 : Lysates extracted from *E. coli* cells containing the pD198P plasmid
- Lane 9 : Lysates extracted from *E. coli* cells containing the pC199P plasmid
- Lane 10 : Lysates extracted from *E. coli* cells containing the pD200P plasmid

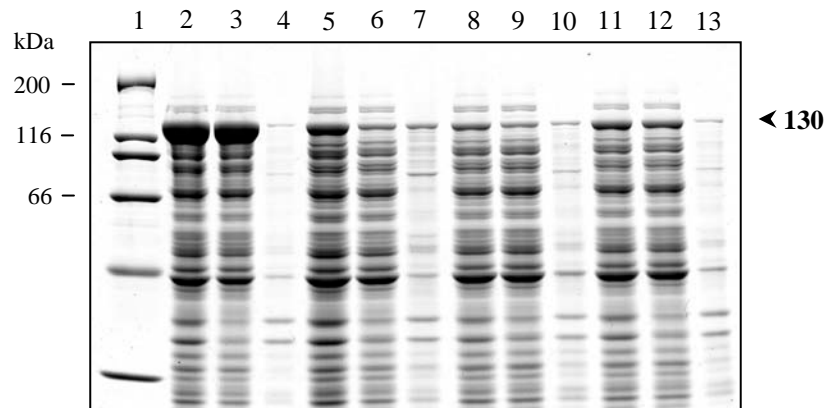


**Figure 6.10 Alkaline solubility of Cry4Aa and its proline-substituted mutant inclusions**

Coomassie blue-stained SDS-polyacrylamide gel (10%) shows solubility of Cry4Aa and its proline-substituted mutant inclusions in 50 mM Na<sub>2</sub>CO<sub>3</sub> buffer (pH 9.0). The bands of 130-kDa protoxins are indicated.

- Lane 1 : Molecular mass standards
- Lanes 2-4 : Total inclusion suspension, soluble fraction and insoluble pellet of Cry4Aa, respectively
- Lanes 5-7 : Total inclusion suspension, soluble fraction and insoluble pellet of S191P, respectively
- Lanes 8-10 : Total inclusion suspension, soluble fraction and insoluble pellet of C192P, respectively
- Lanes 11-13 : Total inclusion suspension, soluble fraction and insoluble pellet of N195P, respectively

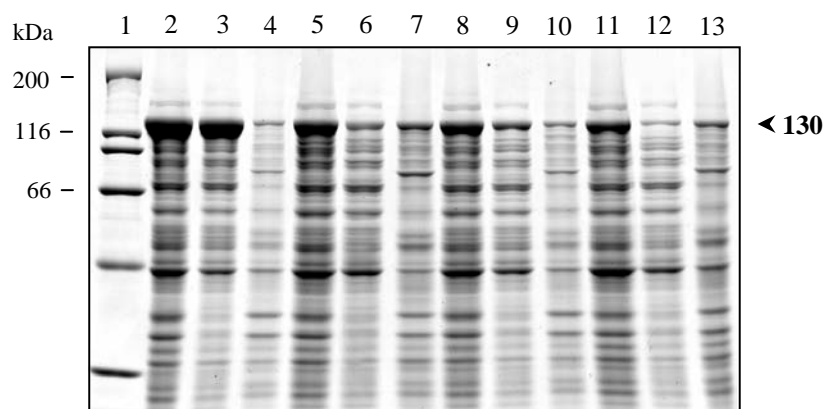


**Figure 6.11 Alkaline solubility of proline-substituted Cry4Aa mutant inclusions**

Coomassie blue-stained SDS-polyacrylamide gel (10%) shows solubility of proline-substituted Cry4Aa mutant inclusions in 50 mM  $\text{Na}_2\text{CO}_3$  buffer (pH 9.0). The bands of 130-kDa protoxins are indicated.

- Lane 1 : Molecular mass standards
- Lanes 2-4 : Total inclusion suspension, soluble fraction and insoluble pellet of S197P, respectively
- Lanes 5-7 : Total inclusion suspension, soluble fraction and insoluble pellet of D198P, respectively
- Lanes 8-10 : Total inclusion suspension, soluble fraction and insoluble pellet of C199P, respectively
- Lanes 11-13 : Total inclusion suspension, soluble fraction and insoluble pellet of D200P, respectively

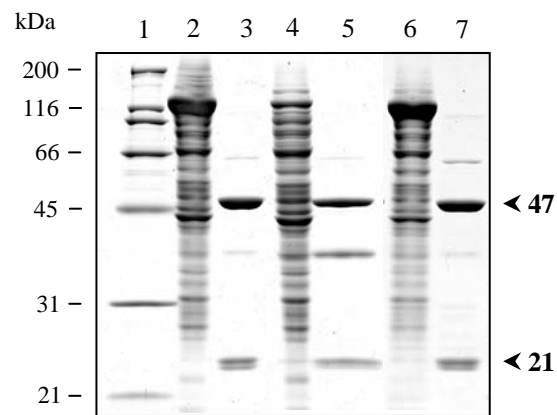


**Figure 6.12 Trypsin-digested products of Cry4Aa and its proline-substituted mutants**

Coomassie blue-stained SDS-polyacrylamide gel (12%) shows tryptic processing of Cry4Aa and its proline-substituted mutants. The expected bands of trypsin-treated products (ca. 47- and ca. 21-kDa) are indicated.

Lane 1: Molecular mass standards

Lane 2: Trypsin-untreated Cry4Aa protoxin

Lane 3: Trypsin-treated products of Cry4Aa

Lane 4: Trypsin-untreated N195P mutant protoxin

Lane 5: Trypsin-treated products of N195P

Lane 6: Trypsin-untreated S197P mutant protoxin

Lane 7: Trypsin-treated products of S197P

Toxin	% Mortality								
	pMEx-8	Cry4Aa	S191P	C192P	N195P	S197P	D198P	C199P	D200P
Mean	0.3	77.0	4.6	5.3	36.3	74.3	3.3	10.3	9.3
SEM	0.3	3.6	2.3	0.3	6.9	3.8	1.8	3.2	2.9

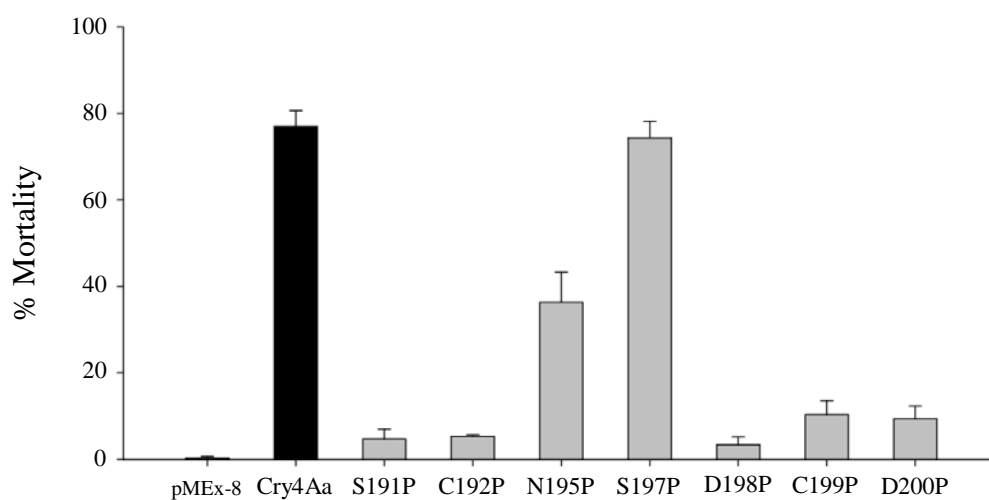


**Figure 6.13 Larvicidal activity of Cry4Aa and its proline-substituted mutants**

The figure shows toxicity of *E. coli* cells ( $10^8$ ) expressing the Cry4Aa wild-type or its mutant toxins (S191P, C192P, N195P, S197P, D198P, C199P and D200P) against *A. aegypti* larvae. The control sample was *E. coli* cells carrying pMEx-8 vector. Error bars represent SEM from three independent experiments. Inserted table shows each value in details.

## CHAPTER VII

### RESULT IV: CHARACTERIZATION OF Cry4Aa AND ITS MUTANT TOXINS

As shown in **Chapter V**, Cry4Aa mutant toxins with a substitution at individual proline residues (Pro<sup>193</sup>, Pro<sup>194</sup> and Pro<sup>196</sup>) in the Cry4Aa  $\alpha$ 4- $\alpha$ 5 loop exhibited a reduction in larvicidal activity, thus indicating the importance of these loop proline residues for toxin function. In this chapter, other structural and functional properties of such mutants were further examined in comparison with those of the Cry4Aa wild type.

#### **7.1 Purification of Cry4Aa and its glycine-substituted mutant toxins**

After solubilization and trypsin digestion in 50 mM Na<sub>2</sub>CO<sub>3</sub> (pH 9.0), the 65-kDa activated Cry4Aa wild-type and mutant toxins (P193G, P194G and P196G) were subjected to size-exclusion FPLC (Superose 12 GL 10/300 column), which was equilibrated with carbonated buffer (pH 9.0). It was found that purified activated toxins (65-kDa) were eluted as a peak at the volume of 12 ml (indicated by arrow in **Figures 7.1A-7.4A**). These peak fractions were then analyzed on SDS-polyacrylamide gel (**Figures 7.1B-7.4B**) and used for further characterization.

#### **7.2 Structural determination of Cry4Aa and its glycine-substituted mutant toxins**

Intrinsic fluorescence of 65-kDa purified Cry4Aa wild-type and mutant toxins (P193G, P194G and P196G) was measured by using a spectrofluorometer. As can be seen in **Figure 7.5**, fluorescence spectra of all mutants were similar to that of the wild type, suggesting that their overall tertiary structures are the same.

### 7.3 Disulfide bond determination of Cry4Aa and its glycine-substituted mutant toxins

The existence of Cys<sup>192</sup>-Cys<sup>199</sup> bond in 21-kDa fragment (corresponding to the first five helices of Cry4Aa-domain I) of activated Cry4Aa mutant toxins (P193G, P194G and P196G) was determined, in comparison with that of the wild-type toxin, by assaying the mobility of the 21-kDa  $\alpha$ 1- $\alpha$ 5 fragment under reducing and non-reducing conditions on SDS-polyacrylamide gel. This assay is based on the fact that the electrophoretic mobility of the  $\alpha$ 1- $\alpha$ 5 fragment is faster in the presence of the disulfide bond. **Figure 7.6** shows that the 21-kDa fragments of all mutant toxins, as well as that of the wild-type toxin, ran differently in the absence and presence of DTT, indicating the existence of the Cys<sup>192</sup>-Cys<sup>199</sup> bond in the  $\alpha$ 1- $\alpha$ 5 fragment of all mutant toxins.

### 7.4 Membrane-perturbing activity of Cry4Aa and its glycine-substituted mutant toxins

Release activity of the 65-kDa purified Cry4Aa against calcein-entrapped hybrid liposomes was evaluated at various protein concentrations (1.5, 3.0, 12.5, 25.0, 50.0 and 75.0  $\mu$ g/ml) and the concentration-versus-release activity profile was generated. It was found that the leakage of entrapped calcein increased logarithmically with toxin concentration (**Figure 7.7**).

When Cry4Aa mutant toxins (P193G, P194G and P196G) were tested for their membrane-perturbing activity in comparison with the wild-type toxin, a similarity in calcein-release activity was observed between the wild type and all these three mutants (**Figure 7.8**).

### 7.5 Structural analysis of Cry4Aa and its mutant toxins substituted at the position 193

Structural analysis of the three critical proline residues (Pro<sup>193</sup>, Pro<sup>194</sup> and Pro<sup>196</sup>) within the Cry4Aa  $\alpha$ 4- $\alpha$ 5 loop revealed that side chain of Pro<sup>193</sup> points inwards into the toxin molecule while those of Pro<sup>194</sup> and Pro<sup>196</sup> point outwards (**Figure 7.9**).

Further structural analysis showed that mutations at the position 193 led to an alteration in the interactions between the substituents and their neighboring residues, *i.e.*, P193G mutation introduced a cavity between the Gly<sup>193</sup> and its surroundings, whereas P193V, P193F, P193Y and P193W mutations caused a side-chain overlap effect (**Figure 7.10**).

Structural analysis *via* MD simulations revealed that substitutions at the position 193 (P193G and P193V) resulted in a structural rearrangement around this position. Different from the wild type-Pro<sup>193</sup> which is surrounded by hydrophobic environment including benzene ring of Tyr<sup>133</sup>, the substituents (Gly<sup>193</sup> and Val<sup>193</sup>) were found to be surface-exposed as the Tyr<sup>133</sup> moved to form H-bond with Asp<sup>198</sup> (**Figure 7.11**).

## 7.6 RMSF value determination of Cry4Aa-domain I

The last 4 ns of MD trajectories from 10-ns simulations of the Cry4Aa wild type was used for calculation of C<sub>α</sub>-RMSF value. It was found that RMSF values are high at each loop region (**Figure 7.12A**), indicating a large flexibility of the loop structure compared with helical structure. Among Cry4Aa's domain-I loop, the α4-α5 loop, which is not the shortest loop and possesses unique structural features (**Figure 7.12B**), showed the lowest RMSF value, signifying that this loop is substantially stable.

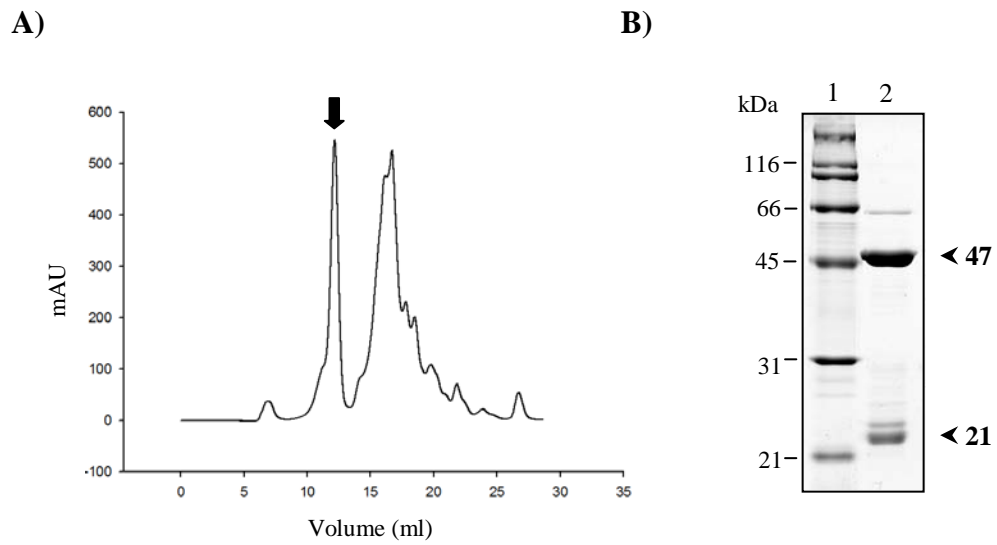


**Figure 7.1 Chromatogram and SDS-PAGE analysis of purified Cry4Aa toxin**

- A)** FPLC chromatogram from size-exclusion chromatography of purified Cry4Aa toxin. The peak corresponding to the purified 65-kDa Cry4Aa toxin is indicated.
- B)** Coomassie blue-stained SDS-polyacrylamide gel (12%) of the purified fraction of the Cry4Aa toxin.

Lane 1 : Molecular mass standards

Lane 2 : The purified fraction of the 65-kDa Cry4Aa toxin (comprising two non-covalently associated fragments of ca. 47 and ca. 21 kDa)

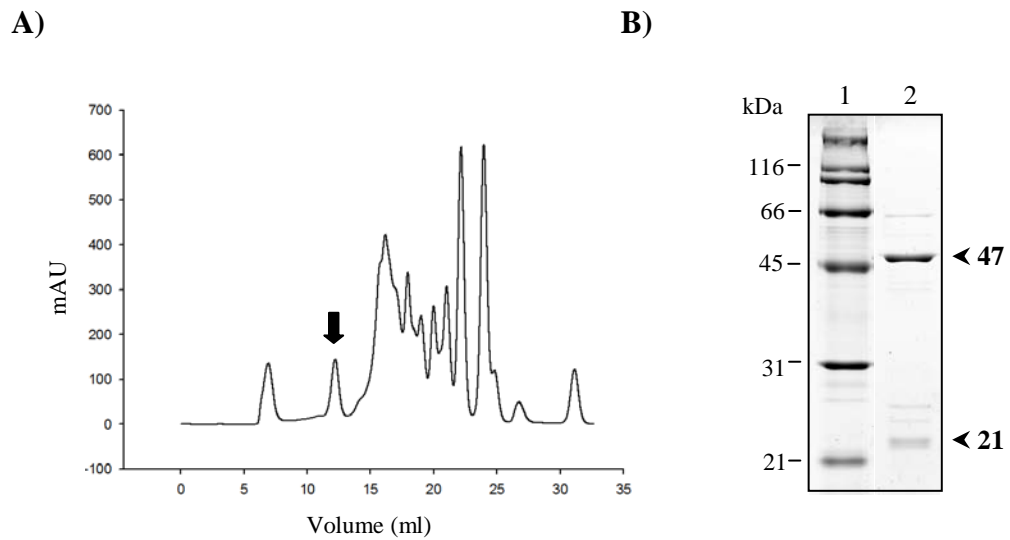


**Figure 7.2 Chromatogram and SDS-PAGE analysis of purified P193G mutant**

- A)** FPLC chromatogram from size-exclusion chromatography of purified P193G mutant toxin. The peak corresponding to the purified 65-kDa P193G mutant toxin is indicated.
- B)** Coomassie blue-stained SDS-polyacrylamide gel (12%) of the purified fraction of the P193G mutant toxin.

Lane 1 : Molecular mass standards

Lane 2 : The purified fraction of the 65-kDa P193G mutant toxin  
(comprising two non-covalently associated fragments of ca. 47  
and ca. 21 kDa)

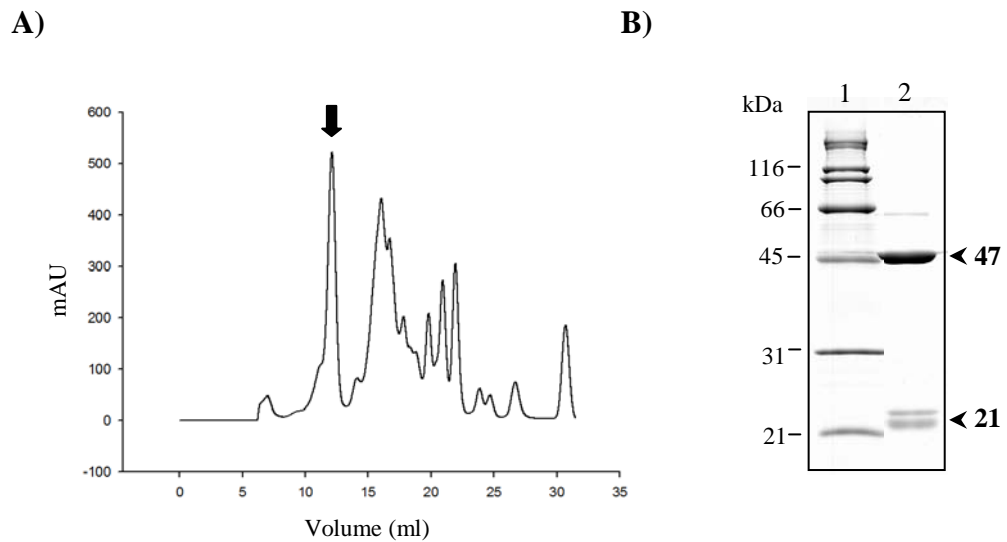


**Figure 7.3 Chromatogram and SDS-PAGE analysis of purified P194G mutant**

- A)** FPLC chromatogram from size-exclusion chromatography of purified P194G mutant toxin. The peak corresponding to the purified 65-kDa P194G mutant toxin is indicated.
- B)** Coomassie blue-stained SDS-polyacrylamide gel (12%) of the purified fraction of the P194G mutant toxin.

Lane 1 : Molecular mass standards

Lane 2 : The purified fraction of the 65-kDa P194G mutant toxin  
(comprising two non-covalently associated fragments of ca. 47  
and ca. 21 kDa)

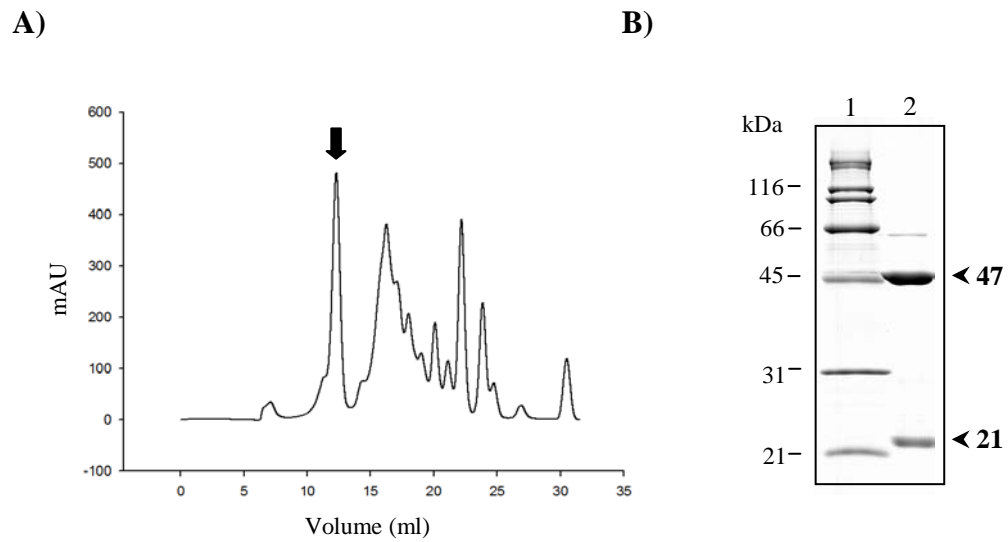


**Figure 7.4 Chromatogram and SDS-PAGE analysis of purified P196G mutant**

- A)** FPLC chromatogram from size-exclusion chromatography of purified P196G mutant toxin. The peak corresponding to the purified 65-kDa P196G mutant toxin is indicated.
- B)** Coomassie blue-stained SDS-polyacrylamide gel (12%) of the purified fraction of the P196G mutant toxin.

Lane 1 : Molecular mass standards

Lane 2 : The purified fraction of the 65-kDa P196G mutant toxin  
(comprising two non-covalently associated fragments of ca. 47  
and ca. 21 kDa)

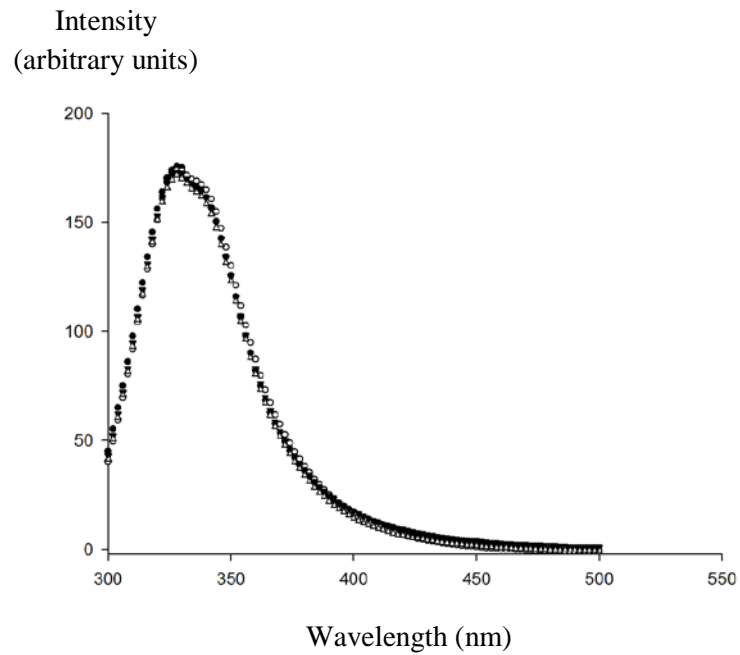


**Figure 7.5 Intrinsic fluorescence spectra of Cry4Aa and its glycine-substituted mutants**

The figure shows fluorescence spectrum of the 65-kDa FPLC-purified Cry4Aa toxin (●) in comparison with those of the mutant toxins, P193G (○), P194G (▼) and P196G (Δ).

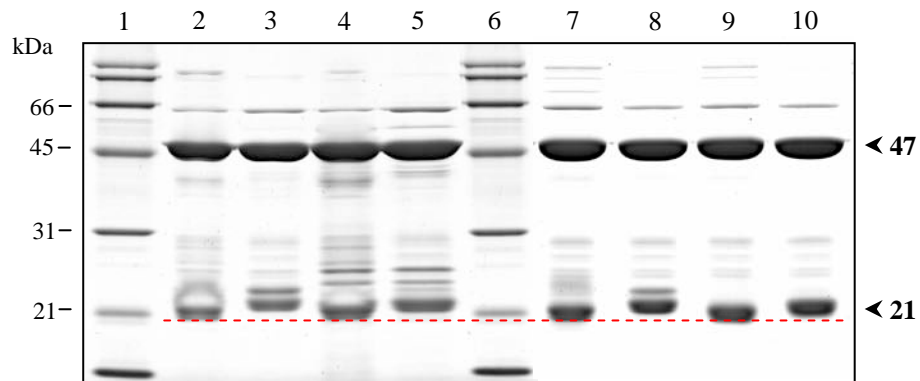


**Figure 7.6 Band-shift of Cry4Aa and its glycine-substituted mutants**

Coomassie blue-stained SDS-polyacrylamide gel (12%) shows mobility shift of the 21-kDa  $\alpha 1$ - $\alpha 5$  fragment of the trypsin-activated Cry4Aa and its mutant toxins.

Lanes 1 and 6 : Molecular mass standards

Lanes 2 and 3 : Trypsin-activated Cry4Aa toxin untreated and treated with DTT, respectively

Lanes 4 and 5 : Trypsin-activated P193G mutant untreated and treated with DTT, respectively

Lanes 7 and 8 : Trypsin-activated P194G mutant untreated and treated with DTT, respectively

Lanes 9 and 10 : Trypsin-activated P196G mutant untreated and treated with DTT, respectively

Toxin	% Calcein release					
	Cry4Aa (1.5 µg/ml)	Cry4Aa (3.0 µg/ml)	Cry4Aa (12.5 µg/ml)	Cry4Aa (25.0 µg/ml)	Cry4Aa (50.0 µg/ml)	Cry4Aa (75.0 µg/ml)
Mean	13.4	19.9	27.4	34.1	35.7	37.9
SD	4.9	5.6	1.9	11.8	5.3	1.1

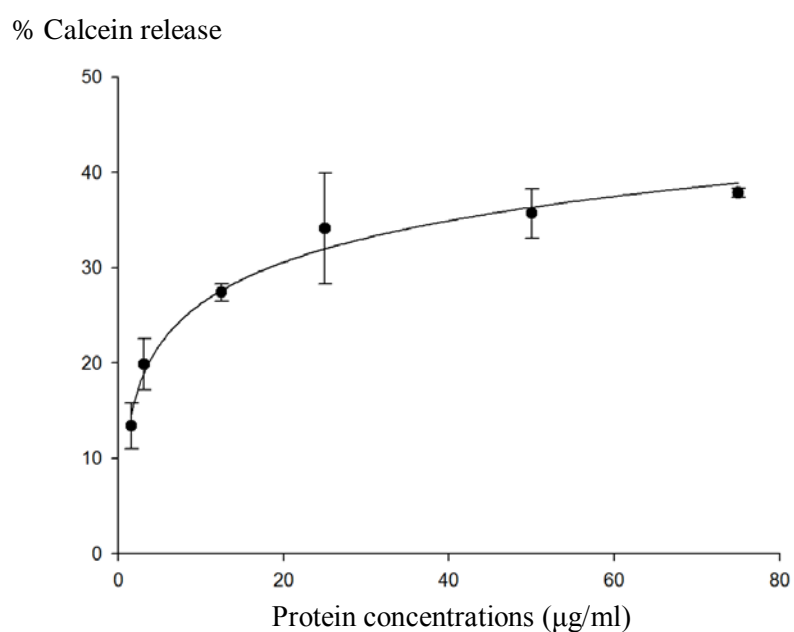


**Figure 7.7** Relative calcein release activity of Cry4Aa

The figure shows the relative calcein release activity of the 65-kDa purified Cry4Aa toxin at different concentrations. Error bars represent standard deviation (SD) from three experiments. Inserted table shows each value in details.

Toxin	% Calcein release				
	Na <sub>2</sub> CO <sub>3</sub>	Cry4Aa	P193G	P194G	P196G
Mean	0.1	20.0	24.0	18.1	19.8
SD	0.1	2.6	2.2	3.1	2.1

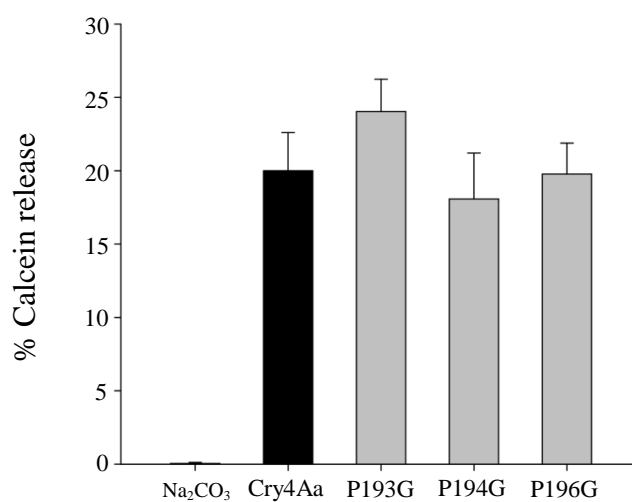


**Figure 7.8 Relative calcein release activity of Cry4Aa and its glycine-substituted mutants**

The figure shows the relative calcein release activity of the 65-kDa purified Cry4Aa and its mutant toxins (P193G, P194G and P196G) at the concentration of 3.0 µg/ml. The control sample was 50 mM carbonate buffer (pH 9.0). Error bars represent SD from three experiments. Inserted table shows each value in details.

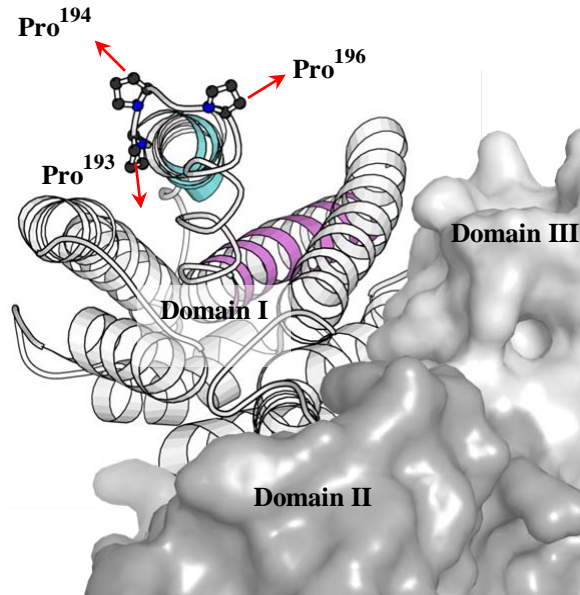


**Figure 7.9** Close-up view of part of Cry4Aa structure, illustrating side-chain direction of proline residues within the  $\alpha 4$ - $\alpha 5$  loop

The figure shows direction of side chain of individual proline residues (Pro<sup>193</sup>, Pro<sup>194</sup> and Pro<sup>196</sup>) within the  $\alpha 4$ - $\alpha 5$  loop of Cry4Aa (indicated as red arrows). The helical domain I is represented as schematic ribbon. Domains II and III are depicted as surface model.

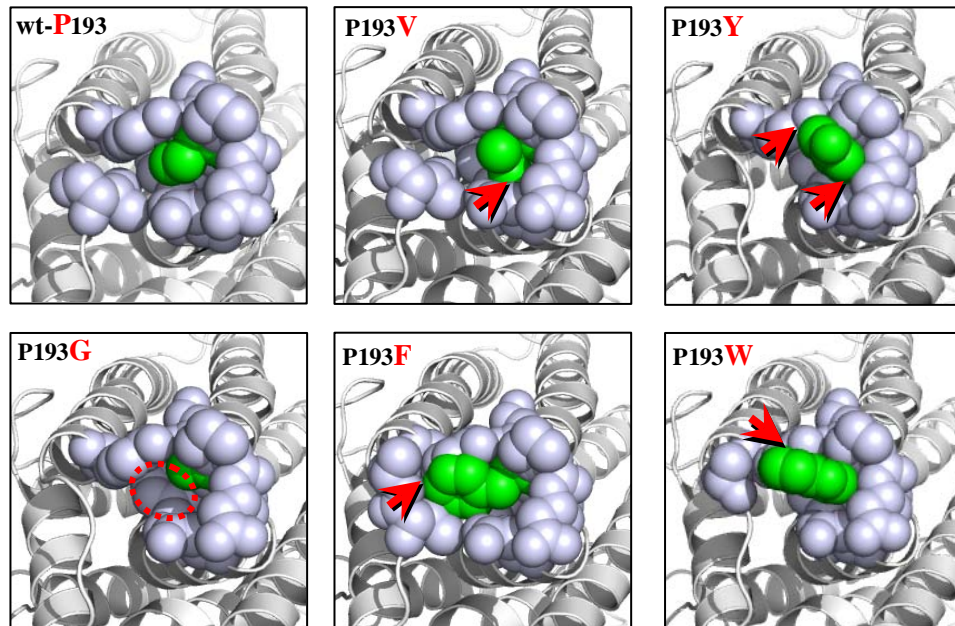


**Figure 7.10** Close-up views of part of Cry4Aa structure, illustrating interactions between residues at position 193 and their neighboring residues within 5 Å

The figure shows interactions between residues at the critical position 193 (shown as green space-filling model) and their neighboring residues within 5 Å (blue/white space-filling model). The cavity introduced inside the interaction is encircled. The red arrows indicate the side-chain overlap.

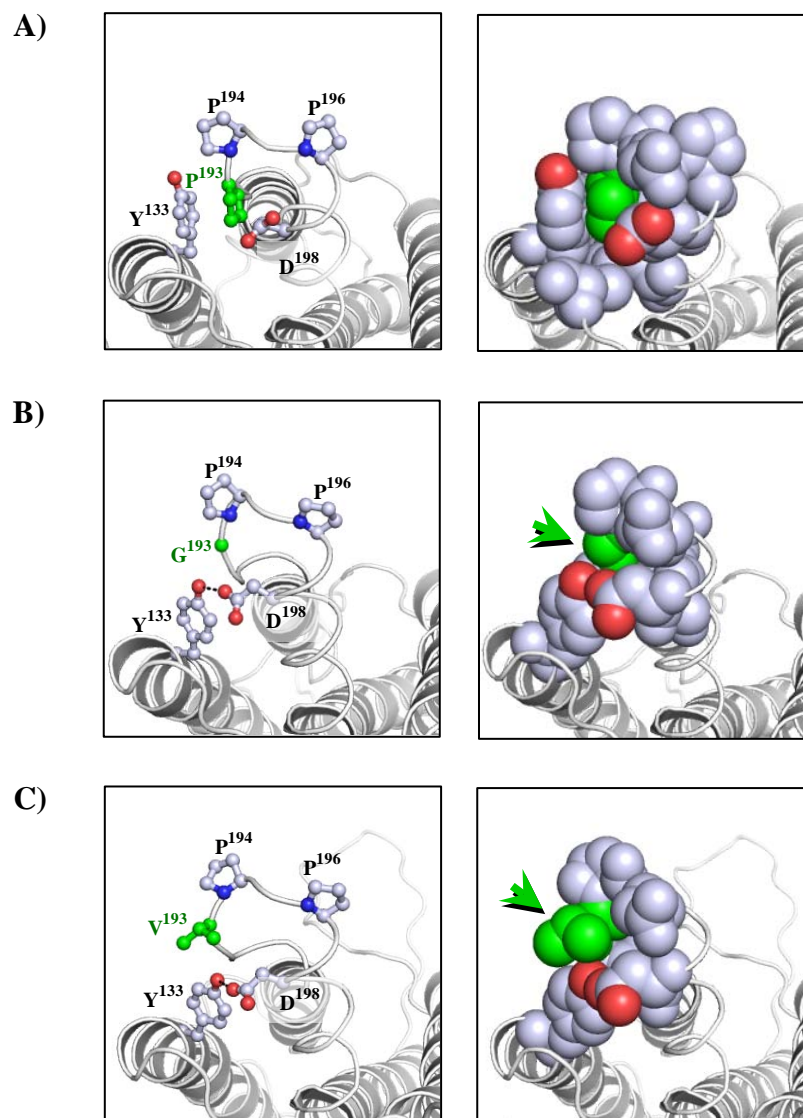


**Figure 7.11 Snapshots from MD simulations of Cry4Aa and its mutants, illustrating structural arrangement around position 193**

**A), B) and C)** Snapshots with different representations (left and right panels) from MD simulations of Cry4Aa wild type, P193G mutant and P193V mutant, respectively. Left panels show H-bond formed between Tyr<sup>133</sup> and Asp<sup>198</sup> specially found in mutant molecules (indicated as dash line). Right panels show amino acids at position 193 (green-colored) and their surrounding residues within 5 Å (bluewhite-colored). Green arrows indicate surface-exposed substituents (Gly<sup>193</sup> and Val<sup>193</sup>).

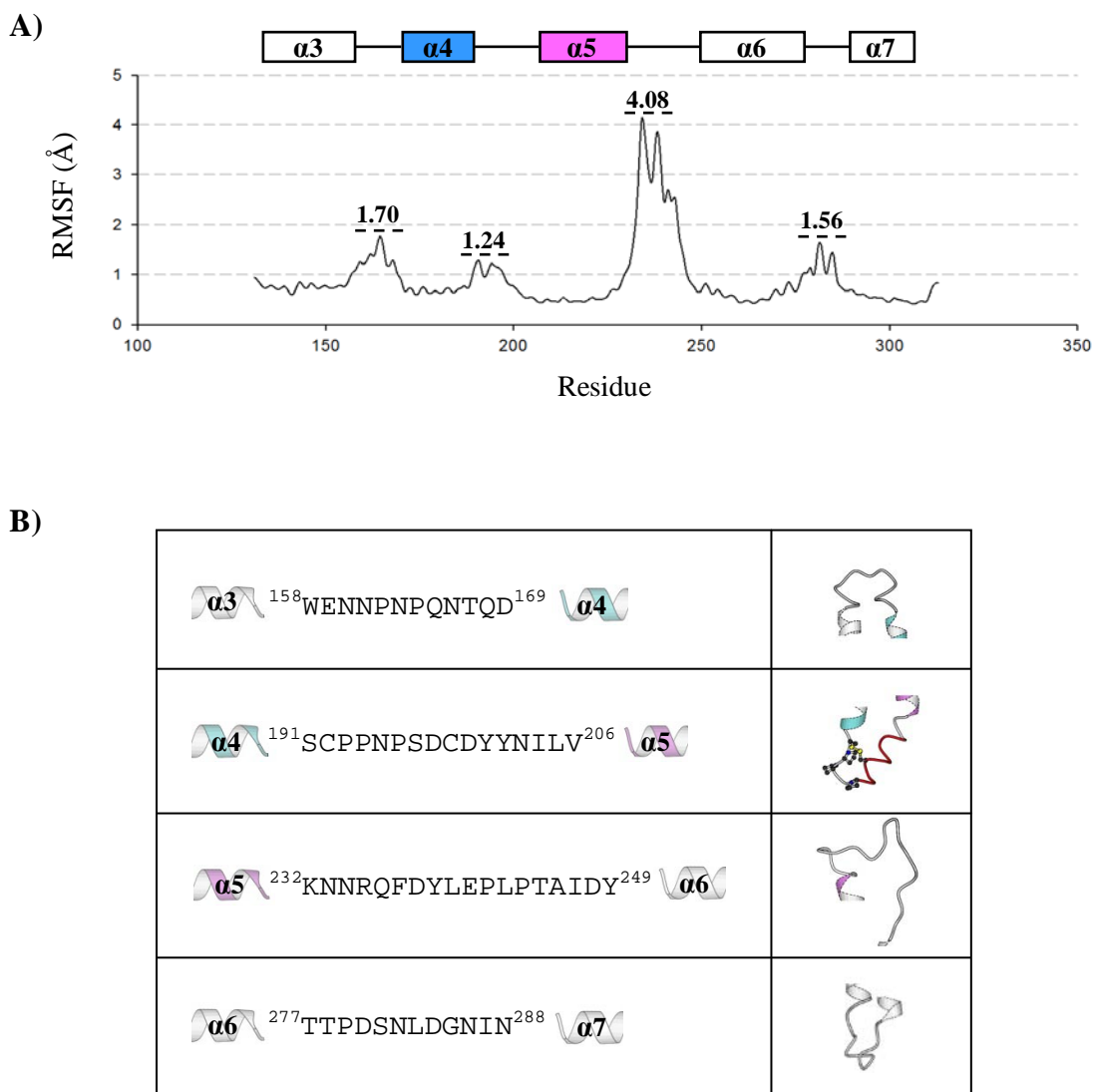


**Figure 7.12 RMSF value of Cry4Aa-domain I from MD simulations**

- A)**  $C_{\alpha}$ -RMSF value of Cry4Aa-domain I obtained from MD simulations.  $\alpha$ -helices are depicted above their corresponding RMSF profiles as rectangles. The highest RMSF values of each loop connecting two adjacent helices are indicated.
- B)** Sequences and corresponding conformations of Cry4Aa's domain-I loops. The three critical proline residues (Pro<sup>193</sup>, Pro<sup>194</sup> and Pro<sup>196</sup>) and Cys<sup>192</sup>-Cys<sup>199</sup> bond within  $\alpha 4$ - $\alpha 5$  loop are illustrated as ball-and-stick model. A short helical structure specially found within the  $\alpha 4$ - $\alpha 5$  loop is represented as red backbone trace.

## CHAPTER VIII

### DISCUSSION

#### 8.1 Effects of pH on formation of Cry4Aa protoxin inclusion

Similar to the native *B. thuringiensis* Cry4Aa toxin, its recombinant toxin was produced in *E. coli* as cytoplasmic crystalline inclusion (**Figure 4.1**). However, when distilled water was used as host cell-suspending solution in the process of Cry4Aa isolation (see details in section 3.2.11.1), a loss of the Cry4Aa inclusion was observed as the expressed Cry4Aa toxin was totally found in the soluble fraction of the cell lysate (**Figure 4.2A**). The measured pH value of distilled water used in the process was 5.5. As generally known, freshly distilled water is highly pure and thus will quickly dissolve CO<sub>2</sub> from the atmosphere to form a very dilute solution of carbonic acid with pH below 7.0 (usually pH 5.0-6.5, depending on the amount of CO<sub>2</sub> being dissolved). Without buffering capacity, *E. coli* host cells pre-suspended in distilled water showed an 1 pH-unit increase from pH 5.5 of cell suspension to pH 6.5 of cell lysate. Although it was shown that isolated Cry4Aa inclusion was solubilized in alkaline solution (16), it cannot be excluded that the Cry4Aa inclusion would be dissolved at pH 6.5 of the cell lysate in which several factors could possibly promote solubilization of the inclusion.

When a buffer solution with slightly acidic pH, *i.e.*, 100 mM KH<sub>2</sub>PO<sub>4</sub> (pH 5.0), was used instead of distilled water (see details in section 3.2.11.2), the expressed Cry4Aa inclusion was perfectly maintained (**Figure 4.2B**) as pH of the cell lysate was found to be 5.5. Clearly, the earlier observed loss of Cry4Aa inclusion was due to its solubility at the higher pH (6.5) of the cell lysate. When the obtained Cry4Aa inclusion was determined for alkaline solubility and proteolytic stability which are general characteristics of the Cry toxins, it was found to be solubilized in 50 mM Na<sub>2</sub>CO<sub>3</sub> buffer (pH 9.0) (**Figure 4.3A**) and cleaved by trypsin to yield ca. 47- and 21-kDa products (**Figure 4.3B**), thus indicating correct folding of the toxin.

Since it was shown here that a mildly acidic condition is sufficient to retain the inclusion form of Cry4Aa in *E. coli* cell lysate, it was further investigated whether the Cry4Aa inclusion could be derived from soluble form of the toxin by pH adjustment. Interestingly, the soluble Cry4Aa toxin in 50 mM Na<sub>2</sub>CO<sub>3</sub> buffer (pH 9.0) was found to precipitate when it was dialyzed against 100 mM KH<sub>2</sub>PO<sub>4</sub> buffer (pH 5.0). The resulting precipitated Cry4Aa inclusion exhibited typical biochemical characteristics and was typically toxic against *A. aegypti* mosquito larvae. The current evidence that crystalline inclusion formation of the Cry4Aa toxin is reversible depending on environmental pH suggested a participation of salt bridges in formation of the toxin inclusion, agreeing with the previous study which suggested that salt bridges are involved in stabilizing the crystal form of the Cry3Aa toxin (19).

## 8.2 Hydrophobic feature of proline-rich sequence located in Cry4Aa $\alpha$ 4- $\alpha$ 5 loop

The proline-rich sequence (Pro<sup>193</sup>Pro<sup>194</sup>\_Pro<sup>196</sup>), found within the  $\alpha$ 4- $\alpha$ 5 loop of Cry4Aa, was previously shown to be required for larvicidal activity of the toxin (16). As was widely shown that several protein-interaction domains, *e.g.*, Src homology 3 (SH3) domains which are found in a great variety of proteins of signaling pathways, bind to their proline-rich ligands *via* hydrophobic forces (85-88), hydrophobicity is considered as an essential feature of general proline-rich sequences. To investigate whether hydrophobic feature *per se* of the Cry4Aa proline-rich sequence is important for the toxin function, the three proline residues (Pro<sup>193</sup>, Pro<sup>194</sup> and Pro<sup>196</sup>) within the Cry4Aa  $\alpha$ 4- $\alpha$ 5 loop were replaced separately with valine, a hydrophobic residue with molecular mass similar to proline.

When the resulting valine-substituted mutants were tested for their toxicity against *A. aegypti* larvae, all were found to display a significant decrease in larvicidal activity (**Figure 5.8**), indicating that hydrophobic character of valine cannot compensate individual proline residue's character. Although the two aliphatic hydrophobic amino acids, proline and valine, are very similar in size, their structural features are rather different, *i.e.*, proline has a rigid planar structure while valine is an

alkyl chain. Thus, the results suggested an importance of the specific structure rather than hydrophobicity *per se* of individual critical proline residues for toxin function.

It should be noted that among single-valine substitutions of the three critical proline residues (Pro<sup>193</sup>, Pro<sup>194</sup> and Pro<sup>196</sup>), only P193V could disturb structural characteristic of the toxin as it showed an adverse effect on solubility of the toxin inclusion (**Figure 5.6**).

### **8.3 Structural importance of proline-rich sequence for Cry4Aa activity**

As was generally known, an aliphatic side chain of proline exceptionally forms a covalent bond with its N<sub>α</sub> atom, causing the peptide backbone N-terminally adjacent to the proline to be conformationally restrained. Accordingly, the three proline residues (Pro<sup>193</sup>, Pro<sup>194</sup> and Pro<sup>196</sup>) found within the Cry4Aa α4-α5 loop would make the loop to be highly rigid. Opposite to proline residue, glycine which has only single H atom as its side chain would allow the backbone to bend with a wide range of angles, thus providing high flexibility to the backbone. To determine whether loop rigidity provided by the proline-rich sequence is important for biological activity of the Cry4Aa toxin, the three proline residues were therefore substituted individually with glycine.

Bioassays of the resulting glycine-substituted mutants revealed that P194G and P196G mutations reduced toxicity against *A. aegypti* larvae of approximately 20-30% and P193G mutation caused a 50% loss of larvicidal activity (**Figure 5.16**). Compared with previously constructed P193A mutant which displayed a 30% reduction in toxicity (16), glycine substitutions which introduce more flexibility to the Cry4Aa α4-α5 loop had higher adverse effect on larvicidal activity. There is a related study showing that Pro<sup>345</sup> located near the turn between transmembrane helices 8 and 9 is important for membrane insertion of the diphtheria toxin as it may determine the conformation of the α8-α9 hairpin (89). In addition, another study suggested that connecting-loop rigidity which is likely determined by two loop proline residues (Pro<sup>43</sup> and Pro<sup>47</sup>) contributes to stability of the hairpin structure formed by two helices of the ATP synthase subunit *c* (90). According to a proposed mechanism of Cry toxin

action that the toxins insert into the membrane as a helical hairpin formed by helices 4 and 5 (7), the well-formed hairpin structure of these two helices is therefore required. Taken together, structural rigidity of the proline-rich sequence (Pro<sup>193</sup>Pro<sup>194</sup>\_Pro<sup>196</sup>), a determinant of the  $\alpha$ 4- $\alpha$ 5 loop stability, plays a crucial role in larvicidal activity of the Cry4Aa toxin, conceivably by supporting the  $\alpha$ 4- $\alpha$ 5 hairpin structure which is required for membrane insertion and pore formation. It is worth noting that structural analysis of the Cry4Aa trimeric structure, which was previously shown to be stable in solution *via* 10-ns MD simulations (66), revealed a close proximity among proline-rich sequences (Pro<sup>193</sup>Pro<sup>194</sup>\_Pro<sup>196</sup>) of individual protomers (**Figure 8.1**), thus suggesting a cooperation of these proline-rich clusters for promoting membrane insertion of the trimeric pre-pore formed by individual  $\alpha$ 4- $\alpha$ 5 hairpins.

Attempts were therefore made to examine an effect of loop flexibility introduced by glycine substitutions (P193G, P194G and P196G) on activity of the Cry4Aa toxin to permeabilize calcein-entrapped liposomes. The release of the encapsulated calcein by tested toxins was quantified as the relative increase in fluorescence de-quenching intensity. As can be seen that, similar to the wild-type toxin, all three glycine-substituted mutants were found to exhibit a high value of calcein release activity (**Figure 7.8**). It should be noted that an estimated concentration of the total released calcein upon addition of Triton X-100 (causing 100% calcein leakage) was  $\sim 0.15 \mu\text{M}$  that is much lower than a critical concentration for self-quenching ( $\sim 20 \mu\text{M}$ ) (91-92). This indicated that the similarity in release activity observed between the wild type and the three mutants is least likely to be resulted from self-quenching of the released calcein. Compared to the result from bioassays that the three glycine-substituted mutants displayed a reduction in mosquito-larvicidal activity, the high membrane-perturbing activity of these mutants observed from calcein release assay could be due to a lower integrity of the artificial biomembrane (liposomes) than that of the larval gut membrane.

It is interesting to note that, similar to valine-substituted mutations, glycine substitution of only Pro<sup>193</sup> (P193G) interfered with solubility of the toxin inclusion (**Figure 5.14**). A possible explanation for this remarkable mutational effect is mentioned in **section 8.4**.

#### 8.4 Additional importance of Pro<sup>193</sup> for structural arrangement of Cry4Aa toxin molecule

Noticed that among amino-acid substitutions of the three proline residues (Pro<sup>193</sup>, Pro<sup>194</sup> and Pro<sup>196</sup>) within the Cry4Aa  $\alpha$ 4- $\alpha$ 5 loop, those of Pro<sup>193</sup> (P193V and P193G) had the most adverse effect on larvicidal activity of the toxin (**Figures 5.8 and 5.16**). Structural analysis of the Cry4Aa toxin indicated that the Pro<sup>193</sup> is located in the way that its pyrrolidine ring is closely parallel to benzene ring of Tyr<sup>133</sup>, suggesting an interaction between these two amino-acid residues. Such conceivable interaction was speculated to sustain a functional conformation of the Cry4Aa toxin. However, replacements of the Pro<sup>193</sup> with aromatic amino acids which may form a  $\pi$ - $\pi$  interaction with Tyr<sup>133</sup> resulted in a drastic loss of toxin activity (**Figure 5.24**), indicating that aromatic ring cannot compensate the Pro<sup>193</sup>-pyrrolidine ring. Moreover, it was found that all these substitutions adversely affect toxin solubility (**Figure 5.23**), thus implying their interference with structural characteristic of the toxin.

It was also speculated that substitutions of Pro<sup>193</sup> which is located next to Cys<sup>192</sup> may interfere with Cys<sup>192</sup>-Cys<sup>199</sup> bond formation, thus additionally affecting  $\alpha$ 4- $\alpha$ 5 loop stability and hence toxicity. To test this notion, the soluble form of P193G mutant was selected for examining the existence of the disulfide bond in comparison with the wild type and two other mutants (P194G and P196G). Like that of the wild type, the 21-kDa fragment (corresponding to the first five helices of Cry4Aa-domain I) of P193G, as well as those of P194G and P196G, ran differently in the absence and presence of DTT (**Figure 7.6**), indicating the existence of the Cys<sup>192</sup>-Cys<sup>199</sup> bond within all the toxin molecules. This result revealed that P193G mutation had no effect on formation of the Cys<sup>192</sup>-Cys<sup>199</sup> bond although it showed a large influence on toxin activity. Further structural characterization using intrinsic fluorescence revealed that the P193G mutant's soluble form also retained the same overall tertiary structure as the wild type and the two other mutants (P194G and P196G) since all of them showed the identical fluorescence spectral profiles (**Figure 7.5**).

Consistent with mortality result, data from alkaline solubilization showed that single-substitutions of Pro<sup>193</sup> (P193V, P193G, P193F, P193W and P193Y) caused a severe defect in solubility of the toxin inclusion while those of Pro<sup>194</sup> and Pro<sup>196</sup> retained the high level of solubility. Since a deficiency in alkaline solubility implies an

insoluble aggregated form of the toxin resulted from protein misfolding, the great influence of Pro<sup>193</sup> on inclusion solubility suggested an added role of the Pro<sup>193</sup> in structural arrangement of the toxin molecule, apart from providing a structural rigidity.

Interestingly, additional structural analysis of the Cry4Aa toxin revealed that side chain of the Pro<sup>193</sup> points inwards into the toxin molecule whereas those of Pro<sup>194</sup> and Pro<sup>196</sup> point outwards (**Figure 7.9**), suggesting the high possibility that mutations of Pro<sup>193</sup> would affect structural arrangement and hence function of the toxin. Further structural analysis *via* MD simulations showed that amino-acid replacements at the position 193 caused a great change in structural arrangement around this position. Whereas Pro<sup>193</sup> of the wild-type toxin was surrounded by hydrophobic environment including benzene ring of Tyr<sup>133</sup>, the substituents (Gly<sup>193</sup> and Val<sup>193</sup>) were found to be surface-exposed as the Tyr<sup>133</sup> remarkably moved to form H-bond with side chain of Asp<sup>198</sup> (**Figure 7.11**). Moreover, dissimilarity in conformational dynamics of Tyr<sup>133</sup> was observed between P193G and P193V mutants, *i.e.*, while P193V-Tyr<sup>133</sup> permanently shifted from Val<sup>193</sup> to form H-bond with Asp<sup>198</sup>, P193G-Tyr<sup>133</sup> was found to fluctuate between Gly<sup>193</sup> and Asp<sup>198</sup> (data not shown). As mentioned earlier that P193G substitution caused ~50% decrease in solubility of the toxin inclusion whereas P193V mutation resulted in a nearly complete loss of inclusion solubility (**Figures 5.14** and **5.6**, respectively), equal chances of the P193G-Tyr<sup>133</sup> to occur at the two positions might be an explanation for the two forms (alkali-soluble and insoluble-aggregated inclusions) of the P193G protoxin inclusion. Altogether, the well-packing of Pro<sup>193</sup> and its hydrophobic surroundings is likely a requirement for proper arrangement of the Cry4Aa toxin structure, thus leading the Pro<sup>193</sup> to be the most critical residue among proline residues within the  $\alpha$ 4- $\alpha$ 5 loop.

## 8.5 Structure-stability relationships of the long Cry4Aa $\alpha$ 4- $\alpha$ 5 loop

The  $\alpha$ 4- $\alpha$ 5 loop of the Cry4Aa toxin is extraordinarily long (16 residues) when compared with those of other known Cry toxins (5-9 residues) (**Figure 1.1B**). Structural rigidity of the proline-rich region (Pro<sup>193</sup>Pro<sup>194</sup>\_Pro<sup>196</sup>) which is currently shown to be required for the Cry4Aa toxicity may serve as a determinant for stabilizing such long loop. This notion became more possible as two other structural

features of the loop were also found, *i.e.*, a disulfide bond (Cys<sup>192</sup>-Cys<sup>199</sup>) and a short helical structure (Pro<sup>196</sup> to Ile<sup>204</sup>) (**Figure 1.1A**), and the disulfide bond was previously shown to be essential for larvicidal activity of the Cry4Aa toxin (16).

Although conformational rigidity provided by the three proline residues (Pro<sup>193</sup>, Pro<sup>194</sup> and Pro<sup>196</sup>) was shown to be essential for the toxin function, further analysis *via* proline-scanning mutagenesis of the loop residues (Ser<sup>191</sup> to Asp<sup>200</sup>) revealed that almost all proline-substituted mutants exhibited a reduction in larvicidal activity (**Figure 6.13**). Moreover, it was found that all the proline-substituted mutations, except for N195P and S197P, adversely affected solubility of the toxin inclusion (**Figures 6.10-6.11**). These results suggested that proline residues are only acceptable at particular positions in the Cry4Aa  $\alpha$ 4- $\alpha$ 5 loop since existence of proline at wrong positions may disturb another structural features (the Cys<sup>192</sup>-Cys<sup>199</sup> bond and the  $\alpha$ -helical structure) of the loop, thus causing a further consequence on both loop stability and overall toxin structure as can be observed through a reduction in toxicity and alkaline solubility, respectively.

MD simulations of the Cry4Aa wild-type structure revealed that the  $\alpha$ 4- $\alpha$ 5 loop has an RMSF value of 1.24 Å which is lower than those of the remaining loops within the pore-forming domain (**Figure 7.12A**). This data is consistent with that reported from previous simulations of the Cry4Aa trimer that the  $\alpha$ 4- $\alpha$ 5 loop showed the lowest RMSF value among the domain-I loops (66). As RMSF values indicate the intensity of fluctuation for each amino-acid residue, such RMSF data implied a substantial rigidity of the  $\alpha$ 4- $\alpha$ 5 loop over the other loops with a similar or even a shorter length ( $\alpha$ 3- $\alpha$ 4 loop: 12 residues;  $\alpha$ 5- $\alpha$ 6 loop: 18 residues;  $\alpha$ 6- $\alpha$ 7 loop: 12 residues) (**Figure 7.12B**). Note that the  $\alpha$ 5- $\alpha$ 6 loop which is only 2-residue longer than the  $\alpha$ 4- $\alpha$ 5 loop showed a greater RMSF value of 4.08 Å, indicating that this loop is incredibly unstable. Moreover, the coordinates of part of this  $\alpha$ 5- $\alpha$ 6 loop (Arg<sup>235</sup> to Pro<sup>244</sup>) were missing from the original X-ray crystal structure of the Cry4Aa toxin (PDB ID: 2C9K), thus supporting a great flexibility of this extra long loop. Compared with such flexible  $\alpha$ 5- $\alpha$ 6 loop, the supreme stability of the Cry4Aa  $\alpha$ 4- $\alpha$ 5 loop is likely related to its unique structural features, *i.e.*, the proline-rich sequence, the disulfide bond and the short  $\alpha$ -helical structure.

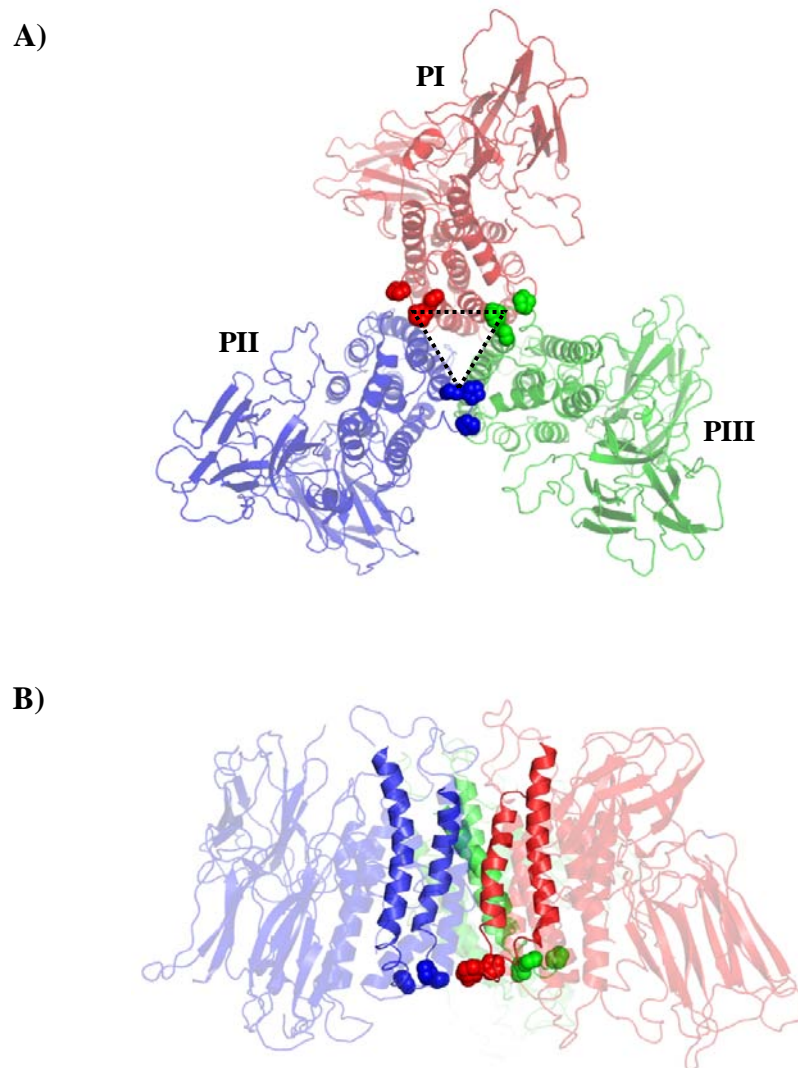


**Figure 8.1 Two different views of Cry4Aa trimeric structure, illustrating position of loop proline clusters within the molecule**

**A)** Bottom view of Cry4Aa trimer. Proline-rich cluster (Pro<sup>193</sup>Pro<sup>194</sup>\_Pro<sup>196</sup>) within  $\alpha$ 4- $\alpha$ 5 loop of individual protomers (PI, PII and PIII) is depicted as vdW (van der Waals) spheres. The putative pre-pore formed by the three protomers is indicated with dash-line triangle.

**B)** Side view of Cry4Aa trimer. The proline-rich clusters are shown as vdW spheres.  $\alpha$ 4- $\alpha$ 5 hairpins of individual protomers are depicted as opaque ribbons.

## CHAPTER IX

### CONCLUSIONS

1. It was shown that crystalline inclusion of the Cry4Aa toxin can be obtained effectively from host-cell lysate or soluble form of the toxin by pH adjustment. pH dependence of the Cry4Aa crystalline inclusion formation suggested an involvement of salt bridges in the toxin crystal formation.

2. Valine substitutions of individual proline residues (Pro<sup>193</sup>, Pro<sup>194</sup> and Pro<sup>196</sup>) were performed to investigate whether hydrophobicity *per se* of the proline-rich structure (Pro<sup>193</sup>Pro<sup>194</sup>\_Pro<sup>196</sup>) found within the Cry4Aa  $\alpha$ 4- $\alpha$ 5 loop is important for the toxin function. Bioassays revealed that all proline-to-valine substitutions caused a significant decrease in toxicity against *A. aegypti* larvae, suggesting that specific structure, not hydrophobic feature *per se*, of the three proline residues is crucial for the toxin bioactivity.

3. Glycine substitutions of the three proline residues were further performed to investigate whether structural rigidity of the Cry4Aa  $\alpha$ 4- $\alpha$ 5 loop comprising the proline-rich structure (Pro<sup>193</sup>Pro<sup>194</sup>\_Pro<sup>196</sup>) is essential for larvicidal activity of the toxin. It was found that all proline-to-glycine mutants, especially P193G, displayed a reduction in toxicity, indicating the importance of loop rigidity provided by the three proline residues for the toxin function.

4. Among amino-acid replacements of proline residues within the Cry4Aa  $\alpha$ 4- $\alpha$ 5 loop, those of Pro<sup>193</sup> had the most adverse effect on both larvicidal activity and inclusion solubility of the toxin. It was revealed that only the most critical proline residue—Pro<sup>193</sup>, whose side chain points inwards into the toxin molecule, is located inside a well-packed core made up of several hydrophobic residues. It was shown that mutations of this Pro<sup>193</sup> could disrupt this hydrophobic packing and thus prevent the correct folding of the toxin molecule. Thereby, Pro<sup>193</sup> could possibly play another role in structural arrangement of the Cry4Aa toxin molecule, apart from providing the  $\alpha$ 4- $\alpha$ 5 loop rigidity.

5. Unique structural features of the long Cry4Aa  $\alpha$ 4- $\alpha$ 5 loop, *i.e.*, a proline-rich sequence (Pro<sup>193</sup>Pro<sup>194</sup>Pro<sup>196</sup>), a Cys<sup>192</sup>-Cys<sup>199</sup> bond and a short  $\alpha$ -helical structure (Pro<sup>196</sup> to Ile<sup>204</sup>), are likely to be determinants for the loop stability which is required for toxin activity.

Additional experiments are still required to verify definitively the functional role of the proline-rich sequence, particularly in the steps of membrane insertion and pore formation.

## REFERENCES

1. Federici BA, Park HW, Bideshi DK. Overview of the basic biology of *Bacillus thuringiensis* with emphasis on genetic engineering of bacterial larvicides for mosquito control. *Open Toxinol J.* 2010;3:83-100.
2. Poncet S, Delécluse A, Klier A, Rapoport G. Evaluation of synergistic interactions among the CryIVA, CryIVB, and CryIVD toxic components of *B. thuringiensis* subsp. *israelensis* crystals. *J Invertebr Pathol.* 1995;66(2):131-135.
3. Schnepf E, Crickmore N, Van Rie J, Lereclus D, Baum J, Feitelson J, *et al.* *Bacillus thuringiensis* and its pesticidal crystal proteins. *Microbiol Mol Biol Rev.* 1998;62(3):775-806.
4. Knowles BH. Mechanism of action of *Bacillus thuringiensis* insecticidal  $\delta$ -endotoxins. In: Evans PD, editor. *Adv Insect Physiol*: Academic Press; 1994. p. 275-308.
5. Knowles BH, Ellar DJ. Colloid-osmotic lysis is a general feature of the mechanism of action of *Bacillus thuringiensis*  $\delta$ -endotoxins with different insect specificity. *Biochim Biophys Acta.* 1987;924(3):509-518.
6. Boonserm P, Mo M, Angsuthanasombat C, Lescar J. Structure of the functional form of the mosquito larvicidal Cry4Aa toxin from *Bacillus thuringiensis* at a 2.8-angstrom resolution. *J Bacteriol.* 2006;188(9):3391-3401.
7. Gazit E, Rocca PL, Sansom MSP, Shai Y. The structure and organization within the membrane of the helices composing the pore-forming domain of *Bacillus thuringiensis*  $\delta$ -endotoxin are consistent with an “umbrella-like” structure of the pore. *Proc Natl Acad Sci USA.* 1998;95(21):12289-12294.

8. Schwartz J-L, Juteau M, Grochulski P, Cygler M, Préfontaine G, Brousseau R, *et al.* Restriction of intramolecular movements within the Cry1Aa toxin molecule of *Bacillus thuringiensis* through disulfide bond engineering. *FEBS Lett.* 1997;410(2-3):397-402.
9. Masson L, Tabashnik BE, Liu Y-B, Brousseau R, Schwartz J-L. Helix 4 of the *Bacillus thuringiensis* Cry1Aa toxin lines the lumen of the ion channel. *J Biol Chem.* 1999;274(45):31996-32000.
10. Sramala I, Leetachewa S, Krittanai C, Katzenmeier G, Panyim S, Angsuthanasombat C. Charged residue screening in helix 4 of the *Bacillus thuringiensis* Cry4B toxin reveals one critical residue for larvicidal activity. *J Biochem Mol Biol Biophys.* 2001;5(3):219-225.
11. Nuñez-Valdez ME, Sánchez J, Lina L, Güereca L, Bravo A. Structural and functional studies of  $\alpha$ -helix 5 region from *Bacillus thuringiensis* Cry1Ab  $\delta$ -endotoxin. *Biochim Biophys Acta.* 2001;1546(1):122-131.
12. Likitvivatanavong S, Katzenmeier G, Angsuthanasombat C. Asn<sup>183</sup> in  $\alpha$ 5 is essential for oligomerisation and toxicity of the *Bacillus thuringiensis* Cry4Ba toxin. *Arch Biochem Biophys.* 2006;445(1):46-55.
13. Gerber D, Shai Y. Insertion and organization with membranes of the  $\delta$ -endotoxin pore-forming domain, helix 4-loop-helix 5, and inhibition of its activity by a mutant helix 4 peptide. *J Biol Chem.* 2000;275(31):23602-23607.
14. Kanintronkul Y, Sramala I, Katzenmeier G, Panyim S, Angsuthanasombat C. Specific mutations within the  $\alpha$ 4- $\alpha$ 5 loop of the *Bacillus thuringiensis* Cry4B toxin reveal a crucial role for Asn-166 and Tyr-170. *Mol Biotechnol.* 2003;24(1):11-19.
15. Pornwiroon W, Katzenmeier G, Panyim S, Angsuthanasombat C. Aromaticity of Tyr-202 in the  $\alpha$ 4- $\alpha$ 5 loop is essential for toxicity of the *Bacillus thuringiensis* Cry4A toxin. *J Biochem Mol Biol.* 2004;37(3):292-297.

16. Tapaneeyakorn S, Pornwiroon W, Katzenmeier G, Angsuthanasombat C. Structural requirements of the unique disulphide bond and the proline-rich motif with the  $\alpha$ 4- $\alpha$ 5 loop for larvicidal activity of the *Bacillus thuringiensis* Cry4Aa  $\delta$ -endotoxin. *Biochem Biophys Res Commun*. 2005;330(2):519-525.
17. Grochulski P, Masson L, Borisova S, Pusztai-Carey M, Schwartz J-L, Brousseau R, *et al.* *Bacillus thuringiensis* CryIA(a) insecticidal toxin: crystal structure and channel formation. *J Mol Biol*. 1995;254(3):447-464.
18. Morse RJ, Yamamoto T, Stroud RM. Structure of Cry2Aa suggests an unexpected receptor binding epitope. *Structure*. 2001;9(5):409-417.
19. Li J, Carroll J, Ellar DJ. Crystal structure of insecticidal  $\delta$ -endotoxin from *Bacillus thuringiensis* at 2.5 Å resolution. *Nature*. 1991;353(6347):815-821.
20. Boonserm P, Davis P, Ellar DJ, Li J. Crystal structure of the mosquito-larvicidal toxin Cry4Ba and its biological implications. *J Mol Biol*. 2005;348(2):363-382.
21. Höfte H, Whiteley HR. Insecticidal crystal proteins of *Bacillus thuringiensis*. *Microbiol Rev*. 1989;53(2):242-255.
22. Aronson AI, Shai Y. Why *Bacillus thuringiensis* insecticidal toxins are so effective: unique features of their mode of action. *FEMS Microbiol Lett*. 2001;195(1):1-8.
23. Crickmore N, Zeigler DR, Feitelson J, Schnepf E, Van Rie J, Lereclus D, *et al.* Revision of the nomenclature for the *Bacillus thuringiensis* pesticidal crystal proteins. *Microbiol Mol Biol Rev*. 1998;62(3):807-813.
24. Von Tersch MA, Slatin SL, Kulesza CA, English LH. Membrane-permeabilizing activities of *Bacillus thuringiensis* coleopteran-active toxin CryIIIB2 and CryIIIB2 domain I peptide. *Appl Environ Microbiol*. 1994;60(10):3711-3717.
25. Kumar AS, Aronson AI. Analysis of mutations in the pore-forming region essential for insecticidal activity of a *Bacillus thuringiensis*  $\delta$ -endotoxin. *J Bacteriol*. 1999;181(19):6103-6107.

26. Tigue NJ, Jacoby J, Ellar DJ. The  $\alpha$ -helix 4 residue, Asn135, is involved in the oligomerization of Cry1Ac1 and Cry1Ab5 *Bacillus thuringiensis* toxins. *Appl Environ Microbiol.* 2001;67(12):5715-5720.
27. Alcantara EP, Alzate O, Lee MK, Curtiss A, Dean DH. Role of  $\alpha$ -helix seven of *Bacillus thuringiensis* Cry1Ab  $\delta$ -endotoxin in membrane insertion, structural stability, and ion channel activity. *Biochemistry.* 2001;40(8):2540-2547.
28. Widner WR, Whiteley HR. Location of the dipteran specificity region in a lepidopteran-dipteran crystal protein from *Bacillus thuringiensis*. *J Bacteriol.* 1990;172(6):2826-2832.
29. Lu H, Rajamohan F, Dean DH. Identification of amino acid residues of *Bacillus thuringiensis*  $\delta$ -endotoxin CryIAa associated with membrane binding and toxicity to *Bombyx mori*. *J Bacteriol.* 1994;176(17):5554-5559.
30. Smith GP, Ellar DJ. Mutagenesis of two surface-exposed loops of the *Bacillus thuringiensis* CryIC  $\delta$ -endotoxin affects insecticidal specificity. *Biochem J.* 1994;302(Pt 2):611-616.
31. Rajamohan F, Alcantara E, Lee MK, Chen XJ, Curtiss A, Dean DH. Single amino acid changes in domain II of *Bacillus thuringiensis* CryIAb  $\delta$ -endotoxin affect irreversible binding to *Manduca sexta* midgut membrane vesicles. *J Bacteriol.* 1995;177(9):2276-2282.
32. Rajamohan F, Cotrill JA, Gould F, Dean DH. Role of domain II, loop 2 residues of *Bacillus thuringiensis* CryIAb  $\delta$ -endotoxin in reversible and irreversible binding to *Manduca sexta* and *Heliothis virescens*. *J Biol Chem.* 1996;271(5):2390-2396.
33. Rajamohan F, Hussain SR, Cotrill JA, Gould F, Dean DH. Mutations at domain II, loop 3, of *Bacillus thuringiensis* CryIAa and CryIAb  $\delta$ -endotoxins suggest loop 3 is involved in initial binding to lepidopteran midguts. *J Biol Chem.* 1996;271(41):25220-25226.
34. Lee MK, Young BA, Dean DH. Domain III exchanges of *Bacillus thuringiensis* CryIA toxins affect binding to different gypsy moth midgut receptors. *Biochem Biophys Res Commun.* 1995;216(1):306-312.

35. de Maagd RA, Kwa MS, van der Klei H, Yamamoto T, Schipper B, Vlak JM, *et al.* Domain III substitution in *Bacillus thuringiensis* delta-endotoxin CryIA(b) results in superior toxicity for *Spodoptera exigua* and altered membrane protein recognition. *Appl Environ Microbiol.* 1996;62(5):1537-1543.
36. de Maagd RA, Bakker PL, Masson L, Adang MJ, Sangadala S, Stiekema W, *et al.* Domain III of the *Bacillus thuringiensis* delta-endotoxin Cry1Ac is involved in binding to *Manduca sexta* brush border membranes and to its purified aminopeptidase N. *Mol Microbiol.* 1999;31(2):463-471.
37. Koller CN, Bauer LS, Hollingworth RM. Characterization of the pH-mediated solubility of *Bacillus thuringiensis* var. *san diego* native  $\delta$ -endotoxin crystals. *Biochem Biophys Res Commun.* 1992;184(2):692-699.
38. Aronson AI, Beckman W, Dunn P. *Bacillus thuringiensis* and related insect pathogens. *Microbiol Rev.* 1986;50(1):1-24.
39. Choma CT, Surewicz WK, Carey PR, Pozsgay M, Raynor T, Kaplan H. Unusual proteolysis of the protoxin and toxin from *Bacillus thuringiensis*. *Eur J Biochem.* 1990;189(3):523-527.
40. Höfte H, de Greve H, Seurinck J, Jansens S, Mahillon J, Ampe C, *et al.* Structural and functional analysis of a cloned delta endotoxin of *Bacillus thuringiensis* berliner 1715. *Eur J Biochem.* 1986;161(2):273-280.
41. Boonserm P, Pornwiroon W, Katzenmeier G, Panyim S, Angsuthanasombat C. Optimised expression in *Escherichia coli* and purification of the functional form of the *Bacillus thuringiensis* Cry4Aa  $\delta$ -endotoxin. *Protein Expr Purif.* 2004;35(2):397-403.
42. Hofmann C, Lüthy P, Hütter R, Pliska V. Binding of the delta endotoxin from *Bacillus thuringiensis* to brush-border membrane vesicles of the cabbage butterfly (*Pieris brassicae*). *Eur J Biochem.* 1988;173(1):85-91.
43. McNall RJ, Adang MJ. Identification of novel *Bacillus thuringiensis* Cry1Ac binding proteins in *Manduca sexta* midgut through proteomic analysis. *Insect Biochem Mol Biol.* 2003;33(10):999-1010.

44. Jurat-Fuentes JL, Adang MJ. Characterization of a Cry1Ac-receptor alkaline phosphatase in susceptible and resistant *Heliothis virescens* larvae. *Eur J Biochem.* 2004;271(15):3127-3135.
45. Fernandez LE, Aimanova KG, Gill SS, Bravo A, Soberón M. A GPI-anchored alkaline phosphatase is a functional midgut receptor of Cry11Aa toxin in *Aedes aegypti* larvae. *Biochem J.* 2006;394(Pt 1):77-84.
46. Dechklar M, Tiewisiri K, Angsuthanasombat C, Pootanakit K. Functional expression in insect cells of glycosylphosphatidylinositol-linked alkaline phosphatase from *Aedes aegypti* larval midgut: a *Bacillus thuringiensis* Cry4Ba toxin receptor. *Insect Biochem Mol Biol.* 2011;41(3):159-166.
47. Masson L, Lu Y-J, Mazza A, Brousseau R, Adang MJ. The CryIA(c) receptor purified from *Manduca sexta* displays multiple specificities. *J Biol Chem.* 1995;270(35):20309-20315.
48. Yaoi K, Kadotani T, Kuwana H, Shinkawa A, Takahashi T, Iwahana H, *et al.* Aminopeptidase N from *Bombyx mori* as a candidate for the receptor of *Bacillus thuringiensis* Cry1Aa toxin. *Eur J Biochem.* 1997;246(3):652-657.
49. Luo K, Sangadala S, Masson L, Mazza A, Brousseau R, Adang MJ. The *Heliothis virescens* 170 kDa aminopeptidase functions as "Receptor A" by mediating specific *Bacillus thuringiensis* Cry1A  $\delta$ -endotoxin binding and pore formation. *Insect Biochem Mol Biol.* 1997;27(8-9):735-743.
50. Zhang R, Hua G, Andacht TM, Adang MJ. A 106-kDa aminopeptidase is a putative receptor for *Bacillus thuringiensis* Cry11Ba toxin in the mosquito *Anopheles gambiae*. *Biochemistry.* 2008;47(43):11263-11272.
51. Nagamatsu Y, Toda S, Yamaguchi F, Ogo M, Kogure M, Nakamura M, *et al.* Identification of *Bombyx mori* midgut receptor for *Bacillus thuringiensis* insecticidal CryIA(a) toxin. *Biosci Biotechnol Biochem.* 1998;62(4):718-726.
52. Nagamatsu Y, Koike T, Sasaki K, Yoshimoto A, Furukawa Y. The cadherin-like protein is essential to specificity determination and cytotoxic action of the *Bacillus thuringiensis* insecticidal CryIAa toxin. *FEBS Lett.* 1999;460(2):385-390.

53. Fabrick J, Oppert C, Lorenzen MD, Morris K, Oppert B, Jurat-Fuentes JL. A novel *Tenebrio molitor* cadherin is a functional receptor for *Bacillus thuringiensis* Cry3Aa toxin. *J Biol Chem*. 2009;284(27):18401-18410.
54. Contreras E, Schoppmeier M, Real MD, Rausell C. Sodium solute symporter and cadherin proteins act as *Bacillus thuringiensis* Cry3Ba toxin functional receptors in *Tribolium castaneum*. *J Biol Chem*. 2013;288(25):18013-18021.
55. Ibrahim MA, Griko NB, Bulla LA. Cytotoxicity of the *Bacillus thuringiensis* Cry4B toxin is mediated by the cadherin receptor BT-R<sub>3</sub> of *Anopheles gambiae*. *Exp Biol Med (Maywood)*. 2013;238(7):755-764.
56. Gómez I, Miranda-Ríos J, Rudiño-Piñera E, Oltean DI, Gill SS, Bravo A, *et al*. Hydrophobic complementarity determines interaction of epitope <sup>869</sup>HITDTNNK<sup>876</sup> in *Manduca sexta* Bt-R<sub>1</sub> receptor with loop 2 of domain II of *Bacillus thuringiensis* Cry1A toxins. *J Biol Chem*. 2002;277(33):30137-30143.
57. Gómez I, Arenas I, Benitez I, Miranda-Ríos J, Becerril B, Grande R, *et al*. Specific epitopes of domains II and III of *Bacillus thuringiensis* Cry1Ab toxin involved in the sequential interaction with cadherin and aminopeptidase-N receptors in *Manduca sexta*. *J Biol Chem*. 2006;281(45):34032-34039.
58. Liu XS, Dean DH. Redesigning *Bacillus thuringiensis* Cry1Aa toxin into a mosquito toxin. *Protein Eng Des Sel*. 2006;19(3):107-111.
59. Abdullah MA, Alzate O, Mohammad M, McNall RJ, Adang MJ, Dean DH. Introduction of *Culex* toxicity into *Bacillus thuringiensis* Cry4Ba by protein engineering. *Appl Environ Microbiol*. 2003;69(9):5343-5353.
60. Burton SL, Ellar DJ, Li J, Derbyshire DJ. N-acetylgalactosamine on the putative insect receptor aminopeptidase N is recognised by a site on the domain III lectin-like fold of a *Bacillus thuringiensis* insecticidal toxin. *J Mol Biol*. 1999;287(5):1011-1022.
61. Mathur A, Sethi A, Jogini V, Bhargava Y, Tembe BL, Lala AK. Energetics of insertion of soluble proteins into membrane. *Curr Sci*. 2004;87(2):181-189.

62. Tomimoto K, Hayakawa T, Hori H. Determination of a region of Cry1Aa inserted into *Bombyx mori* BBMV. In: Côté JC, Otvos IS, Schwartz JL, Vincent C, editors. Proceedings of the 6th Pacific Rim Conference on the Biotechnology of *Bacillus thuringiensis* and its Environmental Impact, 2005. Ottawa: National Sciences and Engineering Research Council of Canada (NSERC); 2007. p. 17-18.
63. Aronson AI, Geng C, Wu L. Aggregation of *Bacillus thuringiensis* Cry1A toxins upon binding to target insect larval midgut vesicles. *Appl Environ Microbiol.* 1999;65(6):2503-2507.
64. Puntheeranurak T, Stroh C, Zhu R, Angsuthanasombat C, Hinterdorfer P. Structure and distribution of the *Bacillus thuringiensis* Cry4Ba toxin in lipid membranes. *Ultramicroscopy.* 2005;105(1-4):115-124.
65. Ounjai P, Unger VM, Sigworth FJ, Angsuthanasombat C. Two conformational states of the membrane-associated *Bacillus thuringiensis* Cry4Ba  $\delta$ -endotoxin complex revealed by electron crystallography: implications for toxin-pore formation. *Biochem Biophys Res Commun.* 2007;361(4):890-895.
66. Taveecharoenkool T, Angsuthanasombat C, Kanchanawarin C. Combined molecular dynamics and continuum solvent studies of the pre-pore Cry4Aa trimer suggest its stability in solution and how it may form pore. *PMC Biophys.* 2010;3(1):10.
67. Kato T, Higuchi M, Endo R, Maruyama T, Haginoya K, Shitomi Y, *et al.* *Bacillus thuringiensis* Cry1Ab, but not Cry1Aa or Cry1Ac, disrupts liposomes. *Pestic Biochem Physiol.* 2006;84(1):1-9.
68. Leetachewa S, Katzenmeier G, Angsuthanasombat C. Novel preparation and characterization of the  $\alpha$ 4-loop- $\alpha$ 5 membrane-perturbing peptide from the *Bacillus thuringiensis* Cry4Ba  $\delta$ -endotoxin. *J Biochem Mol Biol.* 2006;39(3):270-277.
69. Carroll J, Ellar DJ. An analysis of *Bacillus thuringiensis*  $\delta$ -endotoxin action on insect-midgut-membrane permeability using a light-scattering assay. *Eur J Biochem.* 1993;214(3):771-778.

70. Tran LB, Vachon V, Schwartz JL, Laprade R. Differential effects of pH on the pore-forming properties of *Bacillus thuringiensis* insecticidal crystal toxins. *Appl Environ Microbiol.* 2001;67(10):4488-4494.
71. Schwartz J-L, Lu YJ, Söhnlein P, Brousseau R, Laprade R, Masson L, *et al.* Ion channels formed in planar lipid bilayers by *Bacillus thuringiensis* toxins in the presence of *Manduca sexta* midgut receptors. *FEBS Lett.* 1997;412(2):270-276.
72. Peyronnet O, Nieman B, Généreux F, Vachon V, Laprade R, Schwartz JL. Estimation of the radius of the pores formed by the *Bacillus thuringiensis* Cry1C  $\delta$ -endotoxin in planar lipid bilayers. *Biochim Biophys Acta.* 2002;1567(1-2):113-122.
73. Puntheeranurak T, Uawithya P, Potvin L, Angsuthanasombat C, Schwartz JL. Ion channels formed in planar lipid bilayers by the dipteran-specific Cry4B *Bacillus thuringiensis* toxin and its  $\alpha 1$ - $\alpha 5$  fragment. *Mol Membr Biol.* 2004;21(1):67-74.
74. Buttcher V, Ruhlmann A, Cramer F. Improved single-stranded DNA producing expression vectors for protein manipulation in *Escherichia coli*. *Nucleic Acids Res.* 1990;18(4):1075.
75. Sambrook J, Maniatis T, Fritsch EF. *Molecular cloning: a laboratory manual.* New York, USA: Cold spring harbor laboratory press; 2001.
76. Del Sal G, Manfioletti G, Schneider C. A one-tube plasmid DNA mini-preparation suitable for sequencing. *Nucleic Acids Res.* 1988;16(20):9878.
77. Bradford MM. A rapid and sensitive method for the quantitation of microgram quantities of protein utilizing the principle of protein-dye binding. *Anal Biochem.* 1976;72:248-254.
78. Allen TM, Cleland LG. Serum-induced leakage of liposome contents. *Biochim Biophys Acta.* 1980;597(2):418-426.
79. Pouny Y, Rapaport D, Mor A, Nicolas P, Shai Y. Interaction of antimicrobial dermaseptin and its fluorescently labeled analogues with phospholipid membranes. *Biochemistry.* 1992;31(49):12416-12423.

80. Mrsny RJ, Volwerk JJ, Griffith OH. A simplified procedure for lipid phosphorus analysis shows that digestion rates vary with phospholipid structure. *Chem Phys Lipids*. 1986;39(1-2):185-191.
81. Phillips JC, Braun R, Wang W, Gumbart J, Tajkhorshid E, Villa E, *et al.* Scalable molecular dynamics with NAMD. *J Comput Chem*. 2005;26(16):1781-1802.
82. MacKerell AD, Bashford D, Bellott M, Dunbrack RL, Evanseck JD, Field MJ, *et al.* All-atom empirical potential for molecular modeling and dynamics studies of proteins. *J Phys Chem B*. 1998;102(18):3586-3616.
83. Darden T, York D, Pedersen L. Particle mesh Ewald: an  $N \cdot \log(N)$  method for Ewald sums in large systems. *J Chem Phys*. 1993;98(12):10089-10092.
84. Essmann U, Perera L, Berkowitz ML, Darden T, Lee H, Pedersen LG. A smooth particle mesh Ewald method. *J Chem Phys*. 1995;103(19):8577-8593.
85. Kay BK, Williamson MP, Sudol M. The importance of being proline: the interaction of proline-rich motifs in signaling proteins with their cognate domains. *FASEB J*. 2000;14(2):231-241.
86. Hou T, Chen K, McLaughlin WA, Lu B, Wang W. Computational analysis and prediction of the binding motif and protein interacting partners of the Abl SH3 domain. *PLoS Comput Biol*. 2006;2(1):e1.
87. Williamson MP. The structure and function of proline-rich regions in proteins. *Biochem J*. 1994;297(Pt 2):249-260.
88. Macias MJ, Hyvonen M, Baraldi E, Schultz J, Sudol M, Saraste M, *et al.* Structure of the WW domain of a kinase-associated protein complexed with a proline-rich peptide. *Nature*. 1996;382(6592):646-649.
89. Zhan H, Elliott JL, Shen WH, Huynh PD, Finkelstein A, Collier RJ. Effects of mutations in proline 345 on insertion of diphtheria toxin into model membranes. *J Membr Biol*. 1999;167(2):173-181.
90. Dmitriev OY, Fillingame RH. The rigid connecting loop stabilizes hairpin folding of the two helices of the ATP synthase subunit *c*. *Protein Sci*. 2007;16(10):2118-2122.

91. Roberts KE, O’Keeffe AK, Lloyd CJ, Clarke DJ. Selective dequenching by photobleaching increases fluorescence probe visibility. *J Fluoresc.* 2003;13(6):513-517.
92. Andersson A, Danielsson J, Gräslund A, Mäler L. Kinetic models for peptide-induced leakage from vesicles and cells. *Eur Biophys J.* 2007;36(6):621-635.

## BIOGRAPHY

<b>NAME</b>	Miss Chompounoot Imtong
<b>DATE OF BIRTH</b>	31 January 1983
<b>PLACE OF BIRTH</b>	Tak, Thailand
<b>INSTITUTIONS ATTENDED</b>	Chiang Mai University, 2002-2005 Bachelor of Science (Biology) Mahidol University, 2006-2013 Doctor of Philosophy (Molecular Genetics and Genetic Engineering)
<b>SCHOLARSHIP</b>	B.Sc. Scholarship from the Development and Promotion of Science and Technology Talents Project M.Sc.-Ph.D. Scholarship from the Development and Promotion of Science and Technology Talents Project
<b>ADDRESS</b>	79 Moo 2, Wangchan, Sam-Ngao, Tak 63130 E-mail: chompou_ron@hotmail.com

## PUBLICATION AND PRESENTATION

1. **Imtong, C., et al.** (2014) *Bacillus thuringiensis* Cry4Aa insecticidal protein: functional importance of intrinsic stability of the unique  $\alpha$ 4- $\alpha$ 5 loop comprising the Pro-rich sequence. **Biochim Biophys Acta**. doi: 10.1016/j.bbapap.2014.03.003.
2. **Imtong, C., et al.** (2011) Structure of the proline-rich region within  $\alpha$ 4- $\alpha$ 5 loop of pore-forming domain is required for larvicidal activity of *Bacillus thuringiensis* Cry4Aa toxin. In Abstract of **the 37<sup>th</sup> Congress on Science and Technology**, October 10-12, 2011, Thailand.